

UNIVERSITA' DEGLI STUDI DI PAVIA

FACOLTA' DI INGEGNERIA
DIPARTIMENTO DI INGEGNERIA INDUSTRIALE E DELL'INFORMAZIONE

DOTTORATO DI RICERCA IN TECNOLOGIE PER LA SALUTE, BIOINGEGNERIA E BIOINFORMATICA
XXXIII CICLO - 2020

CAROTID ARTERY AND STENTING: FROM GEOMETRICAL ANALYSIS TO COMPUTATIONAL HEMODYNAMICS

PhD Thesis by
GIOVANNI MARIA FORMATO

Advisor:
Prof. Michele Conti

PhD Program Chair:
Prof. Silvana Quaglini



“You have to trust in something. Your god, destiny, life, karma, whatever. Because believing that the dots will connect down the road will give you the confidence to follow your heart even when it’ll lead you off the well know path, and that will make all the difference.”

By Steve Jobs

Abstract (English)

Vascular geometry and hemodynamics are key biomechanical factors involved in the onset, progression, and post-treatment follow-up of carotid artery disease. In this dissertation, carotid geometry and hemodynamics were analyzed from two different clinical perspectives, i.e., hypertension and stenting, developing innovative computational frameworks for each condition.

In the first part, the relation between arterial flow, carotid and vertebral morphometry, and blood pressure was assessed. A semi-automatic framework for the objective anatomic subdivision and morphometric analysis of these vessels into different vascular tracts was implemented, basing on the curvature analysis of centerlines reconstructed by spatially adaptive free-knot regression splines. Results from the application of the implemented tool on a cohort of patients showed that hypertensives had a significant reduction of blood flow in all the investigated vessels, and a possible relation between blood pressure, arterial flow and vertebral artery geometry was suggested.

In the second part, we aimed to assess the impact of carotid stenting as well as stent design on the resulting carotid blood flow. A framework to simplify the set-up of the computational fluid dynamic simulation in the stented carotid artery was developed, exploiting the immersed method for the inclusion of the stent inside the blood domain. Alongside, a meshing tool for the semi-automatic local mesh refine-

ment in proximity of the endovascular device was implemented. The potentialities of the proposed tool were then assessed in a proof-of-concept study comparing the carotid hemodynamics after the implant of four different commercial stents. Results showed that stenting did not significantly alter carotid bulk flow dynamics, but increased the external carotid artery resistance (particularly closed-cell stent designs). Also, it was observed the formation of low time-averaged wall shear stresses areas at the carotid sinus and near the stent struts, although with no clear association with stent design.

In both cases, the developed frameworks significantly reduced the workload associated to the specific task. This thesis promotes the idea that computational tools can support the clinical research by shading new light on biomechanics of vascular diseases.

Abstract (Italian)

La geometria vascolare e l'emodinamica sono due fattori biomeccanici che giocano un ruolo fondamentale per quanto concerne l'inizio, la progressione ed il decorso post-trattamento delle patologie della carotide. In questa tesi, la geometria e l'emodinamica carotidea sono state analizzate da due prospettive cliniche, l'ipertensione e lo stenting, sviluppando degli strumenti computazionali innovativi per ciascuna condizione.

In particolare, la prima parte della tesi si propone di analizzare la dipendenza che intercorre tra il flusso arterioso, la morfometria delle carotidi e delle arterie vertebrali, e la pressione arteriosa sistemica. A tale scopo si è implementata una piattaforma in grado di operare, in maniera semi-automatica, l'analisi morfometrica di tratti anatomici di interesse identificati sfruttando l'analisi della curvatura delle centerlines ricostruite mediante spatially adaptive free-knot regression splines. I risultati derivanti dall'applicazione di tale strumento su una coorte di pazienti hanno mostrato che negli ipertesi esiste una significativa riduzione di flusso in tutti i vasi analizzati e, unicamente per le arterie vertebrali, una possibile relazione tra pressione arteriosa, flusso sanguigno e geometria vascolari. La seconda parte della tesi si propone invece di analizzare l'impatto dell'impianto dello stent e del suo design sul flusso carotideo. A tale scopo si è sviluppata una procedura per semplificare e velocizzare l'impostazione della simu-

lazione fluidodinamica computazionale della carotide post-stenting, adottando un approccio “immersed” per l’inclusione dello stent nel dominio computazionale. Inoltre, è stato implementato un algoritmo per la generazione di una mesh rifinita localmente nell’intorno del dispositivo endovascolare. Per valutare le potenzialità dello strumento proposto, è stato eseguito uno studio preliminare comparando l’emodinamica carotidea risultante dall’impianto di quattro diversi stent commerciali. I risultati non hanno mostrato un’alterazione significativa del pattern di flusso all’interno della carotide post-stenting, ma piuttosto un incremento della resistenza vascolare della carotide esterna (in particolare per quanto concerne gli stent con design a celle chiuse). Inoltre, si è osservata la formazione di aree a bassi time-averaged wall shear stresses presso il seno carotideo e tra le maglie dello stent, sebbene senza una chiara correlazione con il suo design. In entrambi i casi, i metodi sviluppati hanno consentito di ridurre significativamente la complessità dell’indagine per cui sono stati implementati. In conclusione, questa tesi promuove l’utilità e l’efficacia degli strumenti computazionali bioingegneristici a supporto della ricerca clinica e dell’indagine di nuovi aspetti biomeccanici delle patologie vascolari.

List of Abbreviations

BA	basilar artery
BC	boundary condition
BP	blood pressure
CAD	computer-aided designed
CAS	carotid artery stenting
CCA	common carotid artery
CEA	carotid endarterectomy
CFD	computational fluid dynamic
CFL	Courant-Friedrichs-Lewy
CT	computed tomography
EC	endothelial cell
ECA	external carotid artery
ECM	extra-cellular matrix
FE	finite element

ICA internal carotid artery
ISR in-stent restenosis
ITK Insight Toolkit
LCA left internal carotid artery
LVA left vertebral artery
MR magnetic resonance
NSE Navier-Stokes equations
PC phase contrast
PDE partial differential equation
RCA right internal carotid artery
RVA right vertebral artery
SARS spatially adaptive free-knot regression splines
SMC smooth muscle cell
TAWSS time-averaged wall shear stress
VA vertebral artery
VMTK Vascular Modelling Toolkit
VTK Visualization Toolkit
WSS wall shear stress

Contents

English abstract	iii
Italian abstract	v
List of Abbreviations	ix
List of Figures	xv
List of Tables	xix
1 Rationale	1
1.1 Thesis outline	3
1.1.1 Chapter 2	4
1.1.2 Chapter 3	4
1.1.3 Chapter 4	4
1.1.4 Chapter 5	5
1.1.5 Chapter 6	5
2 Atherosclerosis in the major intracranial arteries: patho- physiology and treatment	7
2.1 Anatomy of interest: carotid and vertebral arteries	7

2.2	Structure, function and response to injury of the arterial wall	10
2.3	Pathophysiology of atherosclerosis	12
2.4	Surgical treatment: the minimally invasive approach	14
3	Implementation of a platform for the semi-automatic morphometric analysis of carotid and vertebral arteries	17
3.1	Introduction	17
3.2	Computational techniques for geometric analysis of blood vessels	20
3.2.1	Segmentation and 3-D model reconstruction	20
3.2.2	Centerline computation	21
3.2.3	Geometric quantities of interest	22
3.3	Efficient estimation of 3-D vascular centerlines by spatially adaptive free-knot regression splines	23
3.3.1	Data and model	23
3.3.2	Issues with curvature estimation by central differences in VMTK	26
3.3.3	Free-knot regression splines	28
3.3.4	Search of optimal knots: general algorithm and implementation details	33
3.3.5	Curvature computation	34
3.3.6	Comparison with VMTK smoothing algorithm and standard regression splines	38
3.4	Implementation of the semi-automatic platform	40
3.4.1	Introduction	40
3.4.2	General structure	42
3.4.3	Internal carotid subdivision	43
3.4.4	Vertebral artery subdivision	43
3.5	Final comments and future developments	44
4	Can arterial morphometry affect cerebral perfusion and raise systemic wall pressure? Experience at the	

Bristol Heart Institute	47
4.1 Introduction	47
4.2 Patient dataset	48
4.3 MR image acquisition, segmentation and centerline extraction	48
4.4 Blood flow measurements	50
4.5 Morphometric analysis	51
4.6 Statistical analysis	51
4.7 Efficacy of the measurement platform	52
4.8 Comparison of vascular morphometry and flow between normotensives and hypertensives	52
4.9 Associations between vascular morphometry and blood flow	54
4.10 Analysis of the results	57
4.11 Final comments and future developments	60
5 From systemic to local risk factor: implementation of a simulation framework to assess carotid hemodynamics after carotid stenting	63
5.1 Introduction	63
5.2 Computational techniques for hemodynamic analysis of blood vessels	64
5.2.1 Equations and material properties	64
5.2.2 Computational domain	67
5.2.3 Meshing	67
5.2.4 Solution of the Navier-Stokes equations	69
5.2.5 Hemodynamic quantities of interest	70
5.3 Methods for the hemodynamic simulation of the stented carotid and related issues	71
5.4 Goal of the study	78
5.5 The “immersed solid method”	78
5.6 Semi-automatic local mesh refinement: the proposed approach	80
5.6.1 Basics of GMSH	83

5.6.2	Mesh generation	85
5.6.3	Boundary identification	88
5.6.4	Crop and remesh	88
5.7	Mesh sensitivity analysis in an idealized model of im- mersed stent strut	89
5.7.1	Motivations	89
5.7.2	The computational model	90
5.7.3	Mesh sensitivity analysis	92
5.7.4	Discussion	96
5.8	Time-step sensitivity analysis	100
5.8.1	Motivations	100
5.8.2	Computational model	102
5.8.3	Time-step sensitivity analysis	104
5.8.4	Discussion	109
5.9	Final comments and future developments	112
6	Evaluation of post-stenting carotid hemodynamics with different stent designs: proof-of-concept study	117
6.1	Introduction	117
6.2	Carotid geometry	120
6.3	Stent geometries	120
6.4	Mesh generation with local refinement	121
6.5	CFD simulation set-up	123
6.6	Post-processing of the simulation results	124
6.7	Impact of stenting on the blood flow field	125
6.8	Impact of stenting on arterial resistance	126
6.9	Impact of stenting on TAWSS distribution	127
6.10	Analysis of the results	129
6.11	Final comments and future developments	133
7	Conclusions	137
	Bibliography	143
	Acknowledgements	163

List of Figures

2.1	Internal carotid artery and its subdivision into different vascular segments.	9
2.2	Vertebral artery and its subdivision into different vascular segments.	11
2.3	Histological section of the arterial wall.	13
2.4	Examples of different stent cell design.	16
3.1	Tortuosity index does not adequately describe the vascular shape.	24
3.2	Space components of the centerlines extracted by VMTK.	28
3.3	Curvatures of the investigated centerlines estimated by central differences.	29
3.4	Block diagram of the algorithm for the search of optimal knots in spatially adaptive free-knot regression splines.	35
3.5	Comparison between the x-, y- and z- components of the centerline c2 reconstructed by VMTK and by SARS.	39
3.6	Comparison between the curvature of centerline c6 computed by VMTK and by spatially adaptive free-knot regression splines.	40

3.7	Comparison between the x-component of the center-line c2 reconstructed by VMTK, SARS, and regression spline with uniform knot vector.	41
3.8	Subdivision of the carotid and vertebral arteries into different vascular tracts.	45
4.1	Comparison of carotid and vertebral blood flows between normotensive and hypertensive subjects.	55
4.2	Comparison of vertebral morphometry between normotensive and hypertensive subjects.	56
4.3	Linear regression models between vertebral morphometry and flow.	57
5.1	Boundary conditions employed for the CFD simulation in the stented carotid model.	66
5.2	Cylindrical flow extensions at the inlet/outlet sections of a carotid model.	68
5.3	Literature review of the methods for the inclusion of the endovascular device in the blood domain in CFD analyses of post-CAS hemodynamics.	72
5.4	Workflow to perform the geometric and hemodynamic analysis of post-stenting carotid artery from post-operative imaging data.	74
5.5	Workflow to perform the geometric, structural, and hemodynamic analysis of pre- and post-stenting carotid artery from pre-operative imaging data.	75
5.6	Comparison between “body-fitted” and “immersed” grids.	77
5.7	Schematic representation of immersed solid boundary in Ansys CFX.	81
5.8	Schematic diagram of the proposed tool for the local mesh refinement around the endovascular device.	84
5.9	Schematic representation of the local mesh refinement and relative parameters.	87
5.10	Computational model used for the mesh sensitivity analysis.	91

LIST OF FIGURES

5.11	Comparison of the velocity magnitude along the longitudinal and transversal directions in the models with body-fitted and immersed uniform meshes at different element sizes.	93
5.12	Comparison of the velocity magnitude along the longitudinal and transversal directions in the models with body-fitted and immersed meshes at different element sizes in the refined region.	95
5.13	Comparison of the wall shear stress magnitude at the stent strut-blood interface in the models with body-fitted and immersed meshes at different element sizes in the refined region.	97
5.14	Patient-specific model used for the time-step sensitivity analysis.	105
5.15	Local mesh refinement and blood flow pattern around the stent struts protruding inside the carotid bifurcation.	107
5.16	Flowrate at the ECA and velocity magnitude at the probed point A recorded at the last cycle of the simulations with different time steps	108
5.17	Vectorial components and magnitude of the WSS vectors at the probed point B recorded at the last cycle of the simulations with different time steps.	108
5.18	Velocity magnitudes at the probed point A over the four simulated cardiac cycles with different time steps.	110
5.19	Verification of applied flow division and mass conservation.	111
6.1	Generation of non-conforming grid when the endovascular device is not perfectly positioned inside the vessel lumen.	119
6.2	Stents deployed in the carotid artery.	121
6.3	Impact of stenting on the blood flow field at the carotid bifurcation.	126
6.4	Impact of stenting on ICA and ECA flow resistances.	127

LIST OF FIGURES

6.5	Impact of stenting on TAWSS distribution.	129
6.6	Impact of stenting on TAWSS areas.	130

List of Tables

3.1	Characteristics of the investigated centerlines extracted by VMTK.	27
4.1	Characteristics of participants.	49
4.2	Groups and relative grouping criteria.	50
5.1	Element edge lengths and number of degrees of freedom (#DOF) of the body-fitted and immersed models with uniform mesh.	92
5.2	Element edge lengths inside the refined region and number of degrees of freedom (#DOF) of the body-fitted and immersed models with local refinement. . .	92
5.3	Minimum values of the velocity magnitude inside the stent strut of the immersed models expressed as percentage of maximum velocity magnitude along each direction.	96
5.4	Maximum relative errors of the velocity magnitude around the stent strut of the immersed models with respect to the body-fitted solution.	96
5.5	Courant numbers and solver iterations at the systolic peak in the models with different time step sizes. . .	106

6.1 Mesh characteristics of the computational models used
for the CFD analysis. 123

Chapter 1

Rationale

Hypertension and atherosclerosis are considered the major risk factors for cardiovascular morbidity and mortality [1]. Although they are independent (who has hypertension does not necessarily have atherosclerosis, and vice versa) increasing evidence suggests that the two conditions have certain common mechanisms, as both often operate simultaneously to affect the cardiovascular system adversely. The effect of the blood flow on the endothelium via mechanotransduction is likely central focus of both diseases [2]. Systemic high blood pressure (BP) and local disturbed hemodynamics alter the mechanical forces to which the vascular wall is normally subjected. The anomalous mechanical stretch and shear stresses on the arterial wall induce oxidative stress on the endothelium [2] with consequent dysfunction [1], a key player in the initiation and maintenance of the vascular inflammation common to both diseases [3, 4]. From a clinical viewpoint, the most harmful effect of such a chronic inflammation is the formation of the atherosclerotic plaque, an abnormal intramural accumulation of material including lipids, proteins and fibrous tissue [5]. In large and medium arteries, the clinical outcomes of the atherosclerosis mostly depend on the time evolution of such a plaque. Its rupture or erosion is the main cause of intraluminal thrombosis

further associated to myocardial infarction [6] or stroke [7]. The latter is the second leading cause of death and the third of disability in the world [8].

Systemic high BP and local hemodynamics are risk factors to atherosclerosis [9], but arterial geometry likely plays a behind-the-scenes role, contributing to arterial resistance [10, 11, 12, 13] and shaping the blood flow [14]. This is suggested by the observation that many cardiovascular disorders occur in the presence of “disturbed” flow by different geometrical configurations. The carotid and coronary bifurcations, the inner aortic arch and the insertion points of aortic branches are preferred sites for endothelial lining lesions [14], while the anomalous endothelial shear stresses exerted by the blood flowing through the stent struts¹ can promote neointima formation and in-stent restenosis [15]. In essence, a complex geometry leading to changes in flow can also lead to biological events. The digital and technological progress of the last decades has been leading to a more accurate, fast and novel investigation of such aspects. On one side, increasingly sophisticated imaging and processing techniques have permitted to investigate the link between the geometric features of the vessels to the brain and the risk associated to the onset of atherosclerosis [16, 17, 18]. On the other side, the growing experience in the field of numerical simulations have produced tools and methodologies to accurately compute the flow pattern and the wall shear stresses (WSS) in subject-specific models of cerebral vessels to study the atherosclerotic plaque formation [19, 20, 14] and rupture [21, 22, 23].

However, the interaction of these aspects has not been sufficiently investigated neither as regards the origin of systemic high BP that yet predisposes to and accelerates atherosclerosis, nor as regards the post-treatment risk of re-stenosis in the stented carotid, thereby possibly missing shared mechanisms involved in the same complex condition

¹A stent is a tubular structure that is expanded in the lumen of a stenosed artery to restore its patency and raise blood flow. The reader will find more details in section 2.4.

[1]. On one hand, a few studies have demonstrated that primary hypertension may originate from an insufficient blood supply to the brain [24], suggesting the cause in the morphometric abnormalities of vertebral arteries (VAs) [25, 26] and external carotid arteries (ECAs) [27, 28, 29], but a systematic analysis correlating vascular geometry and cerebral blood flow in hypertensives is missing. On the other hand, only few studies deal with the hemodynamic simulation inside a stented carotid artery, because the inclusion of the endovascular device involves a number of modelling issues that require the implementation of *ad hoc* methodologies [30, 31].

Therefore, the first aim of this dissertation is to elucidate the relationship between local and global morphometry of the major intracranial arteries in hypertensive patients and assess their relationship with arterial flow and BP. Moving from systemic to local level, the second aim is to evaluate the flow dynamics inside the carotid artery with an implanted stent to assess the hemodynamic impact of different stent designs. Following a bioengineering approach, each aim is accomplished by setting up innovative computational tools for the investigations of such aspects in patient-specific problems.

1.1 Thesis outline

The thesis is organized as follow.

Chapter 2 introduces basic notions of the anatomic district and relative disease of interest. Chapters 3 - 4 and 5 - 6 are the core of this work, and are structurally similar. First, the novel methodology is presented, reporting the details of the implementation as well as preliminary proof-of-concept results. Then, the novel tool is applied to a problem of interest to answer the specific clinical question. Finally, Chapter 7 draws the conclusions of the present work.

In the following, a brief summary of each chapter is given.

1.1.1 Chapter 2

This chapter introduces anatomic notions of the vascular districts of interest, i.e., the internal carotid artery (ICA) and VA, as well as relative anatomic subdivision used in the medical field. Then, after a focus on the structure, function and response to injury of the arterial wall, it describes the mechanisms involved in the pathology of atherosclerosis. Finally, it introduces the stenting surgical procedure for the treatment of atherosclerotic carotid arteries, analyzing the main complications associated to the technique which deserve the engineer's eye to be improved.

1.1.2 Chapter 3

This chapter introduces a preliminary overview of the main computational methods for the reconstruction, processing and analysis of vascular geometries from medical images. Then, it presents the implementation of the algorithms for the efficient estimation of 3-D vascular centerlines and their curvature by spatially adaptive free-knot regression splines (SARS). Comparative tests with standard centerline reconstructions methods are presented. Finally, it describes the implementation of a platform for the semi-automatic morphometric analysis of ICA and VA based on the analysis of centerline curvature.

1.1.3 Chapter 4

This chapter presents a retrospective study including 142 patients in which the implemented platform is used to perform a detailed analysis of the local and global morphometry of the major intracranial arteries in order to assess differences between hypertensive and normotensive subjects as well as associations between vascular morphometry, blood flow and systemic BP.

1.1.4 Chapter 5

This chapter introduces the main concepts and steps to analyze the hemodynamics of blood vessels by means of computational fluid dynamic (CFD) simulations. Then, after an overview of the methods for the CFD simulation of post-carotid artery stenting (CAS) hemodynamics, it focuses on the immersed approach evidencing the related modelling issues. It then deals with the creation of a framework for the simulation of post-CAS hemodynamics with the immersed approach in which the fluid mesh is locally refined in proximity of the endovascular device. Finally, grid and time-step sensitivity analyses on simple problems for the tuning of the meshing and simulation parameters are presented.

1.1.5 Chapter 6

This chapter presents a preliminary comparative study in which the developed framework for the post-CAS hemodynamic simulation is used to evaluate the effect on carotid blood flow resulting from the implant of four different commercial stents. Specifically, the impact of stenting is assessed with respect to alterations of blood flow pattern, ICA and ECA resistances, and time-averaged wall shear stress (TAWSS) distribution.

Chapter **2**

Atherosclerosis in the major intracranial arteries: pathophysiology and treatment

2.1 Anatomy of interest: carotid and vertebral arteries

The brain receives oxygenated blood from two sources: the right internal carotid artery (RCA) and left internal carotid artery (LCA) supply blood to the anterior brain, while the right vertebral artery (RVA) and left vertebral artery (LVA) irrigate the posterior brain. The common carotid arteries (CCAs) supply blood to the neck and head and have an asymmetric origin: the left CCA arises directly from the aortic arch, while the right CCA branches off the brachiocephalic trunk. After a thoracic course, each CCA travels vertically in the neck until bifurcates into the internal carotid artery (ICA) and external carotid artery (ECA) at the level of the fourth cervical ver-

tebra. Both branches travel upward, but while the ECAs travel more superficially to supply the neck and face, the ICAs take a deeper path and go to the skull to supply the brain. The ICAs have a rather peculiar course and this dissertation presents a detailed description of its morphometry basing on an automatic subdivision into different tracts from its centreline. The most widely used system describing the ICA segments was proposed by Bouthillier and colleagues [32] as follows (figure 2.1):

- Cervical segment, from the carotid bifurcation to the entrance of the carotid canal in the skull (segment C1);
- Petrous segment, inside the petrous part of the temporal bone until the foramen lacerum (segment C2);
- Lacerum segment, from the foramen lacerum to the petrolingual ligament (segment C3);
- Cavernous segment, from the petrolingual ligament to the proximal dural ring, surrounded by the cavernous sinus. In this tract, the ICA curves to form the so-called carotid siphon (segment C4);
- Clinoid segment, after the exit of the ICA from the cavernous sinus to the distal dural ring (segment C5);
- Ophthalmic segment, from the distal dural ring to the origin of the posterior communicating artery (segment C6);
- Communicating segment, or cerebral segment, from the origin of the posterior communicating artery to the bifurcation of the ICA (segment C7).

On the other hand, the vertebral arteries (VAs) supply blood to the upper spinal cord, brainstem, cerebellum, and posterior part of the brain. VAs can be subdivided into four segments starting from their

point of origin at the subclavian arteries on each side of the body (figure 2.2):

- preforaminal tract, from their origin to the transverse process of the sixth cervical vertebra (segment V1);
- foraminal tract, in the transverse foramina from the sixth to the second vertebra (segment V2);
- atlantic tract, as VAs issue from the C2 foramen transversarium. This is further subdivided into the vertical segment V3v passing vertically upwards, crossing the C2 root and entering the foramen transversarium of C1, and the horizontal segment V3h, curving medially and posteriorly behind the superior articular process of the atlas;
- intracranial tract.

ICA and VA circulations are not separated. The basilar artery (BA) connects to the ICAs of both sides through an anastomotic arterial ring called the circle of Willis. If one of the major arteries becomes occluded, this structure potentially allows for blood flow compensation from the others, ensuring that any part of the brain continues to receive the oxygenated blood.

2.2 Structure, function and response to injury of the arterial wall

To better understand how pathological changes of the arterial wall can lead to vascular diseases, we will first examine the main structural and functional characteristics of blood vessels. A histological section of a healthy artery shows three separated concentric layers having different composition to explicate specific functions (figure 2.3). The tunica adventitia is the outermost layer. It is composed

2.2. Structure, function and response to injury of the arterial wall

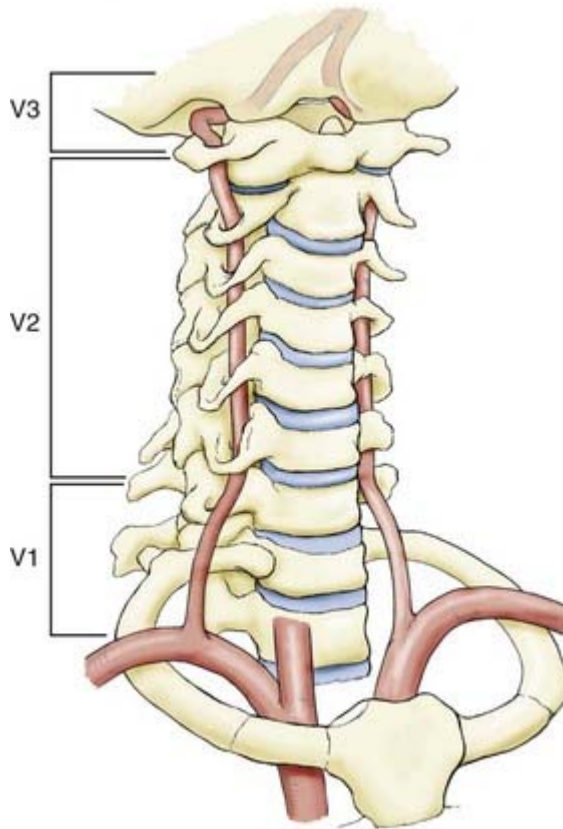


Figure 2.2: Vertebral artery and its subdivision into different vascular segments. Reproduced from <https://neupsykey.com/extracranial-vertebral-artery-diseases/>

by loose connective tissue, often merged with the surrounding structures. The tunica media is composed of smooth muscle cells (SMCs) and extra-cellular matrix (ECM) components. It is responsible for the mechanical properties of the blood vessels and intervenes during the vascular repair, when SMCs migrate from the tunica media to the innermost layer, the tunica intima, to proliferate and form neointimal tissue. This mechanism becomes dangerous in the atherosclerosis, where recurring injuries lead to an excessive neointima formation with consequent stenosis of the small and medium arteries. Finally, the tunica intima is a single-layer of endothelial cells (ECs); this layer, called the endothelium, not only is responsible for the maintenance of a non-thrombogenic interface between blood and tissues, but is essential for the regulation of vascular homeostasis. Through a mechanism called “endothelial activation”, the endothelium can carry out new functions (e.g., activation of coagulation, modulation of vascular resistance, regulation of inflammation, SMC growth control ...) in response to external pathophysiological stimuli [34]. In cardiovascular diseases, another state of the endothelium called “endothelial dysfunction”, occurs when the altered phenotype is systematically associated to compromised vasoreactivity, inflammatory and thrombogenic state. Endothelial dysfunction plays a key role in triggering the thrombosis, atherosclerosis and vascular lesions typical of hypertension or other pathologies [35].

2.3 Pathophysiology of atherosclerosis

Atherosclerosis is a condition where intimal lesions lead to the formation of atheromatous plaques protruding into the vascular lumen. The reader may find a comprehensive description of atherosclerosis in the excellent book by George and Johnson [36]; in this section, we only give an overview of its pathophysiology. The current model of atherosclerosis relies on a “response to injury” hypothesis [37], i.e., atherosclerosis has to be seen as a chronic inflammatory response of the arterial wall to an endothelial damage, involving a complex

2.3. Pathophysiology of atherosclerosis

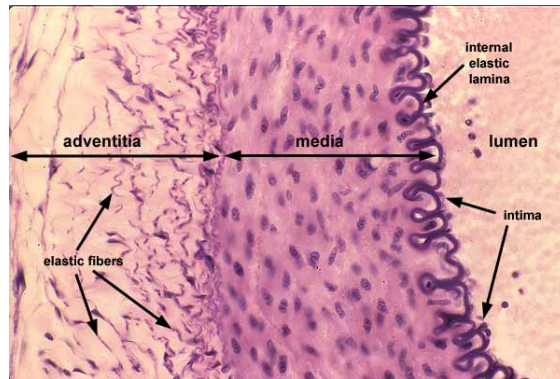


Figure 2.3: Histological section of the arterial wall. It is possible to distinguish the three layers composing the vascular wall (tunica intima, tunica media and tunica adventitia). Reproduced from (<http://www.pathologyoutlines.com/topic/softtissuevascnormal.html>)

interaction between lipoproteins, white blood cells and normal constituents of blood vessels. The atherosclerosis is the result of the following pathogenic events:

1. Endothelial damage and dysfunction (initiation of the atherosclerotic lesion);
2. Adhesion of lipoproteins (start of the inflammatory response);
3. Adhesion of monocytes to the endothelium, migration into the intima and formation of foam cells (formation of fatty streak);
4. Platelet adhesion;
5. Platelet-induced SMC migration to the intima;
6. SMC proliferation and neointima formation;
7. Lipid accumulation (plaque formation).

The outcomes of atherosclerosis depend on the size of the involved vessels, the plaque stability and the severity of the damage of the underlying arterial wall. Briefly:

- the intraluminal growth of the atherosclerotic plaques can lead to the occlusion of small arteries, compromising the perfusion of distal tissues and leading to ischemic events;
- the atherosclerotic plaque can evolve and lead to the sudden formation of a thrombus and acute stroke. Eventually, the plaque can rupture and the fragments can occlude a vessel downstream;
- the structural degeneration of the underlying vascular wall can lead to aneurysm formation with secondary rupture and/or thrombosis.

2.4 Surgical treatment: the minimally invasive approach

High risk carotid stenosis is usually treated surgically. Two options are available: carotid endarterectomy (CEA) and carotid artery stenting (CAS). While CEA is an invasive procedure in which the surgeon physically removes the atherosclerotic plaque through an incision in the neck at the location of the stenosis, CAS is the minimally invasive approach in which the surgeon restores the patency of the stenosed carotid by implanting a tubular prosthesis, i.e., a stent. These endovascular devices are currently available in balloon expandable and self-expanding types. Typically, self-expanding stents are the standard for CAS because they better accommodate to the chronic compressive forces, mobility and calibre drop of the carotid bifurcation [38]. Whether CAS is a safe (and safer) alternative to CEA is still a matter of debate, as different carotid stenting clinical trials have pointed out [39, 40, 41, 42, 43]. However, while the intra- and post-procedural outcomes of CEA are completely determined by the ability of the surgeon and the limits of the technique itself, there is still a room for improvement for CAS. A stent is designed to accomplish two goals: 1) opens the stenosed lumen and preserves its patency over time; 2) contains the atherosclerotic plaque

2.4. Surgical treatment: the minimally invasive approach

by pushing it against the arterial wall. However, a stent must also be designed in order to ensure safety: during the implant, i.e., it has to be flexible to easily accommodate to the vessel tortuosity to reduce embolic potential; during the follow-up, i.e., it has to limit the intimal injury that predisposes to in-stent restenosis (ISR), which is the formation of neointimal tissue producing a new stenosis in the stented vessel. The geometric design of the stent plays central role in both phases [44, 45]. Closed-cell stents (top pane of figure 2.4) are generally characterized by small free-cell area (i.e., the area enclosed by connected struts). This kind of stent provides greater plaque coverage but the high strut density is associated to an increase of the stiffness of the device [46], difficult implantation, and elevated blood flow velocities [47]. Conversely, open-cell stents (bottom pane of figure 2.4) are generally characterized by larger free-cell area, providing more malleability during the implant but also more exposure of the atherosclerotic plaque, possibly increasing the embolic risk [48]. Because of different adopted criteria and follow-up duration, the reported incidences of ISR are controversial, ranging from 1% to 70% [49]. ISR may originate from stent-induced endothelial damage due to a) mechanical stresses exerted by the stent structure pushing against the arterial wall [50], and b) hemodynamic stresses exerted by the altered blood flow [15]. Concerning the last point, the implantation of a stent to treat a stenosed carotid bifurcation leads to a significant hemodynamic change potentially impacting the whole district. Immediately after CAS, as the stenosis is removed and the lumen patency restored, the blood can immediately flow through the treated vessel to re-perfuse the distal tissues adequately. But the implanted stent leaves its trace on the blood flow, and the restored hemodynamics is not one hundred percent physiological. First, the rigid structure of the stent induces a straightening and enlargement of the stented segment [51, 52], thus changing the hemodynamic pattern (vascular geometry “shapes” the blood flow) [51] but also altering the vascular resistance [53, 54]. Second, the stent struts immersed in the blood flow field (near the arterial wall of the stented segment and

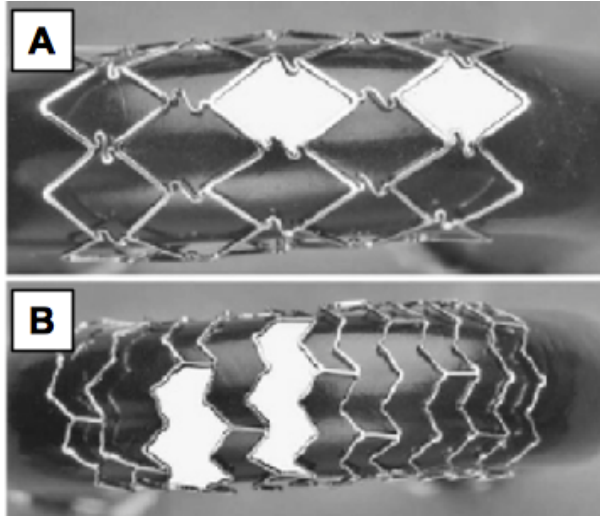


Figure 2.4: Examples of different stent cell design. A) A closed-cell stent; B) an open-cell stent. Adapted from [55].

across the bifurcation at the ICA/ECA ostium) generate anomalous flow structures such as recirculation zones, stagnation zones and small vortices because of the impact with the blood. Different clinical studies have sought the association between stent cell geometry and ISR rate [45], but little attention has been given to the physical mechanisms involved in the stent-vessel interaction, particularly as regards the effect of the geometry of the stent cells on local hemodynamics in the post-CAS carotid artery. In chapter 6, a comparative study among different stent designs with respect to the resulting carotid hemodynamics will be presented.

Chapter 3

Implementation of a platform for the semi-automatic morphometric analysis of carotid and vertebral arteries

3.1 Introduction

Besides behavioural [75] and genetic [76] risk factors, cerebral hypoperfusion has been proposed as a potential cause for hypertension [24]. Insufficient blood flow to the brainstem would elevate sympathetic nerve activity in order to trigger an increase in blood pressure (BP) and restore cerebral blood flow [77, 25]. This has been termed the Cushing’s mechanism [24], or the “selfish brain hypothesis”, and has been supported by post-mortem [26], animal [78, 79], and human studies [25]. If inadequate cerebral perfusion is responsi-

ble for the origin and/or evolution of hypertension, it is important to elucidate the mechanisms behind reduced perfusion in hypertensives, and one parameter of interest is the morphometry of cerebral arteries. Vessel geometry can be related to the onset of specific cerebrovascular wall diseases [80], but whether it plays a role also in the onset of hypertension is still a matter of debate. On one hand, it has been shown that vessel tortuosity increases in age-related remodelling of healthy subjects [102, 17] and that the morphological and functional changes of vascular walls are accelerated in hypertension [103]. On the other hand, early work in cadaveric hypertensive patients suggested a positive correlation between vascular resistance and BP [26], stronger for the vertebral arteries (VAs) than the carotid arteries, and hypothesized that smaller size and a more tortuous course of the artery reduce posterior cerebral flow contributing to hypertension [26], although systematic analysis of the vessels' geometry was lacking and no evidence to support causality was available. More recently, however, it was demonstrated that hypertensive subjects had a greater prevalence of congenital (thus, regardless age) cerebrovascular variants of the posterior circulation such as VA hypoplasia, incomplete posterior circle of Willis or both, and that these variants were functionally associated with lower cerebral perfusion [25]. The possible association between intracranial internal carotid artery (ICA) morphometry and essential hypertension is not known. While previous work focused on morphological abnormalities of the extracranial ICA [27, 28, 29], Romanko-Hrushchak et al. explored the prevalence of anatomic variants in the cerebral vessels, including the ICAs, and observed that hypertensives had narrower VAs, more tortuous cervical tract of the ICAs, and narrower anterior cerebral arteries [81]. However, the study did not analyse the prevalence of vascular morphological variants with respect to changes in cerebral blood flow. Despite some evidences suggesting a relationship between the cerebrovascular morphometry and the development of hypertension, it is not known whether and to what extent the morphometry of the major cerebral arteries is involved in the reduction of cerebral flow.

3.1. Introduction

To date the identification of anatomic variants of the carotid and vertebral arteries in hypertensives has been mostly based on visual inspection of medical imaging data affected by intra- and inter-observer variability, using a binary classification criterion for vessel hypoplasia [82], and disregarding other morphometric features that might also affect arterial hemodynamics such as vessel tortuosity [10, 11] and curvature [12, 13]. On the other hand, robust and objective medical imaging processing methods for the definition and measurement of geometric quantities in arteries have been assessed. Among the others, the Vascular Modelling Toolkit (VMTK) is a large open-source project aiming to share computational tools for the geometric and hemodynamic analysis of blood vessels [59]. Although extensively used by researchers in the field, some of the available algorithms suffer of numerical noise and generate unreliable data, jeopardising their applicability. One of the goal of the present study is to perform an objective subdivision of both the ICA and VA based on the analysis of their curvature, adapting a published method proposed by Piccinelli and co-workers for the geometric characterisation of the ICA in relation to cerebral aneurysm formation [83]. Unfortunately, as will be shown in section 3.3.2, the curvature of a centerline directly computed by VMTK is associated to unacceptable numerical errors despite the availability of post-processing algorithms. In 2009 Sangalli and colleagues proposed a more efficient and accurate way for estimating the vascular centerlines and their curvature function based on spatially adaptive free-knot regression splines (SARS) [84], demonstrating its superiority over a classical regression method, the local polynomial smoothing [85], in terms of efficiency, accuracy and computational cost [86].

With such premises, the first aim of this study is to implement the method adopted by Sangalli and co-workers for a correct and efficient estimation of 3-D vascular centerlines and their curvature. The second aim is to integrate such algorithms in a semi-automatic platform for systematic vascular subdivision and morphometric assessment of the intracranial right internal carotid artery (RCA), left in-

ternal carotid artery (LCA), right vertebral artery (RVA), and left vertebral artery (LVA). We discuss the accomplishment of such aims in this chapter. We present in chapter 4 the third aim of the study, i.e., making use of the implemented platform, we want to analyze the local and global morphometry of the major intracranial arteries in normotensive and hypertensive subjects and assess their relationship with arterial flow and blood pressure. We hypothesise that decreasing vascular mean cross-sectional area, increasing tortuosity and increasing vessel length are associated with decreased arterial flow, or in other words that hypertensive subjects exhibit narrower, more tortuous and longer vessels compared to normotensives.

3.2 Computational techniques for geometric analysis of blood vessels

In the present section, we provide a preliminary overview of the main computational methods for the reconstruction, processing and analysis of vascular geometries from medical images. These background notions will permit to show some of the limits of the traditional approaches, which will be faced in the second part of the chapter.

3.2.1 Segmentation and 3-D model reconstruction

Patient-specific geometries are reconstructed from medical images in two steps: image segmentation and surface reconstruction. The process of segmentation partitions each image in the dataset into multiple segments (i.e., sets of pixels) sharing a common characteristic (e.g. the gray intensity), modifying the representation of each image to easily detect the 2-D contours of the vessel lumen. The simplest and most popular segmentation method relies on the use of thresholds to turn a gray-scale image into a binary representation to

detect the vascular boundaries. This approach is, for example, integrated in the commercial software Mimics (version 19; Materialise, Leuven, Belgium) and will be adopted for the segmentation of the ICAs and VAs in chapter 4. To overcome the high time consumption and low reproducibility of the method due to the manual set of the threshold values, a myriad of more sophisticated and automatic segmentation algorithms have been proposed in recent years, see for example [57] for a systematic review on the subject. Among these, the level set segmentation has been implemented in the most popular softwares for medical imaging processing such as InSight Toolkit (ITK) [58] and VMTK [59], and has been used for example in chapter 6 to segment the unstented carotid artery. In this method, the image contour is the zero level set of a higher dimensional function, i.e., a partial differential equation (PDE), which is iteratively deformed by image-based features such as mean intensity, gradient and edges until it fits the shape of the anatomic structure. For a comprehensive review of segmentation methods, the reader is reminded to the paper by Sethian et al [60].

Once the segmentation is done, the second step consists of the generation of a 3-D representation of the blood vessel through dedicated algorithms, the most common is the marching cubes interpolation algorithm [56]. The output of this process is a surface model - e.g., in the STL format - representing the inner wall of the blood vessel.

3.2.2 Centerline computation

With the 3-D reconstruction at hand, it is possible to compute the vascular centerline. The geometric analysis of the blood vessels is, in fact, based on centerlines, because they are powerful descriptors of the vascular shape and 3-D orientation. Although the concept of centerline is more or less intuitive - a curved line running through the centre of the vessel -, its mathematical definition is less trivial and numerous methods have been proposed [61]. For this task, we adopt the open-source software VMTK, that extracts the centerlines

from the Voronoi diagram [62]. The theoretical and implementation details of how the centerline is defined in VMTK may be found in [63]. From a practical viewpoint, the only manual task for the centerline computation consists of selecting the source and target points in correspondence of the inlet/outlet sections of the model. Such points constitute the endpoints of the centerline, which in the end will be output as a set of 3-D points in a sheet-like form.

3.2.3 Geometric quantities of interest

The extracted centerline and the 3-D model of the vessel can be integrated to build geometric descriptors of the vascular anatomy. In chapter 4, we will perform a detailed analysis of the geometry of the intracranial ICA and VA. The considered tracts do not contain important vascular branches or bifurcations, therefore in this section we introduce only the geometric descriptors for this kind of -simple-vessels. An overview of the geometric characterization of bifurcations may be found for example in Thomas et al. [17]. We basically adopt three simple but rather effective descriptors:

1. curvature, defined as the reciprocal of the radius of the osculating circle at a point along the centerline;
2. tortuosity, defined as the ratio between the length of the centerline of a vascular segment and the distance between its first and last point;
3. the cross-sectional area, defined by the intersection between a plane perpendicular to the centerline at a certain point and the surface of the vascular 3-D model.

Importantly, both curvature and tortuosity relate to the concept of “sinuosity” of a blood vessel, but at two different levels. The first is a local metrics describing the shape of the centerline at a specific point, while the second is a distance metrics describing the global

3.3. Efficient estimation of 3-D vascular centerlines by spatially adaptive free-knot regression splines

path of a centerline. The tortuosity index may therefore be misleading. As an example, in figure 3.1 we computed the tortuosity of two different ICAs; it is possible to see that although the two vessels have completely different shape, the tortuosity indexes are very similar. A better description of the vascular morphometry may be accomplished by integrating also a tortuosity index for “local” vascular tracts as defined later on in this chapter. Moreover, if the vascular tracts are identified by looking at the curvature of the vessel, each computed tortuosity index refers only to one bending of the vessel. Such concepts will be detailed in section 3.4. However, it is first necessary to face the problem of correctly estimating the curvature of a centerline in an efficient manner by implementing *ad hoc* centerline reconstruction methods. This aspect will be addressed in the next section.

3.3 Efficient estimation of 3-D vascular centerlines by spatially adaptive free-knot regression splines

3.3.1 Data and model

The starting point of this section is the luminal surface of a vessel reconstructed through the segmentation of any kind of angiographic images. To keep things simple, let us consider a non-bifurcating vessel, i.e., the reconstructed surface has one inlet and one outlet. As shown in section 3.2.2, it can be defined a 3-D curve c running through the centre of the vessel, called a centerline. Importantly, here by c we mean the *true* centerline, i.e., the analytical curve that we want to extract to ultimately estimate its curvature. The natural parametrization of the 3-D curve c through the definition of the curvilinear abscissa s allows to write c in terms of three space coordinates:

$$c(s) = (x(s), y(s), z(s)) \quad (3.1)$$

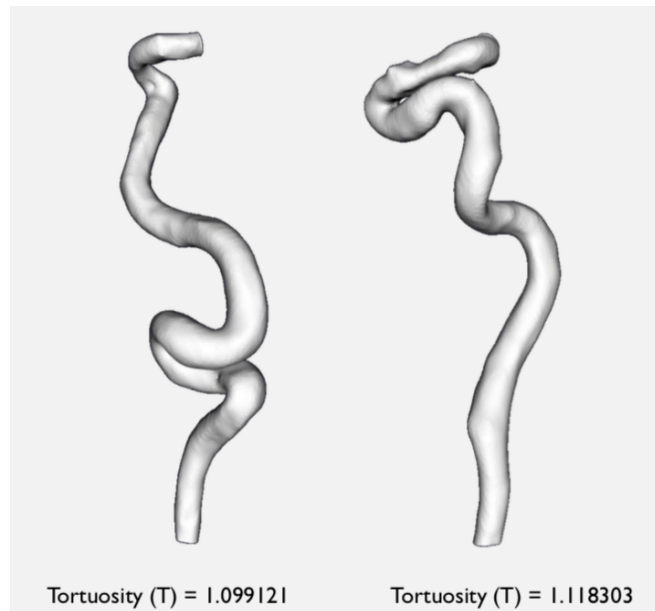


Figure 3.1: Tortuosity index does not adequately describe the vascular shape. Two different ICAs have been analyzed with respect to the global tortuosity index. Results show similar tortuosity indexes, although the vessels have different shapes.

3.3. Efficient estimation of 3-D vascular centerlines by spatially adaptive free-knot regression splines

and, accordingly, compute the curvature as:

$$\text{curv}_c(s) = \frac{\|c'(s) \times c''(s)\|}{\|c'(s)\|^3} \quad (3.2)$$

In practice, however, we deal with *reconstructed* centerlines, which come as a discrete set of n points in R^3 , $\{(x_i, y_i, z_i) : i = 1, 2, \dots, n\}$, where x , y and z denote the three space coordinates of the i_{th} point. Such points are ordered in a list going from the source to the target point as selected during the centerline extraction. When the study involves multiple patients, it is convenient to choose as starting point of each centerline a specific anatomic structure present in the images of each patient, in order to have all the centerlines consistently oriented. With the discrete representation of c , we can still define a discrete curvilinear abscissa $\{s_i : i = 1, 2, \dots, n\}$, which measures an approximate distance along the centerline. For instance, if (x_0, y_0, z_0) is the first point of the centerline, then:

$$\begin{cases} s_1 = \sqrt{(x_1 - x_0)^2 + (y_1 - y_0)^2 + (z_1 - z_0)^2} \\ s_2 = s_1 + \sqrt{(x_2 - x_1)^2 + (y_2 - y_1)^2 + (z_2 - z_1)^2} \\ \dots \\ s_n = s_{n-1} + \sqrt{(x_n - x_{n-1})^2 + (y_n - y_{n-1})^2 + (z_n - z_{n-1})^2} \end{cases} \quad (3.3)$$

and so on for all the points in the centerline. According to the formula 3.2, the computation of the curvature of a reconstructed centerline described as a discrete set of points requires to pointwise estimate the first and second derivatives by central differences schemes. As we will see in the next section, such a choice leads to extremely noisy results, motivating the need to first reconvert the reconstructed centerline to an approximating analytical function, and then perform the exact derivatives on that.

3.3.2 Issues with curvature estimation by central differences in VMTK

As a case study, we consider a reconstructed RCA from the database of the University of Bristol and extract a total of seven centerlines (c0, c1, c2, c3, c4, c5, and c6) with different combinations of resampling length and smoothing algorithm. Specifically, centerline c0 is not resampled, while centerlines c1 and c2 are resampled every 0.08 mm as suggested by Sangalli [86], but with different resampling algorithms. Centerlines c3, c4 and c5 are equivalent to centerlines c0, c1 and c2, respectively, but are smoothed by different smoothing algorithms. Finally, centerline c6 is resampled every 1 mm and smoothed. Table 3.1 summarises the characteristics of each investigated centerline as well as the script in VMTK used to extract it. We compare the x-, y- and z- components of the reconstructed centerlines as well as the computed curvature functions in order to assess which of the investigated algorithms bring the less noisy results. Each centerline starts below the insertion of the anterior cerebral artery and runs downstream to the cervical tract.

Figure 3.2 shows that there are not substantial differences between the space components of the investigated centerlines. That is to say: if the outcome of interest can be extracted directly from the reconstructed centerline without any further operation (such as derivation), each of the investigated algorithms would be accurate enough. However, table 3.1 shows that the resampling provided by the `-resampling` function directly called inside the `vmtkcenterlines` algorithm is worse than that provided by the `-vmtkcenterlineresampling` script both in terms of average resampling length (0.066 mm versus 0.08 mm, set length: 0.08 mm) and standard deviation (0.022 mm against 0.00055 mm). Such a thing will have to be taken into account when implementing the SARS method, as it requires uniformly distributed points on the centerline to work efficiently. Figure 3.3 displays the curvature computed from each investigated centerline. We observe that the central difference method for estimating the first and

3.3. Efficient estimation of 3-D vascular centerlines by spatially adaptive free-knot regression splines

Table 3.1: Characteristics of the investigated centerlines extracted by VMTK. From left to right: label of the centerline, VMTK script used to extract the centerline, number of sampling points, mean (standard deviation) of the sampling length.

Centerline	VMTK script	N. of points	L (σ) [mm]
c0	vmtkcenterlines -pipe vmtkcenterlinegeometry	771	0.13 (0.10)
c1	vmtkcenterlines -resampling 1 -resamplingstep 0.08 -pipe vmtkcenterlinegeometry	1482	0.066 (0.022)
c2	vmtkcenterlineresampling -length 0.08 -pipe vmtkcenterlinegeometry	1222	0.08 (5.52e-04)
c3	vmtkcenterlines -pipe vmtkcenterlinegeometry -smoothing 1	771	0.13 (0.10)
c4	vmtkcenterlines -resampling 1 -resamplingstep 0.08 -pipe vmtkcenterlinegeometry -smoothing 1	1482	0.066 (0.022)
c5	vmtkcenterlineresampling -length 0.08 -pipe vmtkcenterlinegeometry -smoothing 1	1222	0.08 (5.52e-04)
c6	vmtkcenterlines -pipe vmtkcenterlineresampling -length 1.0 -pipe vmtkcenterlinegeometry -smoothing 1	98	1.004 (0.004)

second derivatives produces extremely noisy results (centerlines c0, c1, and c2). The smoothing algorithm provided by VMTK (which is a moving average filter acting on the computed curvature) attenuates the noise originating from the operation of numeric derivation but the resulting curvature is still too noisy to be used. In particular, let us compare the curvatures of c0 with c3, c1 with c4 and c2 with c5. Although much cleaner, it is practically impossible to identify any specific peak of the curvature associated to the bending of the vessel. The solution typically adopted is to increase the length of resampling. The bottommost plot in figure 3.3 displays the curvature of c6, i.e., obtained after a resampling of 1 mm and then smoothed by a moving average filter. The smoothing and resampling algorithms reduce the noise but, as we will see later on in this section, also degrade the accuracy of the computed curvature, motivating the adoption of a more advanced reconstruction method.

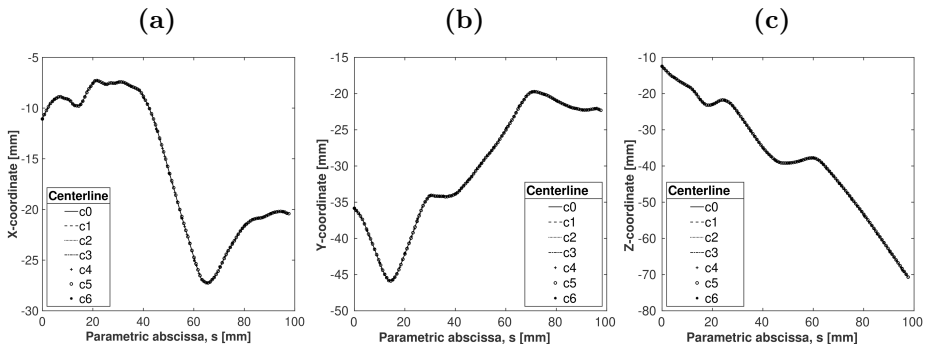


Figure 3.2: Space components of the centerlines extracted by VMTK. In this case, the centerlines are line segments reconstructed from the sampling points; if these are sufficiently numerous, the space components agree among the investigated cases. (a) x-component; (b) y-component; (c) z-component.

3.3.3 Free-knot regression splines

As shown in the previous section, the numeric derivation of the reconstructed centerlines leads to extremely noisy curvatures unless a very low-resolution resampling in conjunction with a moving average filter are used. However, the so computed curvature does not accurately describe the real curvature of the vessel. We anticipated in section 3.3.1 that a good strategy consists of first reconverting the sampled centerline into an approximating analytical function and then computing the derivatives analytically. As approximating functions, we use the free knot regression splines, i.e., regression splines where the number and position of knots are not fixed in advance, but chosen in a way to minimize a penalized sum of squared errors criterion. Some questions may arise in the inexpert reader. What is a spline? How can a spline be used to fit a 3-D sampled curve? What are free knot 3-D regression splines and how can we implement the algorithm for the search of optimal knots? We will answer these question in the following sections. We will provide only a brief overview of the subject whenever this is extensively described in the literature. Specifically, the spline theory is given in [87], the algorithm for the

3.3. Efficient estimation of 3-D vascular centerlines by spatially adaptive free-knot regression splines

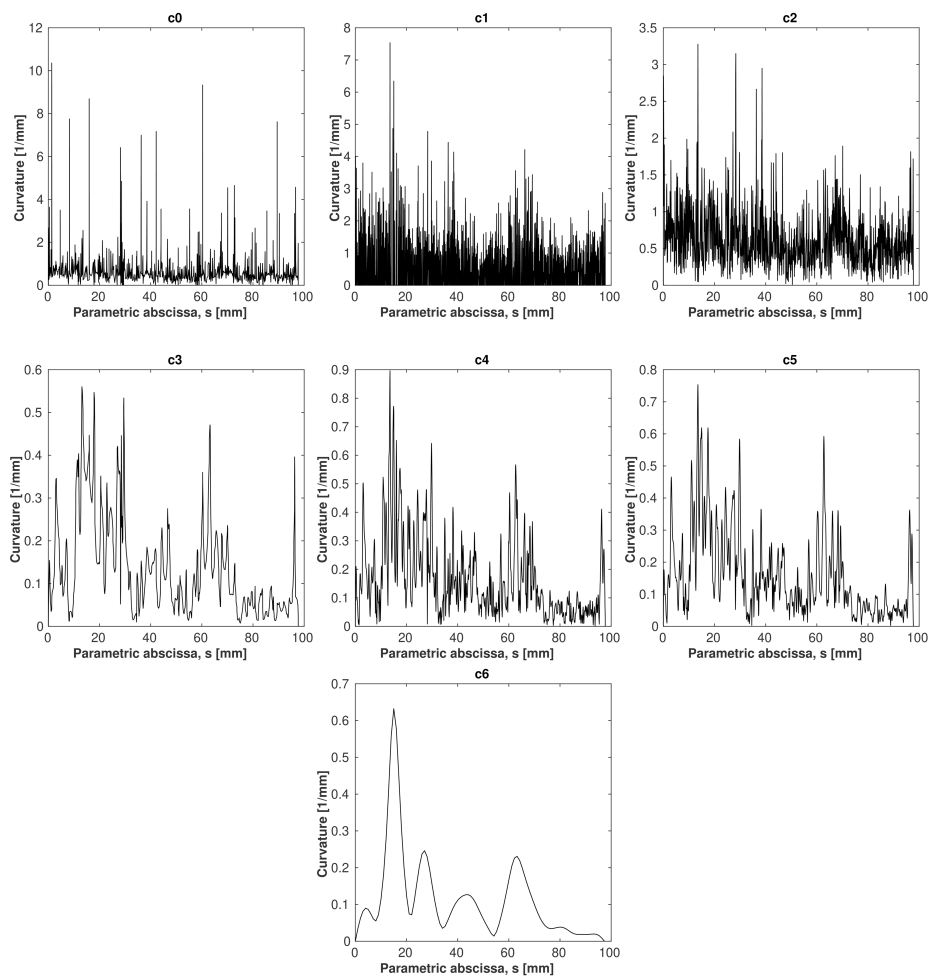


Figure 3.3: Curvatures of the investigated centerlines as extracted by VMTK. The adoption of the central differences technique to compute the curvature leads to extremely noisy results, unless a high resampling length are used.

search of optimal knots is given in [84], the extension to the 3-D case for centerline fitting is given in [86]. Instead, we will focus more on the details of the implementation, which is somehow less intuitive to replicate from the above mentioned papers.

Splines

Let $\Lambda = \{a < t_1 < t_2 < \dots < t_k < b\}$ be a subdivision of the closed interval $[a, b] \subset \mathbb{R}$. A spline $f_p(s)$ of order p with knot vector $K = \{t_1, t_2, \dots, t_k\}$ is a piecewise polynomial function where:

- in each subinterval of $[a, b]$ the function $f_p(s)$ is a polynomial of degree $p-1$;
- the function $f_p(s)$ is of class C^{p-2} in $[a, b]$.

The set of all order- p splines over $[a, b]$, with knot vector K , forms a vector space of dimension $p+k$. The dimension $p+k$ is the number of free parameters, given by the difference between the number of parameters needed to determine $(k+1)$ polynomials of degree $(p-1)$, and the continuity constraints prescribing $p-1$ equations at each of the k knots. Thus: $(k+1)(p) - (p-1)(k) = p+k$. A good basis system for such a vectorial space is represented by the b-splines (i.e., basis splines) $\{b_{r,p}^{[K]}(s) : r = 1, 2, \dots, p+k\}$, such that every spline of order p with knot vector K is expressed as a linear combination of b-splines for some coefficient vector λ , as following:

$$f_p(s) = \sum_{r=1}^{p+k} \lambda_r b_{r,p}^{[K]}(s) \quad (3.4)$$

Importantly, derivatives of splines are still splines with the same knot vector but having a new vector coefficient λ' directly computed from the vector coefficient λ of the original spline.

Regression splines

Let us now introduce the concept of regression splines. For the sake of simplicity, we stay in 1-D. We will deal with 3-D problems further on in this section.

Let $f(s) : [a, b] \subset \mathbb{R} \rightarrow \mathbb{R}$ be a generic curve. This is the *true* curve that we want to estimate, just like $c(s) = (x(s), y(s), z(s))$ of section 3.3.1 was the *true* centerline. Also, as for $c(s)$, we only have a set of n points sampled from $f(s)$, namely $w_j = \{(s_j, f_j), j = 1, 2, \dots, n\}$. In general, $s_j \neq f(s_j)$, i.e.:

$$s_j = f(s_j) + e_j \quad (3.5)$$

Our problem is described as follows: we want to estimate $f(s)$ by means of an order- p regression spline $\hat{f}(s)$ with knot vector K , which fits through the points w_j minimizing the sum of squared errors. That is to say:

$$\hat{f}(s) = \sum_{r=1}^{p+k} \hat{\lambda}_r b_{r,p}^{[K]}(s) \quad (3.6)$$

where $\hat{\lambda} = (\hat{\lambda}_1, \hat{\lambda}_2, \dots, \hat{\lambda}_{p+k})^T$ minimizes the sum of squared errors:

$$SSE(\hat{\lambda}) = \sum_{j=1}^{n_j} (w_j - \sum_{r=1}^{p+k} \hat{\lambda}_r b_{r,p}^{[K]}(s))^2 \quad (3.7)$$

Free knot regression splines

In the equation 3.7, the order p of the regression spline depends on the derivatives that have to be performed on the approximated function $\hat{f}(s)$. It is convenient to use at least $p=d+3$, where d is the highest derivative order that has to be estimated. In our case, we perform second order derivatives, and regression splines of order 6 will be adopted. Concerning the knot vector K , there are two choices: the first is to assign a knot vector *a priori* (for example, where knots are uniformly distributed along the interval $[a, b]$); the second is to

choose the number and position of the knots by minimizing a suitable error functional taking into account the dimension of the model being fitted. The last case describes a *free knot* regression splines, because the knot vector is not assigned *a priori*. A possible model estimator is represented by the Stein's unbiased risk estimate [88], which adds a penalization term $C(p + k)$ to the SSE of equation 3.7.

Extension to the 3-D case

The extension of the 1-D problem discussed so far to the 3-D case was proposed by Sangalli and co-workers in a rather straightforward way [86]. The idea is to estimate the true centerline $c(s)$ by simultaneously fitting its components $x(s)$, $y(s)$, $z(s)$ with three regression splines $\hat{x}(s)$, $\hat{y}(s)$, $\hat{z}(s)$ of order p having the same knot vector K . Obviously, when represented by b-splines, the three regression splines have three different vectors of coefficients $\hat{\lambda}^{[x]}$, $\hat{\lambda}^{[y]}$, $\hat{\lambda}^{[z]}$. Note that each component $x(s)$, $y(s)$, $z(s)$ is a 1-D curve just like the function $f(s)$ of the previous section, associating to a value of the parametric abscissa s the correspondent x -, y - and z - coordinate. It can be demonstrated that the natural extension to the 3-D case of the SSE defined by equation 3.7 is:

$$\begin{aligned}
 3DSSE(\hat{\lambda}) = & \sum_{j=1}^{n_j} (x_j - \sum_{r=1}^{p+k} \hat{\lambda}_r^{[x]} b_{r,p}^{[K]}(s))^2 + \\
 & \sum_{j=1}^{n_j} (y_j - \sum_{r=1}^{p+k} \hat{\lambda}_r^{[y]} b_{r,p}^{[K]}(s))^2 + \\
 & \sum_{j=1}^{n_j} (z_j - \sum_{r=1}^{p+k} \hat{\lambda}_r^{[z]} b_{r,p}^{[K]}(s))^2
 \end{aligned} \tag{3.8}$$

and, for the search of the optimal knots, the model selector is simply obtained by adding the penalization term $C(p + k)$ to the 3DSSE of equation 3.8.

3.3.4 Search of optimal knots: general algorithm and implementation details

We now describe the algorithm for the search of optimal knots proposed by Zhou and colleagues [84]. A block diagram showing the general structure is provided in figure 3.4. The algorithm starts by constructing an initial knot vector K where the knots are uniformly distributed between the extremes of the centerline curvilinear abscissa (s_1 and s_n). The knot vector K has an extended structure, i.e., if the associated regression splines have order p , the first p knots are equal to s_1 , and the last p knots are equal to s_n . Such a structure will be maintained as the algorithm proceeds, ensuring that the reconstructed regression splines interpolate the first and last points of the centerline components. Once K is defined, the algorithm essentially consists of two different steps: knot addition and knot relocation/deletion. Such operations are performed at two levels of refinement, which explains the presence of two functions for the same operation. When the label (ALL) is present (functions ADD KNOT (ALL) and RELOCATE/DELETE KNOT (ALL) [algorithms 2 and 4]), the functions operate on all the knots of K . On the contrary, the operations are performed only on those knots having at least one of the neighbour knots been added in the previous iteration (functions ADD KNOT and RELOCATE/DELETE KNOT [algorithms 1 and 3]). In both cases, however, the operations affect only the internal knots to preserve the extended structure of the vector. Each time the knot vector K is modified, three new regression splines (one for each component of the centerline) are generated and a new penalized least squared error as defined in the formula 3.8 is computed. Zhou and Shen constructed local regression splines by taking a subset of the knot vector to save computational cost assuming that the addition/deletion/relocation of one knot causes only a *local* change of the original regression spline. We construct regression splines approximating the entire components of the centerline, but compute a local error taking a neighbourhood having a radius of twenty grid points

around the modified knot. Our choice does not bring a dramatic slowdown of the code. The new knot vector is kept if the computed error is minor than the one obtained with the previous knot configuration.

Concerning the addition of the knots in the interval under investigation $[t_i, t_{i+1}]$, Sangalli and co-workers looked for the optimal knots among the values of the curvilinear abscissa $t_i < s_j < t_{i+1}$ because the sampling of the centerline ensured a fine enough grid. Differently, by using the Fibonacci algorithm, we iteratively subdivide the knot interval $[t_i, t_{i+1}]$ into subintervals of decreasing size to find the one associated to the smallest error. We stop the algorithm when the subinterval becomes smaller than δ , that is the maximum length found between two consecutive grid points s_i of the original centerline. Then, we place a trial knot in the middle point of the identified subinterval.

The algorithm is coded entirely in Matlab (MATLAB Release 2018b, The MathWorks, Inc., Natick, Massachusetts, United States), exploiting the spline toolbox [89] for the spline generation and evaluation. Specifically, for the generation of the m-order regression spline fitting x-y data from knot vector K , we adopt the following command:

```
spmak(t, slvblk(spcol(K,m,x, 'slvblk', 'noderiv'), y) . ');
```

where `spcol` generates the collocation matrix, `slvblk` means that the collocation matrix is block diagonal, `noderiv` means that the multiplicities are ignored. As for the evaluation of the regression spline, we adopt the built-in function `fnval` provided by the toolbox.

3.3.5 Curvature computation

The computation of the curvature requires the derivation of the generated regression splines. The spline toolbox adopted in this study does not provide any tool to perform such an operation. Therefore, we adopt the Matlab built-in symbolic variables. We first write the generated regression splines in terms of piecewise polynomials as symbolic expressions. Then, we perform the derivatives using the built-in

3.3. Efficient estimation of 3-D vascular centerlines by spatially adaptive free-knot regression splines

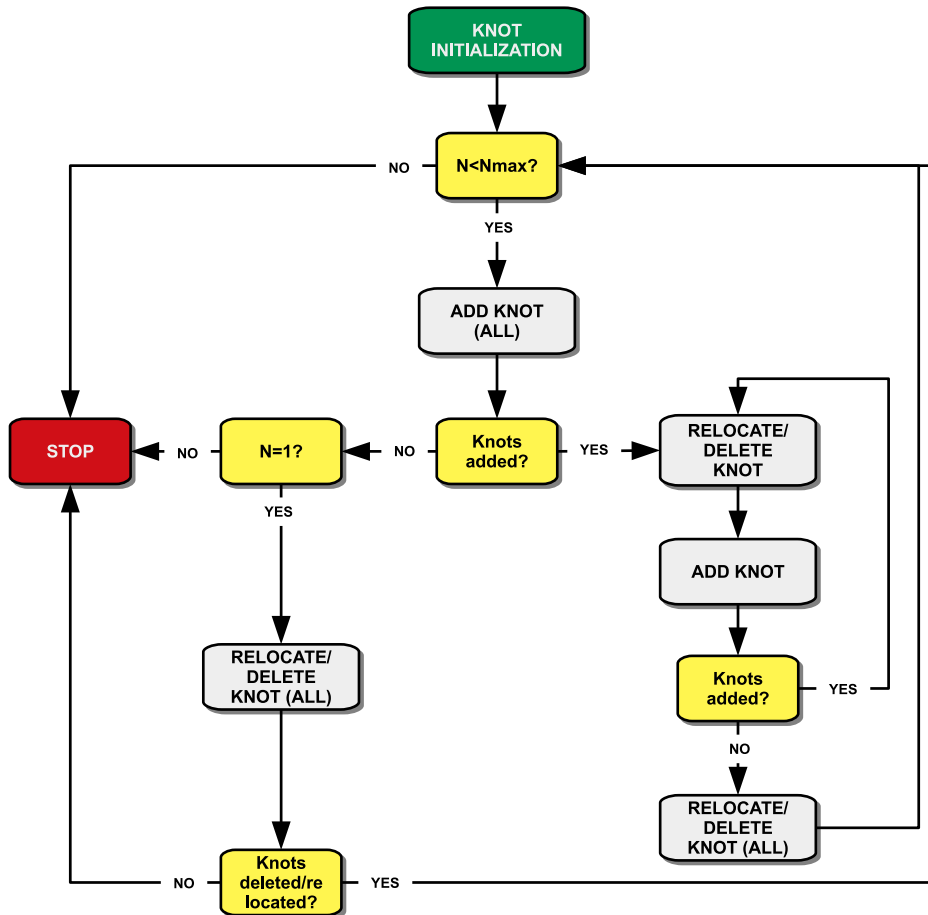


Figure 3.4: Block diagram of the algorithm for the search of optimal knots in spatially adaptive free-knot regression splines. The diagram reproduces the algorithm proposed by Zhou and Shen [84].

Algorithm 1: ADD KNOT

Result: Performs knot addition only in knot intervals surrounding knots added in the previous step
 Φ contains knots added in the previous step;
for t_i *in knot vector* K **do**
 if *at least one* $\{t_{i+j}, j = -2, -1, 0, 1, 2, 3\}$ *is in* Φ **then**
 if *knot interval* $[t_i, t_{i+1}]$ *smaller than* δ **then**
 do nothing;
 else
 $3DSSE \leftarrow$ compute local error with original K ;
 find trial knot t^{trial} in $[t_i, t_{i+1}]$ using Fibonacci algorithm
 $3DSSE^{trial} \leftarrow$ compute local error with trial knot vector K^{trial} ,
 end
 if $3DSSE^{trial} < 3DSSE$ **then**
 update K , i.e., $K \leftarrow K^{trial}$
 end
 end
end

Algorithm 2: ADD KNOT (ALL)

Result: Performs knot addition in all knot intervals
for t_i *in knot vector* K **do**
 if *knot interval* $[t_i, t_{i+1}]$ *smaller than* δ **then**
 do nothing;
 else
 $3DSSE \leftarrow$ compute local error with original K ;
 find trial knot t^{trial} in $[t_i, t_{i+1}]$ using Fibonacci algorithm;
 $3DSSE^{trial} \leftarrow$ compute local error with trial knot vector K^{trial} ,
 end
 if $3DSSE^{trial} < 3DSSE$ **then**
 update K , i.e., $K \leftarrow K^{trial}$
 end
end

3.3. Efficient estimation of 3-D vascular centerlines by spatially adaptive free-knot regression splines

Algorithm 3: RELOCATE/DELETE KNOT

Result: Performs relocation/deletion only of knots near knots added in the previous step

Φ contains knots added in the previous step;

```

for  $t_i$  in knot vector  $K$  do
  if at least one  $\{t_{i+j}, j = -2, -1, 0, 1, 2, 3\}$  is in  $\Phi$  then
    construct new knot vector  $K^{del}$  without knot  $t_i$ ;
     $3DSSE^{del} \leftarrow$  compute local error with knot vector  $K^{del}$ ;
    find trial knot  $t^{trial}$  in  $[t_i, t_{i+1}]$  using Fibonacci algorithm;
    construct new trial knot vector  $K^{trial}$  containing the relocated
      knot  $t^{trial}$ ;
     $3DSSE^{trial} \leftarrow$  compute local error with knot vector  $K^{trial}$ ;
    if  $3DSSE^{trial} < 3DSSE^{del}$  then
      relocate the knot  $t_i$ ;
      update  $K$ , i.e.  $K \leftarrow K^{trial}$  ;
    else
      delete the knot  $t_i$ ;
      update  $\Phi$ ;
      update  $K$ , i.e.,  $K \leftarrow K^{del}$ ;
    end
  end
end
end
/* If at least one knot has been deleted in the previous
loop, two knots in  $\Phi$  can now be adjacent. Thus, perform
the knot relocation/deletion uniquely on  $\Phi$ . */
for  $t_i$  in knot vector  $K$  do
  if  $t_i$  is in  $\Phi$  then
    if at least one  $\{t_{i+j}, j = -1, 1\}$  is in  $\Phi$  then
      /* Repeat the steps seen in the first loop */
    end
  end
end
end

```

Algorithm 4: RELOCATE/DELETE KNOT (ALL)

Result: Performs relocation/deletion of all knots
for t_i *in knot vector* K **do**
 construct new knot vector K^{del} without knot t_i ;
 $3DSSE^{del} \leftarrow$ compute local error with knot vector K^{del} ;
 find trial knot t^{trial} in $[t_i, t_{i+1}]$ using Fibonacci algorithm;
 construct new trial knot vector K^{trial} containing the relocated knot t^{trial} ;
 $3DSSE^{trial} \leftarrow$ compute local error with knot vector K^{trial} ;
 if $3DSSE^{trial} < 3DSSE^{del}$ **then**
 relocate the knot t_i ;
 update K , i.e. $K \leftarrow K^{trial}$;
 else
 delete the knot t_i ;
 update K , i.e., $K \leftarrow K^{del}$;
 end
end

symbolic function `diff` and compute the curvature according to the formula 3.2.

3.3.6 Comparison with VMTK smoothing algorithm and standard regression splines

We now test the efficacy of the SARS method to estimate the x-, y- and z- components of the centerline c_2 . We adopt order 6 splines with a penalty parameter C (equation 3.8) set to 4 [86]. The quality of the approximation is measured by computing the SSE_{1D} for each of the analysed component. Figure 3.5 shows an excellent fitting of the three components by SARS ($SSE_{1D} = 0.0018$ for the x- component, $SSE_{1D} = 0.0022$ for the y- component, $SSE_{1D} = 0.0022$ for the z- component). Recall that one of the advantages of the SARS technique is that the approximating functions are piecewise polynomials, so that the computation of the curvature can be performed by analytical differentiation, eliminating the noise component deriving from

3.3. Efficient estimation of 3-D vascular centerlines by spatially adaptive free-knot regression splines

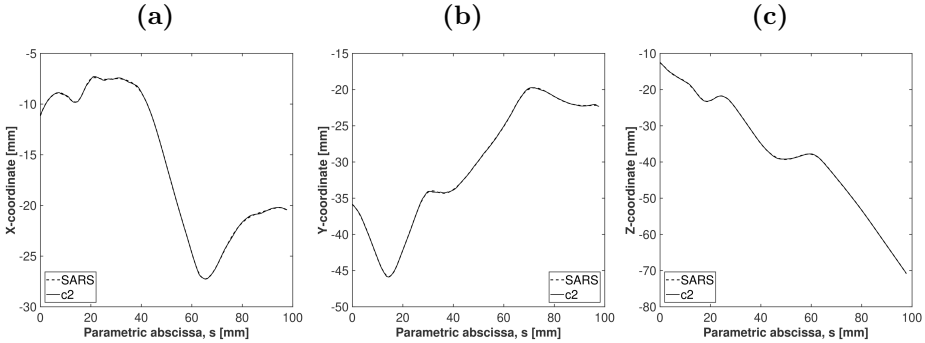


Figure 3.5: Comparison between the x-, y- and z- components of the centerline c_2 reconstructed by VMTK and by SARS. The results show an excellent fitting of the three components using the SARS technique. (a) x-component; (b) y-component; (c) z-component.

the central difference method. Figure 3.6 shows the comparison between the curvature calculated analytically with the SARS method with respect to the curvature of the centerline c_6 reconstructed in VMTK. It is possible to see that the moving average filter adopted by VMTK produces a loss of the curvature peaks and generates an inaccurate curvature preserving only a general trend of the original one. In figure 3.7 we show the comparison between the x- component of the centerlines approximated by SARS and by standard regression splines with respect to the curve reconstructed from VMTK. We also highlight the knots of the two regression splines at the bottom of the figure. The standard regression spline has been built with the built-in function of the spline toolbox using the minimum knot number (i.e., 7). The position of the knots are also set automatically by the function. On the other hand, the SARS algorithm finds a total of 14 knots and sets their position according to the minimisation of the regression error. It is possible to appreciate the effectiveness of the proposed method to better fit the centerline ($SSE_{1D} = 0.3690$ for the noSARS curve, $SSE_{1D} = 0.0018$ for the SARS curve).

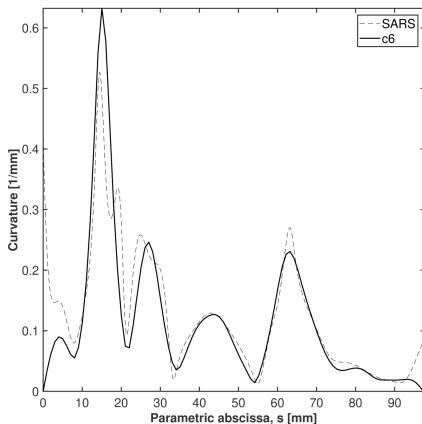


Figure 3.6: Comparison between the curvature of centerline c_6 computed by VMTK and by spatially adaptive free-knot regression splines. Although the trend of the curvatures is similar, the value of the curvature peaks depends on the reconstruction method.

3.4 Implementation of the semi-automatic platform

3.4.1 Introduction

In this section we integrate the methods previously implemented for the fitting of vascular centerlines through SARS into a semi-automatic platform for the morphometric analysis of the ICA and VA. Such a project stemmed from the need of having a computational tool for the objective anatomic subdivision and morphometric measuring of the cerebral vessels in hypertensive patients during the visit at the Bristol Heart Institute (UK), reducing the measuring errors associated to manual measures. We adapt previously proposed methods for the splitting and geometric analysis of the ICA with intracranial aneurysm [83] to work also for the VA. In the next section we will show the general structure of the platform. Then, we will describe more in detail how the splitting of the ICA and VA is

3.4. Implementation of the semi-automatic platform

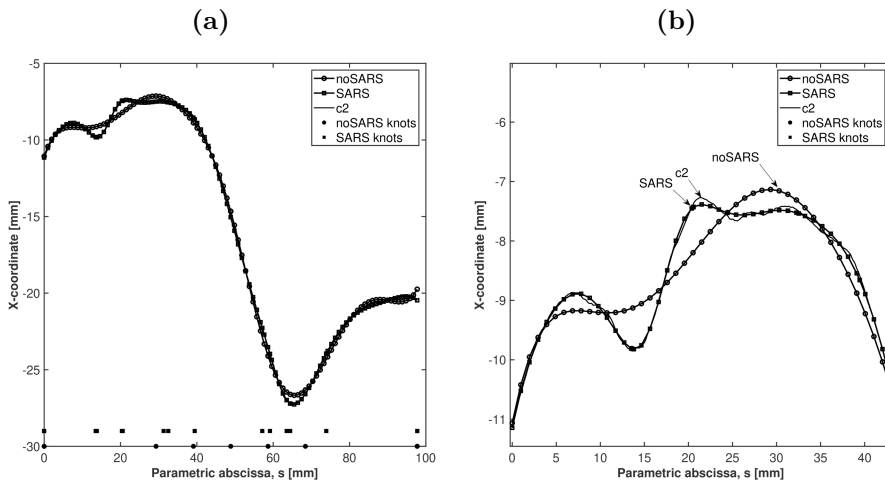


Figure 3.7: Comparison between the x-component of the centerline c_2 reconstructed by VMTK, SARS and regression spline with uniform knot vector. At the bottom axis, the knots of the two regression splines are also highlighted. Spatially-adaptive free knot regression splines are superior to standard regression splines in the estimation of the first component of the centerline. (a) x-component of c_2 reconstructed by VMTK, SARS and uniform knot regression spline; (b) zoom on the x-component first peak where largest errors are found.

achieved.

3.4.2 General structure

The functioning of the platform is rather simple. First, the data files containing the coordinates of each centerline as well as the values of the cross-section areas associated to each point are loaded in Matlab. Such files are generated through the VMTK built-in algorithms `vmtkcenterlines` (for the centerline coordinates) and `vmtkcenterlinegeometry` (for the cross-section areas). Each centerline is reconstructed through SARS and the relative curvature is computed. The platform then enters automatically a loop in which the curvature function is displayed together with the STL model of the vessel. For the VAs, the z-coordinate is also displayed as we will see later on in this chapter. The user can interactively select the peaks of interest that identify different bendings of the vessel, which are automatically stored in separated variables. Eventually, the STL can be rotated in 3-D to check if the selected points correspond to the anatomic bending at which performing the splitting. The user can also decide to cut each vessel at a set length from the last identified bending point. Such a feature allows to obtain vessels that are equally cut across the population of study, particularly important to ensure the uniformity of the relative measures of length and tortuosity. For instance, in a population of carotids in which each centerline starts below the insertion of the anterior cerebral artery and runs downstream to the cervical tract, the platform allows to proximally cut all the centerlines at a defined length after the point that identifies the beginning of the cervical tract. Finally, once the tract of the vessels have been identified by the selected points, the platform reads the loaded files to extract the relative geometric measures. In output, a file containing the measures of curvature, tortuosity and average cross-section areas (as described in section 3.2.3) for each tract is given.

3.4.3 Internal carotid subdivision

The subdivision of the ICAs into five segments relies on the analysis of the curvature of the vessels. For each carotid, the centerline curvature is computed according to Sangalli et al. [86] and five peaks are associated to the relative bendings of the carotid siphon, which in turn are exploited to define an objective subdivision of the vessel into five segments [83]. More specifically, let c_1, c_2, c_3, c_4 and c_5 be the points of maximum curvature, $d_0, d_1, d_2, d_3, d_4, d_5, d_6$ seven additional points placed such that d_0 is the most distal point of the centerline, d_1, d_2, d_3, d_4, d_5 are the middle points between two consecutive points c , and d_6 has an user-defined position referring to the most proximal point of the centerline; each segment is enclosed between two consecutive points d . For each centerline, d_6 can be placed at a certain length downstream the corresponding point c_5 , which identifies the bending of the carotid as it proximally enters the carotid canal. By doing so, all the carotids are reproducibly cut at the cervical level and only the portion of the vessels between d_0 and d_6 is considered for the morphometric analysis. An example is given in figure 3.8.

3.4.4 Vertebral artery subdivision

The subdivision of the VAs into two segments is based on both the curvature and the position of the points of the centerline along the longitudinal axis. In order to obtain an objective subdivision of the VAs, the method adopted for the carotids is slightly modified and the curvature and position of the centerline along the longitudinal axis is exploited instead. A point e_0 is placed at the most distal extremity of the centerline. A second point e_1 is defined corresponding to the peak of the longitudinal coordinate of the centerline, identifying the issuing of the VA from the foramen transversarium of the vertebra C1. Finally, a point e_2 is defined corresponding to the peak of the curvature referring to the lateral sweep of the VA as it emerges from the transverse process of C2 to pass through the transverse foramen

of C1. The last point is used to reproducibly cut all the VAs, leaving the portion from e_0 to e_2 for the morphometric analysis. An example is given in figure 3.8.

3.5 Final comments and future developments

In this chapter, we have built a semi-automatic platform for the systematic subdivision and morphometric analysis of the right and left intracranial ICAs, and right and left intracranial VAs. The subdivision of these vessels into different anatomical tracts was based on the geometric characteristics of the centerline curvature, computed by exact derivatives of the centerline space components reconstructed through SARS as approximating analytical functions. The tool allowed to perform vascular splitting and morphometric analysis of ICAs and VAs in a semi-automated way, significantly reducing the time spent by radiologists to take manual measures, and potentially eliminating the intra- and inter-observer measuring errors.

The tool can be further improved. First, for the subdivision of the VA into two anatomical tracts, we exploited the z-component of the centerline and identified the peak with the issuing of the VA from the foramen transversarium of the vertebra C1. Although such a peak can be found in most patients, it may be absent in some with abnormal anatomic characteristics, compromising the usability of the tool. A more robust criterion for the VA subdivision should be thus implemented. Second, the framework still involves manual operations compromising its full automation. Initially, the segmentation of the medical images and the extraction of the vascular centerlines have to be performed manually to provide the morphometric platform with the necessary input data; then, the subdivision of the vessels into the relevant subdomains relies on the manual identification of the centerline curvature peaks. To achieve such task automatically and improve the level of automation of the analysis, the use of neural

3.5. Final comments and future developments

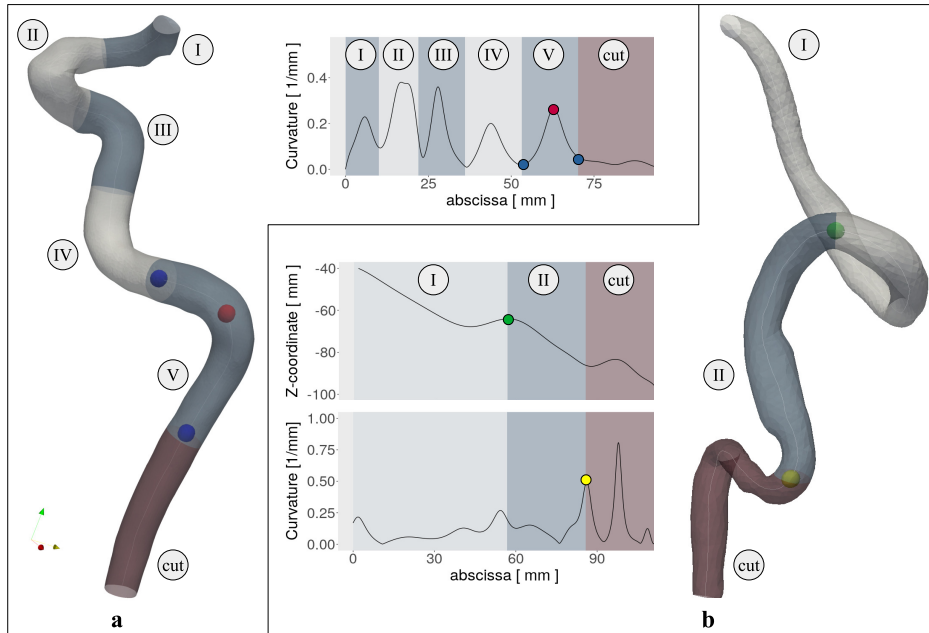


Figure 3.8: Subdivision of the carotid and vertebral arteries into different vascular tracts. a) Example of subdivision of the ICA into five bends. Each bend is identified by a peak of the curvature c and delimited by two points d . For example, the points used to define bend V are the curvature peak c_5 (red circle) and the points d_4 and d_5 (blue circles). These points are highlighted in the graph of the curvature and in the corresponding 3-dimensional model; b) example of subdivision of the VA into two bends. In this case, the point e_1 (green circle) corresponds to the peak of the longitudinal coordinate of the centerline, the point e_2 (yellow circle) corresponds to the peak of the curvature of the centerline. These points are highlighted in the graphs of the longitudinal coordinate and curvature and in the corresponding 3-dimensional model.

3. Arterial morphometry, cerebral perfusion and hypertension

networks could be tested.

Chapter 4

Can arterial morphometry affect cerebral perfusion and raise systemic blood pressure? Experience at the Bristol Heart Institute

4.1 Introduction

The platform implemented in chapter 3 is adopted in a retrospective case-control study involving patients from the Bristol Heart Institute (UK) database to assess the role of the carotid and vertebral morphometry on the reduction of the arterial flow in hypertensive subjects.

4.2 Patient dataset

We use a published dataset including demographic, blood pressure (BP), flow and anatomic data from magnetic resonance (MR) imaging of 142 participants [25]. Of these, 23 participants are excluded due to early termination of MR imaging scan; a further 7 patients are excluded from the analysis of the right internal carotid artery (RCA) and left internal carotid artery (LCA), and 13 patients from the analysis of the right vertebral artery (RVA) and left vertebral artery (LVA) due to motion artefacts in the angiograms or suboptimal image quality. Ultimately, the morphometric analysis is conducted on the carotid arteries of 112 patients and on the vertebral arteries of 106 patients. Based on BP data, patients are classified as normotensives ($< 135/85$ mmHg on daytime average) or hypertensives ($\geq 135/85$ mmHg on daytime average) according to the European guidelines [90]; hypertensives are further divided into four subgroups: untreated, treated resistant, treated uncontrolled and borderline. In total, 71 hypertensive and 41 normotensive individuals are included in the study. The demographic and BP characteristics of the studied patients are reported in table 4.1, while BP criteria are reported in table 4.2.

4.3 MR image acquisition, segmentation and centerline extraction

The anatomy of the major intracranial vessels (RCA, LCA, RVA, LVA) was acquired by 3-D Time of Flight MR angiography using a 3T scanner (GE HDx, Wisconsin, US), which was then used to plan the phase contrast (PC) acquisition for blood flow quantification. Two acquisitions planes were defined: the first acquisition plane was placed 1 cm above the convergence of the vertebral arteries into the basilar artery to derive the blood flow inside the carotid and basilar arteries, the second acquisition plane was placed 1 cm below

4.3. MR image acquisition, segmentation and centerline extraction

Table 4.1: Characteristics of participants. Statistical tests: Chi-squared test for sex comparisons, Welch two-samples t-test otherwise. Data are reported as mean \pm standard deviation and n specifies the sample size. NTN=normotensive, HTN=hypertensive, O-BP=office blood pressure, DA-BP=day-time ambulatory blood pressure, NA-BP=night-time ambulatory blood pressure, SBP=systolic blood pressure, DBP=diastolic blood pressure, MAP=mean arterial pressure, HR= heart rate, BMI=body-mass index.

	NTN (n=41)	HTN (n=71)	p-value
Demographics			
Male sex, n (%)	16 (39%)	42 (59%)	$p = 0.06$
Age, y	44 \pm 15	56 \pm 11	$p < 0.001$
Height, m	1.70 \pm 0.1	1.71 \pm 0.1	$p = 0.7$
BMI, kg/m ²	24.5 \pm 3.3	28.6 \pm 4.2	$p < 0.001$
Family history, n	8 (n=40)	35	$p = 0.004$
O-BP			
SBP, mmHg	123 \pm 8	156 \pm 23	$p < 0.001$
DBP, mmHg	75 \pm 8	91 \pm 13	$p < 0.001$
MAP, mmHg	91 \pm 8	113 \pm 15	$p < 0.001$
HR, bpm	66 \pm 10	66 \pm 11	$p = 0.9$
DA-BP			
SBP, mmHg	120 \pm 9, (n=29)	139 \pm 16, (n=70)	$p < 0.001$
DBP, mmHg	76 \pm 7, (n=29)	86 \pm 11, (n=70)	$p < 0.001$
MAP, mmHg	90 \pm 6, (n=29)	103 \pm 12, (n=69)	$p < 0.001$
HR, bpm	76 \pm 9, (n=29)	74 \pm 10, (n=69)	$p = 0.3$
NA-BP			
SBP, mmHg	107 \pm 10, (n=29)	122 \pm 13, (n=68)	$p < 0.001$
DBP, mmHg	64 \pm 7, (n=29)	72 \pm 9, (n=68)	$p < 0.001$
MAP, mmHg	79 \pm 7, (n=29)	88 \pm 11, (n=67)	$p < 0.001$
HR, bpm	65 \pm 10, (n=29)	64 \pm 10, (n=67)	$p = 0.5$

4. Arterial morphometry, cerebral perfusion and hypertension

Table 4.2: Groups and relative grouping criteria. BP=blood pressure, O-BP=office blood pressure, DA-BP=daytime ambulatory blood pressure, NTN= normotensive, HTN = hypertensive. “Treated” patients were under anti-hypertensive medications.

Group (n)	BP criteria [mmHg]
Normotensive (NTN) (n=41)	O-BP: $\leq 135/85$ DA-BP: $\leq 130/80$
Borderline HTN (n=16)	O-BP: 135 to 140/85 to 90 DA-BP: 130 to 135/80 to 85
Treated-controlled (HTN) (n=17)	O-BP: $\leq 140/90$ DA-BP: $\leq 135/85$
Treated-uncontrolled (HTN) (n=16)	O-BP: $\geq 140/90$ DA-BP: $\geq 135/85$
Untreated (HTN) (n=22)	O-BP: $\geq 140/90$ DA-BP: $\geq 135/85$

the same point to derive the blood flow inside the vertebral arteries. The MR angiograms were imported in Mimics (version 19; Materialise, Leuven, Belgium) and the luminal surfaces of each vessel were reconstructed through a threshold-based segmentation. Each surface was then smoothed by a Laplacian smoothing algorithm (iterations = 100, smoothing factor = 0.1, shrinking compensation). Subsequently, each carotid artery was cropped below the insertion into the circle of Willis, each vertebral artery was cropped below the insertion into the basilar artery. The resulting luminal surfaces were then imported to Vascular Modelling Toolkit (VMTK) [59]. Here, according to section 3.3.1, the centerlines were extracted as a set of discrete 3-D points and then converted into an analytical curve through spatially adaptive free-knot regression splines (SARS) [84, 86].

4.4 Blood flow measurements

Blood flows in the carotid, vertebral and basilar arteries were measured from the PC-MR images using Segment v. 1.9 (Medviso, Sweden). Then, the brain tissue volumes of each patient (cerebrospinal fluid, white and grey matter volumes) were extracted from the 3-D-

4.5. Morphometric analysis

FSPGR images using the Brain Extraction Tool in FSL (FSL, UK) [91] and used to scale the blood flows to express them in mL/min/dL of tissue.

4.5 Morphometric analysis

The objective splitting of each RCA, LCA, RVA and LVA into vascular segments and the analysis of their morphometric features were derived from the geometric analysis of the luminal surfaces and centerlines reconstructed from the 3-D time-of-flight angiograms using the platform implemented in section 3.4.

4.6 Statistical analysis

All statistical tests were carried out in R (R Core Team 2013). Data are presented as mean \pm standard deviation unless otherwise indicated. Normality of the data was assessed by Shapiro-Wilk test. Differences between normally distributed continuous variables were assessed using an unpaired t-test (except for comparisons between right and left vessels within the same patient, in which case a paired t-test was used) and differences between categorical variables with Chi-squared test. For not normally distributed variables, the appropriate non-parametric equivalent tests were used, and multiple comparisons were assessed using the Kruskal-Wallis test with Dunn's test for post hoc adjustment. Associations between variables were assessed by the Pearson's correlation coefficient and linear regression. P-values < 0.05 were regarded to indicate statistical significance, unless Bonferroni-corrected for multiple comparisons (i.e. $p < 0.05/n$ where n is the number of comparisons). Results are presented with 95% confidence intervals. In the figures, the asterisk signifies the following: * $p < 0.05$, ** $p < 0.01$, *** $p < 0.001$.

4.7 Efficacy of the measurement platform

The measurement platform successfully allowed to subdivide and analyse the local and global morphometry of the RCAs and LCAs in all patients. For vertebral arteries (VAs), the platform failed to detect point e_1 of RVAs in only 2/106 patients due to unmet criterion on longitudinal coordinate. The morphometric measures of tracts I were extracted in 98/106 and 101/106 patients, and of tracts II in 41/106 and 43/106 patients, depending, for each case, on the availability of imaging data and amount of reconstructed vessel. Since complete morphometric analysis of VAs including global and local measures of tracts I and II was available for a reduced subset of patients, only the tests regarding tract I are presented.

4.8 Comparison of vascular morphometry and flow between normotensives and hypertensives

While global and local morphometry of carotid arteries did not significantly differ between hypertensives and normotensive controls, the morphometry of VAs was different between the two groups: hypertensives had longer ($p = 0.002$) and more tortuous ($p = 0.006$) RVA but similar LVA comparing to normotensive controls. Flow in hypertensives was lower in RCA ($p < 0.001$), LCA ($p < 0.001$), basilar artery (BA) ($p = 0.01$), RVA ($p = 0.03$) but not in the LVA ($p = 0.8$).

We also evaluated intra-patient differences between right and left side. Local lateral differences were observed in both carotid and vertebral arteries of normotensive controls. In hypertensives, such morphometric asymmetry was preserved in the carotids but not in the vertebral arteries. More specifically, in all subjects, RCA and LCA were globally similar but presented local differences in tract I and II: LCA had less tortuous ($p = 0.01$ for normotensives, $p < 0.001$ for hyper-

4.8. Comparison of vascular morphometry and flow between normotensives and hypertensives

tensives) and shorter ($p = 0.005$ for normotensives, $p = 0.008$ for hypertensives) tract I, and more tortuous ($p < 0.001$ for normotensives, $p = 0.03$ for hypertensives) and longer ($p < 0.001$ for normotensives, $p = 0.002$ for hypertensives) tract II. On the other hand, LVA were longer ($p < 0.001$), more tortuous ($p < 0.001$) and larger ($p = 0.001$) in normotensives, and had greater tortuosity ($p < 0.001$) but comparable length ($p = 0.2$) and cross-sectional area ($p = 0.1$) in hypertensives. Carotid flow was always symmetric ($p = 0.2$ for normotensives and hypertensives), whilst vertebral flow was always asymmetric with lower left perfusion ($p = 0.002$ for normotensives, $p = 0.009$ for hypertensives). See figures 4.1 and 4.2 for the graphical representation of the results.

To summarize, for the carotid arteries:

- Hypertensives have similar carotid morphometry comparing to normotensives;
- Hypertensives have lower carotid blood flow comparing to normotensives;
- Both normotensives and hypertensives have LCA with less tortuous and shorter tract I than RCA;
- Both normotensives and hypertensives have symmetric carotid flow.

For the vertebral arteries:

- Hypertensives have longer and more tortuous RVA, but similar LVA comparing to normotensives;
- Hypertensives have lower blood flow in RVA, but similar blood flow in LVA comparing to normotensives;
- Normotensives have longer, more tortuous and larger LVA than RVA. Hypertensives have more tortuous LVA than RVA, but length and cross-section is similar between the two vessels;

- Both normotensives and hypertensives have asymmetric vertebral flow, with lower left perfusion.

4.9 Associations between vascular morphometry and blood flow

Carotid blood flow did not correlate with global morphometric features of carotid arteries neither in normotensives nor in hypertensives. On the other hand, vertebral blood flow in hypertensives was negatively associated with length of local tracts of RVA ($r = -0.34$, $p = 0.007$) and, more weakly, of LVA ($r = -0.23$, $p = 0.04$). Vertebral flow was negatively associated with cross-sectional area in both groups (in normotensives: $r = -0.3$, $p = 0.042$ for RVA, $r = -0.39$, $p = 0.009$ for LVA; in hypertensives: $r = -0.23$, $p = 0.05$ for RVA, $r = -0.25$, $p = 0.03$ for LVA), but independent of the tortuosity of the investigated tract. Linear regression analysis was conducted regardless side (right and left) and hypertension group to explore a general relationship between vascular morphometry and blood flow. Results confirmed the lack of any significant relationship between global morphometry and flow of carotid arteries, but showed an inverse relationship between vertebral flow and vascular cross-sectional area (intercept = 11.8 ± 0.7 ml/min/dL, angular coefficient = -0.3 ± 0.07 ml/min/dL/mm², $p < 0.001$, *adjustedR*² = 0.09), length (intercept = 15.5 ± 2.2 ml/min/dL, angular coefficient = -0.1 ± 0.03 ml/min/dL/mm, $p = 0.001$, *adjustedR*² = 0.05), but not with vascular tortuosity (intercept = 11.7 ± 1.8 ml/min/dL, angular coefficient = -1.8 ± 1.1 ml/min/dL, $p = 0.1$, *adjustedR*² = 0.009) (Figure 4.3). To summarize:

- Carotid blood flow is not associated with global carotid morphometry neither in normotensives nor in hypertensives;
- Vertebral blood flow might be associated with length and cross-sectional area of vertebral arteries, but not with tortuosity.

4.9. Associations between vascular morphometry and blood flow

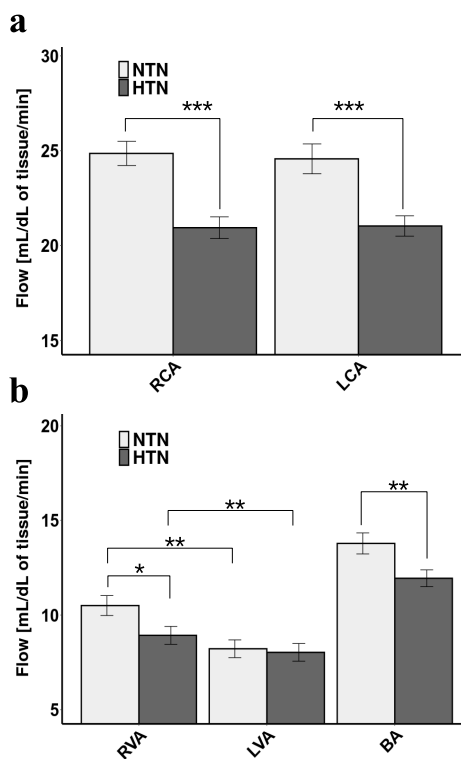


Figure 4.1: Comparison of carotid and vertebral blood flows between normotensive and hypertensive subjects. a) Blood flows in the RCA and LCA were significantly lower in hypertensives comparing to normotensive controls. Carotid flow was symmetric between right and left sides in both groups; b) Blood flows in the RVA and BA were significantly lower in hypertensives comparing to normotensive controls, whereas blood flow in the LVA were similar between the two groups. Vertebral flow was asymmetric between right and left sides in both normotensives and hypertensives. NTN = normotension, HTN = hypertension. Data are shown as mean and standard error of the mean. * $p < 0.05$, ** $p < 0.01$, *** $p < 0.001$.

4. Arterial morphometry, cerebral perfusion and hypertension

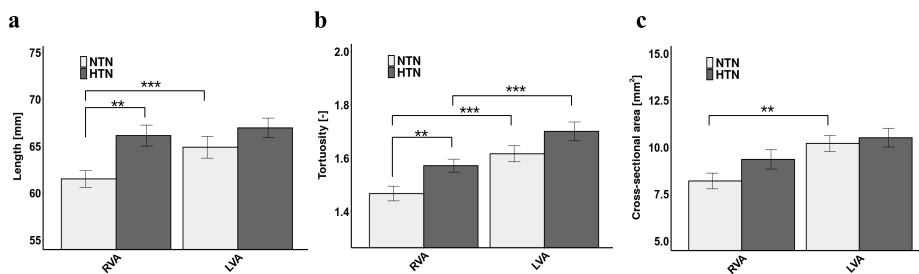


Figure 4.2: Comparison of vertebral morphometry between normotensive and hypertensive subjects. a) Comparison of length: RVAs were longer in hypertensives comparing to normotensive controls, whereas LVAs were similar between the two groups. In normotensives, LVAs were longer than RVAs, but such morphometric asymmetry was absent in hypertensives; b) comparison of tortuosity: RVAs were more tortuous in hypertensives comparing to normotensive controls, whereas LVAs were similarly tortuous between the two groups. In normotensives, LVAs were more tortuous than RVAs, and such morphometric asymmetry was seen also in hypertensives; c) comparison of cross-sectional area: both RVAs and LVAs have comparable cross-sectional area between normotensives and hypertensives. In normotensives, LVAs were larger than RVAs, but such morphometric asymmetry was absent in hypertensives. The morphometric measures refer to the tract I of vertebral arteries. NTN = normotension, HTN = hypertension. Data are shown as mean and standard error of the mean. * $p < 0.05$, ** $p < 0.01$, *** $p < 0.001$.

4.10. Analysis of the results

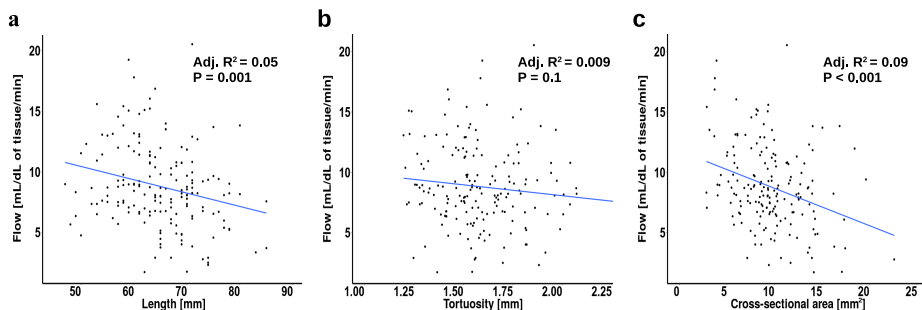


Figure 4.3: Linear regression models between vertebral morphometry and flow. Inverse relationship between vertebral flow and a) length and c) cross-sectional area, but not with b) vascular tortuosity. Linear regression analysis was conducted regardless side (right and left) and hypertension group. * $p < 0.05$, ** $p < 0.01$, *** $p < 0.001$.

4.10 Analysis of the results

This study presents a detailed description of the morphometry of the major intracranial vessels in hypertensive subjects and assesses the role of arterial geometry on cerebral perfusion. Adapting previously proposed methods for the geometric analysis of the internal carotid arteries with intracranial aneurysms [92, 93, 86, 83], a semi-automated platform was implemented to operate a robust anatomic subdivision of both the carotid and vertebral arteries based on the geometric analysis of the centerline, extracting morphometric measures automatically. Carotid flow was lower in hypertensive patients compared to normotensive controls, in agreement with prior observations of reduced total cerebral flow in hypertensives [25]. However, the carotids of hypertensive patients did not present significant geometric differences compared to normotensive. The morphology of the intracranial carotid did not appear to be associated with the reduction of arterial flow in this cohort, in line with the hypothesis that the link between hypertension and morphometry of intracranial internal carotid artery is incidental [81]. Our results showed that LCA was morphologically different to RCA both in hypertensives and healthy

controls, with differences localized at the two most distal investigated segments - i.e. tract I and II. More specifically, tract I was always shorter and less tortuous on the left side, while tract II was longer and more tortuous in all subjects but borderline/pre-hypertensives. Furthermore, carotid blood flow was symmetric in all subjects but borderline/pre-hypertensives, who exhibited a greater left perfusion. Using PC-MR imaging in healthy subjects, McDonald et al. reported that internal carotid blood flow is symmetric in the cavernous and supraclinoid segments, and higher in the left side distally to the bifurcation and in the cervical segment [94]. In this study, carotid flow was derived at the level of the cavernous segments, thus our results confirm that in healthy patients carotid blood flow is symmetric, and show that such a symmetry holds also for hypertensive subjects. Interestingly, borderline/pre-hypertensive patients had higher flow in the LCA and were the only ones presenting similar tortuosity and length of tract II between right and left side. Although we cannot demonstrate causality, we hypothesize that the greater length and tortuosity of tract II in LCA might reduce flow in the most distal segments of the left internal carotid artery, originating from a physiologic asymmetry of blood flow in the arterial system ascribed to the fewer proximal branches in the left arterial circulation as suggested by [94]. Vertebral flow in normotensives was instead asymmetric, with a higher perfusion on the right side, disagreeing with the tendency of higher left vertebral perfusion in healthy subjects [94]. In hypertensives, RVA flow was reduced from 11 ± 3 ml/min/dL to 9 ± 4 ml/min/dL ($p = 0.03$), but continued to be higher than LVA flow, which was on average 8 ± 4 ml/min/dL in both groups ($p = 0.8$). Importantly, basilar flow was also reduced in hypertensives, suggesting that in these patients the LVA was not able to compensate the lowered RVA perfusion. This confirms previous observations by Warnert et al. in a larger, less detailed dataset, where in hypertensive patients the VA did not compensate for the blood flow in the presence of contralateral vertebral hypoplasia [25]. Intriguingly, we observed physiological significant geometric differences between the most dis-

4.10. Analysis of the results

tal segments - i.e. tract I - of RVA and LVA. Healthy subjects had significantly straighter, shorter and narrower tract I in the right side, but such a morphological asymmetry was affected in hypertensives. Our results suggest a possible link between hypertension and vertebral artery geometry, where in particular an increased length and tortuosity might be associated to vertebral flow decrease. Focusing on tract I, this idea is corroborated by the following findings: 1) in both normotensives and hypertensives, LVAs were longer, more tortuous and had reduced flow compared to RVAs; 2) RVAs of hypertensives were more tortuous, longer and had reduced flow compared to RVAs of normotensives; 3) LVAs of hypertensives had similar tortuosity, length, and flow compared to LVAs of normotensives. Regression analysis suggested arterial length as a significant contributor to the reduction of the vertebral flow. Unexpectedly, results showed an inverse relation between vascular calibre and vertebral flow. While numerous studies have proposed vertebral artery hypoplasia as risk factor for posterior cerebral hypoperfusion [95, 82, 96] and for increase in sympathetic nerve activity and BP [78, 77, 25], this may suggest that the length of tract I had a greater influence on vertebral flow than vessel calibre. We suggest a possible relation between the morphometry of specific vascular segments and arterial flow. This is supported by: 1) the presence of less tortuous tract I and a higher LCA blood flow in borderline/pre-hypertensive subjects (results not shown) and 2) the association between the length of tract I and flow in vertebral arteries. There is very little research about haemodynamic alteration induced by vascular morphometry. Wang and colleagues have compared *in silico*, *in vitro* and clinical observations of carotid artery kinking, reporting a drop of mean arterial pressure depending on the angle of kinking [97]. However, the association of carotid flow and tortuosity was not investigated. Our results validated the notion that arterial morphometry may alter haemodynamics, although a more extensive investigation is required.

4.11 Final comments and future developments

In this chapter, we have showed that the geometry of the intracranial carotid arteries was not clearly responsible for the reduction of carotid flow in hypertensives, while the geometry of the vertebral arteries could be responsible for the reduction of their vertebral flow. This study adds evidence to the hypothesis that the morphometry of vertebral arteries may be involved in the onset of essential hypertension, paving the way for supplemental diagnostic evaluation and risk assessment of this pathology. However, further studies in larger cohorts of age and sex-matched participants are warranted to confirm these findings.

Also, we acknowledge some limitations as discussed in the following. First, while this study details the morphometry of the major cerebral vessels focusing on the intracranial segments, the blood flow reduction observed in hypertensives might have been affected also by the extracranial tracts. Previous work pointed out the morphological variability of the cervical internal carotid artery [98], stressing a possible association with arterial flow reduction in hypertensives [99, 100, 27]. A future, more comprehensive morphometric analysis could include also the extracranial segments.

Second, the study is limited by its cross-sectional nature. We cannot establish if the morphometric differences observed in hypertensive subjects were present before (and, thus, might be responsible for) the onset of the pathology or be acquired as an effect of age- and/or hypertension-related remodelling. A longitudinal study could shed light on this aspect.

Another potential caveat is that some hypertensive patients were taking anti-hypertensive medications at the time of screening. Antihypertensive treatment has been demonstrated to correct arterial remodelling by acting on the arterial/venous vasodilatation [104]. Although there is no evidence of the effect of antihypertensive drugs on arterial tortuosity or length, especially for great intracranial ves-

4.11. Final comments and future developments

sels, we acknowledge that the morphometric analysis of the major intracranial vessels might be affected by the type and duration of blood pressure treatment and further studies will have to investigate this aspect.

4. Arterial morphometry, cerebral perfusion and hypertension

Chapter 5

From systemic to local risk factor: implementation of a simulation framework to assess carotid hemodynamics after carotid stenting

5.1 Introduction

Carotid artery stenting (CAS) is a surgical procedure aiming at increasing the blood flow in a stenosed carotid artery by expanding a metal-mesh tube, called a stent, to re-open the narrowed lumen. Although this technique effectively restores the blood perfusion, post-operative complications may arise, of which the most frequently reported is in-stent restenosis (ISR), i.e., the formation of neointimal tissue producing a new stenosis in the stented vessel within months after the intervention [49]. As one of the plausible causes of ISR is the

endothelial injury provoked by the anomalous hemodynamic stresses after the stent implantation [15], the estimation of local aspects of the post-CAS hemodynamics is particularly important to select the best stent implant in terms of size, design, and positioning of the endovascular device. Differently from the previous chapters, in which morphometric and flow data were measured directly from the medical images of hypertensive patients, it is advisable to measure such aspects *before* the implantation of the stent in order to plan the surgical intervention, i.e., we need to *simulate* the stenting condition and the resulting hemodynamics. Computational fluid dynamics (CFD) is a widely used tool to compute local blood flow characteristics in patient-specific vascular models simulating different pathological scenarios, but the modelling of post-CAS condition including the implanted stent is not trivial and presents some complexities that need to be addressed. In the following sections, we first provide a background of the main concepts and steps to analyze the hemodynamics of blood vessels by means of CFD simulations. Then, we review the methods for the CFD analysis of post-CAS hemodynamics. After a focus on the “immersed approach”, we present the creation of an innovative framework for the simulation of post-CAS hemodynamics exploiting such strategy for the inclusion of the stent inside the fluid domain. Finally, grid and time-step sensitivity analyses on simple problems for the tuning of the simulation parameters are presented.

5.2 Computational techniques for hemodynamic analysis of blood vessels

5.2.1 Equations and material properties

The physics of mass, momentum, and heat transfer can be described by a set of partial differential equations (PDEs), called the Navier-Stokes equations (NSE). Being solvable analytically only in

5.2. Computational techniques for hemodynamic analysis of blood vessels

very simple problems (e.g., steady flow in a perfectly cylindrical tube with rigid walls), the NSE must be discretized and solved numerically by means of CFD. We model the blood flow by the unsteady incompressible NSE for a Newtonian fluid. The continuity equation reads:

$$\nabla \cdot \mathbf{u} = 0 \quad (5.1)$$

The momentum equation reads:

$$\rho \frac{\partial \mathbf{u}}{\partial t} + \rho(\mathbf{u} \cdot \nabla)\mathbf{u} - \mu \nabla \cdot (\nabla \mathbf{u} + \nabla \mathbf{u}^T) + \nabla p = \mathbf{0} \quad (5.2)$$

where $\mathbf{u}(\mathbf{x}, t)$ is the velocity vector field, $p(\mathbf{x}, t)$ is the pressure scalar field, t is the time, \mathbf{x} is the position vector in the 3-D domain, μ is the dynamic viscosity set to 0.04 P, and ρ is the blood density set to 1.040 g cm^{-3} . The assumption of Newtonian rheology has been demonstrated to be reasonable for image-based CFD simulations of flow in the carotid bifurcation with respect to both bulk flow metrics [64] and wall shear stress (WSS) based metrics, although more loosely for time-averaged wall shear stress (TAWSS) [64], but still acceptable compared to other sources of uncertainty (i.e., uncertainty on geometry reconstruction) [65].

The NSE must be equipped with appropriate boundary conditions (BCs). The choice of the BCs depends on the type of simulation, model complexity and availability of clinical data. According to [66], in this dissertation the CFD simulation of the stented carotid bifurcation was achieved by prescribing a time-dependent fully-developed parabolic velocity profile at the common carotid artery (CCA), a null static pressure at the external carotid artery (ECA) and an outflow at the internal carotid artery (ICA) guaranteeing a flow split ICA/ECA equal to 65/35 (figure 5.1). Finally, the vascular model was considered rigid, thus a no-slip condition on the velocity field was prescribed at the walls.

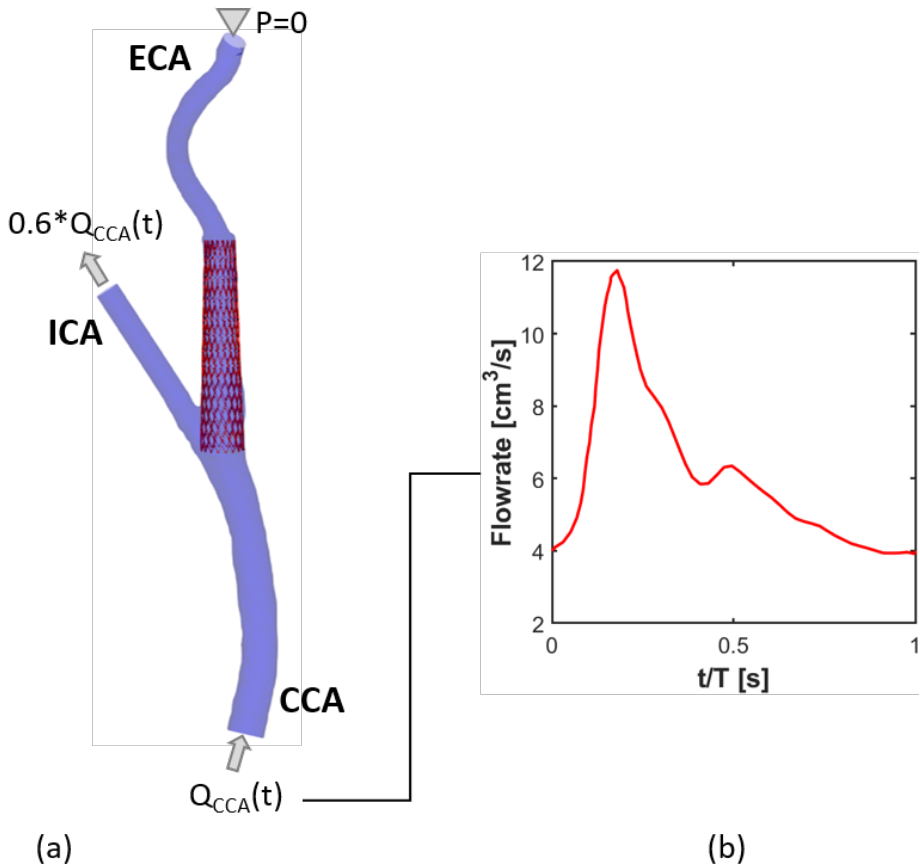


Figure 5.1: Boundary conditions employed for the CFD simulation in the stented carotid model. A time-dependent fully-developed parabolic velocity profile at the CCA, a null static pressure at the ECA and an outflow at the ICA guaranteeing a flow split ICA/ECA equal to 65/35. T is the duration of one cardiac cycle. Flowrate reproduced from Marshall et al. [121].

5.2.2 Computational domain

The NSE are solved in the 3-D domain representing the carotid artery. However, the vascular surface resulting after the segmentation process has to be processed in order to correctly set up the simulation and improve the accuracy of the solution. Cylindrical flow extensions are plugged at all the inlet and outlet sections of the model. This approach allows to:

- have flat and circular sections at the inlet and outlets of the model, so that, in case of fully-developed Dirichlet boundary conditions, Poiseuille or Womersley velocity profiles can be specified analytically;
- the boundaries can be easily labelled for the prescription of boundary conditions;
- to impose the BCs a few diameters far from the region of interest to limit their influence on the blood flow inside the artery. Such an approach is more common for the inlet to allow full flow development [67], but has been proven also to help managing backflow stabilizations at the outlets [68].

An example of cylindrical flow extensions plugged at the inlet and outlet sections of a carotid model is shown in figure 5.2.

5.2.3 Meshing

In order for the NSE to be solved numerically, the computational domain must be discretized into a computational mesh. The volume is broken down into a collection of elementary cells and points, called elements and nodes, respectively. The equations are then solved inside the elements and the solution is given as a collection of values at the nodes. An optimal trade-off between mesh resolution and computational cost is a key aspect to consider during this phase. Fine meshes are able to better capture the characteristics of the physical

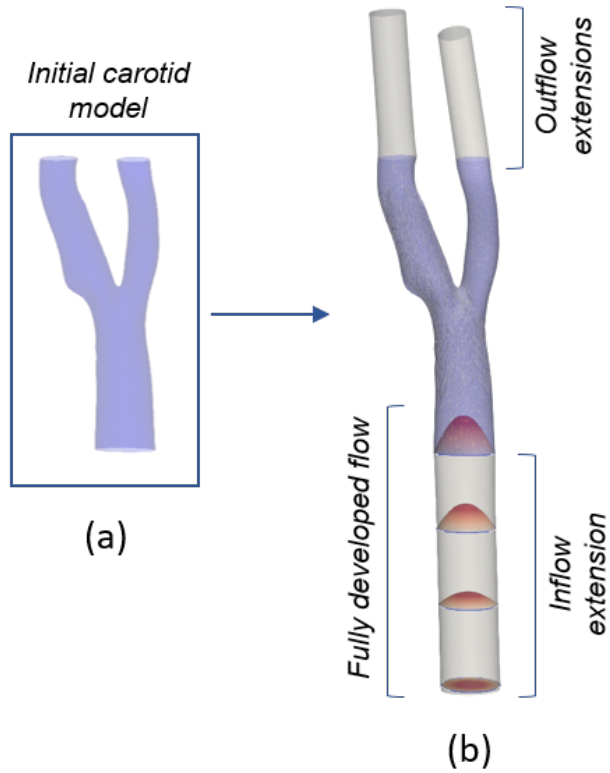


Figure 5.2: Cylindrical flow extensions at the inlet/outlet sections of a carotid model. a) The initial model is the surface representation of a carotid artery extracted from medical images; b) cylindrical flow extensions (in grey) are plugged at the inlet and outlet sections in order to limit the effect of the BCs on the blood flow inside the region of interest (in blue), e.g., a flat velocity profile imposed at the inlet develops into a parabolic velocity profile inside the inflow extension before entering the region of interest.

phenomenon, but lead to problems with a large number of unknowns that require longer computational time. A way to tackle the problem is the local mesh refinement, consisting of employing fine meshes where needed (regions with high Reynolds number, clinical interest of the solution, geometric accuracy), leaving a coarser mesh elsewhere to reduce the computational cost. As the solution may change depending on the resolution of the mesh, it is crucial to ensure that the numerical solution is mesh-independent. It is good practice to carry out a mesh-independence study (sensitivity analysis): the solutions of the same problem are obtained with increasingly finer meshes until no variation is observed, thereby achieving the spatial convergence of the results. For CAS simulation, we will exploit tetrahedral meshes because of their versatility to conform to the complex boundaries of the carotid arteries. Since the near-wall hemodynamics is of great clinical interest, as it is directly linked to WSS and derived quantities, we will also prescribe a high element density near the wall. Tetrahedral elements will be adopted also for this purpose to guarantee compatibility with any unstructured solver.

5.2.4 Solution of the Navier-Stokes equations

Having provided the correct BCs and material properties, and having discretized the spatial domain into a computational mesh, the NSE can be solved numerically. The outcome consists of an approximation of the value of each variable in the equations 5.1 and 5.2 at the nodes of the computational domain. We adopt the commercial solver Ansys CFX under academic licence (Ansys Academic Research CFX, Release 2020 R1), because it natively provides the “immersed solid method”, which will be exploited to take into account the immersed stent in the carotid artery during the development of the framework for the simulation of CAS. For a comprehensive overview of the characteristics of the employed solver, the reader is reminded to the relative documentation [69]. Theoretical and implementation details of the “immersed solid method” will be given in section 5.5

instead.

5.2.5 Hemodynamic quantities of interest

The final phase of the simulation workflow consists of the post-processing of the results. The solution of the equations provides the value of the variables of interest at all the points of the computational mesh. Although such quantities suffice to describe the physics of the phenomenon, they can further be combined to build metrics that, in turn, can be particularly meaningful in different clinical scenarios. In the following section a review of such quantities and their clinical importance in the context of atherosclerosis is presented. The velocity field is used to draw the streamlines and visualize flow patterns, which is particularly useful to evaluate detailed hemodynamics or predict these during the design or intervention planning of endovascular devices [70]. On the other hand, the blood pressure field can be used to compute the power loss across a stenotic artery [71]. The velocity field can be used to derive other quantities also of clinical significance. The frictional force exerted by blood flow on the vessel wall is quantified by the WSS, whose spatial distribution can be obtained multiplying the gradient of the velocity and the blood viscosity. WSS is a vector, thus has a modulus, direction and verse that vary in time during the cardiac cycle. The importance of WSS on vascular remodelling and pathology has been extensively demonstrated: low and oscillatory WSS lead to endothelial dysfunction which initiate the atherogenic cascade [72], high WSS may damage the endothelium and lead to aneurysm formation [73] or dissection [74]. WSS-derived metrics have been adopted to synthesize the temporal evolution of WSS and describe a specific biological effect. For instance, TAWSS is the temporal average of the WSS modulus, oscillatory shear index describes the oscillation of the WSS and particle residence time is linked to the stagnation of blood particles at the vessel wall.

5.3 Methods for the hemodynamic simulation of the stented carotid and related issues

Although CFD is a widely used tool to compute blood flow in patient-specific vascular models simulating different pathological scenarios, the creation of post-CAS condition including the implanted stent is not trivial, and this explains the small number of studies addressing this aspect [105, 31, 54, 53] (summarized in figure 5.3). If the CFD simulations is done in the post-operative phase, a possible strategy is to reconstruct the post-stenting carotid geometry from medical imaging (figure 5.4); however, in general the stent geometry is not directly obtainable from the images due to blurring of the metal struts [106], unless high resolution imaging techniques and dedicated reconstruction tools are used [107]. Therefore, different methods for the virtual stent deployment in the post-stenting carotid geometry have been proposed. Johari et al. mapped the sketch of the stent cells onto the vascular surface of the post-stenting carotid, then performed boolean operations to remove from the post-CAS vessel the region occupied by the stent and carry out the CFD analysis testing the flow impact of three different stent designs [105]. Kabinejadan et al. included in the post-stenting carotid only the portion of the stent at the ECA ostium by simply aligning the free-configuration of the stent to the vascular centerline, then bending the stent by FE simulation according to the carotid geometry, and finally cropping the deformed configuration of the stent to extract the portion of interest inside the vessel lumen [54]. These strategies are computationally inexpensive, but have two main disadvantages. First, they do not simulate the actual deformation of the implanted stent, thus potentially miss important aspects of the post-CAS configuration such as stent mal-apposition [30]. Second, they require that the post-stenting carotid geometry is already available from the medical images, making impossible to use the CFD to *predict* the post-CAS

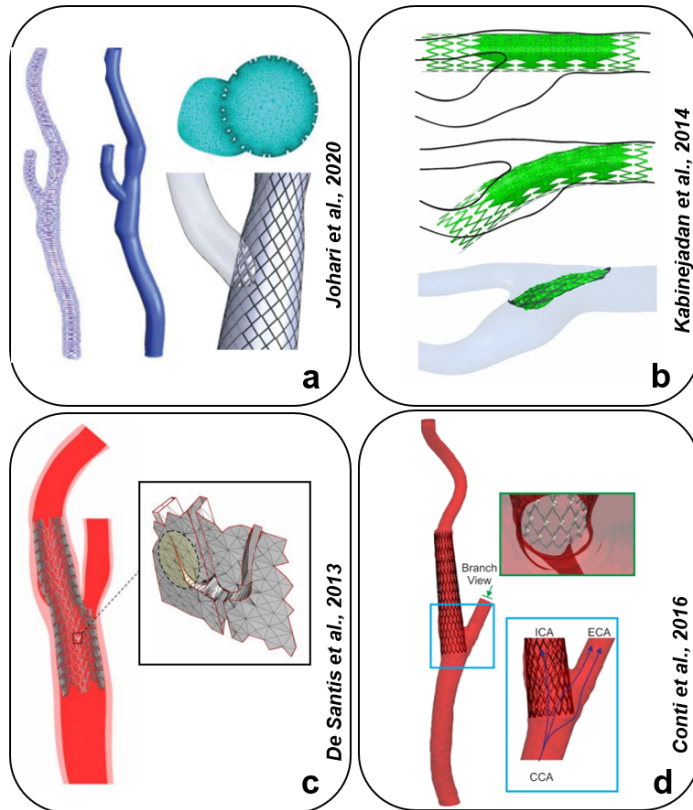


Figure 5.3: Literature review of the methods for the inclusion of the endovascular device in the blood domain in CFD analyses of post-CAS hemodynamics. a) Johari et al. mapped the sketch of the stent cells onto the vascular surface of the post-stenting carotid, then performed boolean operations and built a body-fitted mesh [105]; b) Kabinejadan et al. aligned the free-configuration of the stent to the vascular centerline, then bent it by finite element (FE) simulation, and cropped it to extract the portion of interest [54]; c) De Santis et al. implemented an algorithm to eliminate small gaps and “repair” the stent surfaces before generating the body-fitted mesh [30]; d) Conti et al. aligned the free-configuration of the stent to the vascular centerline, then adopted a “penalty method” implemented in an in-house CFD code to simulate post-CAS hemodynamics [31]. Adapted from [105, 31, 54, 53].

5.3. Methods for the hemodynamic simulation of the stented carotid and related issues

hemodynamics, as for instance during the surgical planning in the pre-operative phase. In this case, the preferred approach is the sequential use of mechanical simulations [108]. Initially, a structural simulation of the stent deployment is performed [109]. With this, it is possible to study the mechanical forces arising from the stent/vessel interaction and extract the post-CAS stent and carotid geometries. The last are used in the second step of this workflow to build the post-CAS computational fluid domain and perform the CFD simulation with the immersed stent.

In figures 5.4 and 5.5 we show the steps that should be taken to produce a patient-specific carotid model to extract structural, geometric and hemodynamic information in the above described cases.

Whatever is the method chosen to position the stent inside the vascular model and obtain the post-CAS stent-vessel configuration, the construction of the post-CAS computational fluid domain and its discretization into a valid computational grid contains some technical difficulties. In particular, the problem arises when the computational fluid domain is obtained through a boolean operation, i.e., the volume occupied by the endovascular device is “subtracted” from the total volume. The result of this operation is a computational grid that *lives* uniquely in the physical fluid domain; it is a “body-fitted” grid because the element faces at the boundaries of the immersed body perfectly match up with its surfaces (an example of body-fitted grid is given in the left pane of figure 5.6). This approach has the advantage of accurately resolving both the geometry of the immersed object both its effect on the flow field because the no-slip BCs can be strongly enforced at its surfaces, but performing boolean operations when such surfaces are non-analytical, as occurs in medical imaging, commonly produces mesh errors such as non-manifold edges, self-intersecting triangles and finite gaps. Furthermore, the stenting application is critical because the stent struts are very thin: numerical approximations occurring during the contact algorithm in the FE solver and the boolean operations cannot be solved by diminishing the geometrical tolerance or by cleaning the final surface using a

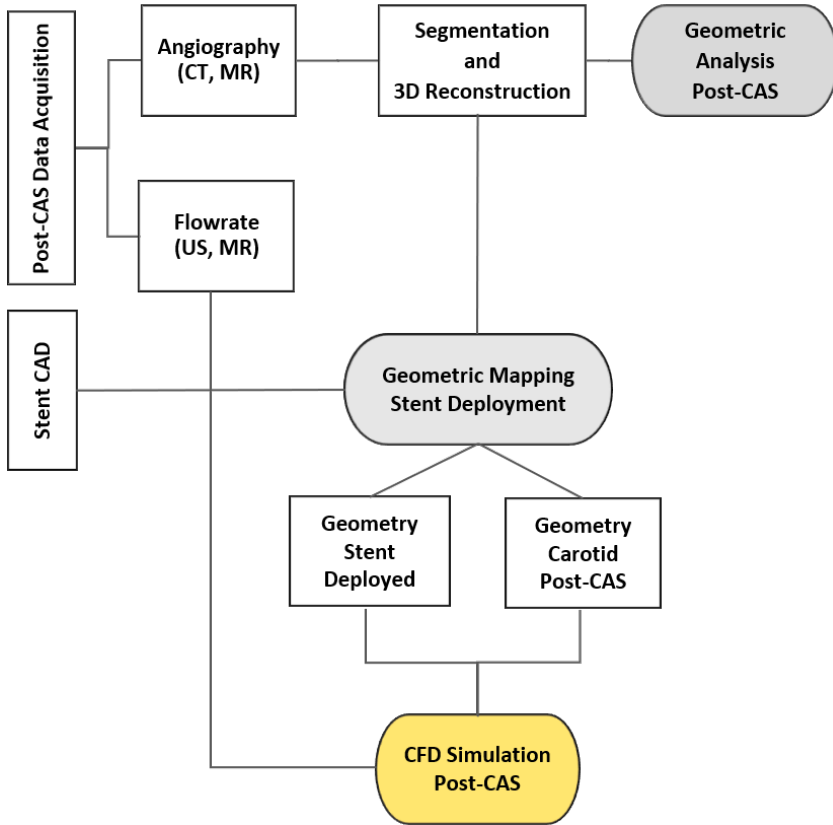


Figure 5.4: Workflow to perform the geometric and hemodynamic analysis of post-stenting carotid artery from post-operative imaging data. The inputs of the workflow are the vertical boxes on the left side of the figure. Patient’s data include angiographic data to reconstruct the post-CAS vascular geometry, and flow data to apply patient-specific BCs in the fluid dynamic simulations. As the implanted stent cannot be extracted from the medical images due to blurring of the metal struts, the CAD representation of the stent has to be used in order to reconstruct the post-CAS model of carotid artery with the implanted stent. This can be achieved by positioning the stent through rigid rototranslation, or by mapping its geometry onto the post-CAS vascular wall. Then, the post-CAS geometries of the stent and carotid are extracted and used to perform the geometric and hemodynamic analysis of the post-CAS configuration. The yellow box, i.e. CFD simulation of post-stenting carotid, is the focus of this work. CAD = Computer-aided designed, CAS = Carotid Artery Stenting, CFD = Computational Fluid Dynamics, MR = Magnetic Resonance, US = Ultrasound.

5.3. Methods for the hemodynamic simulation of the stented carotid and related issues

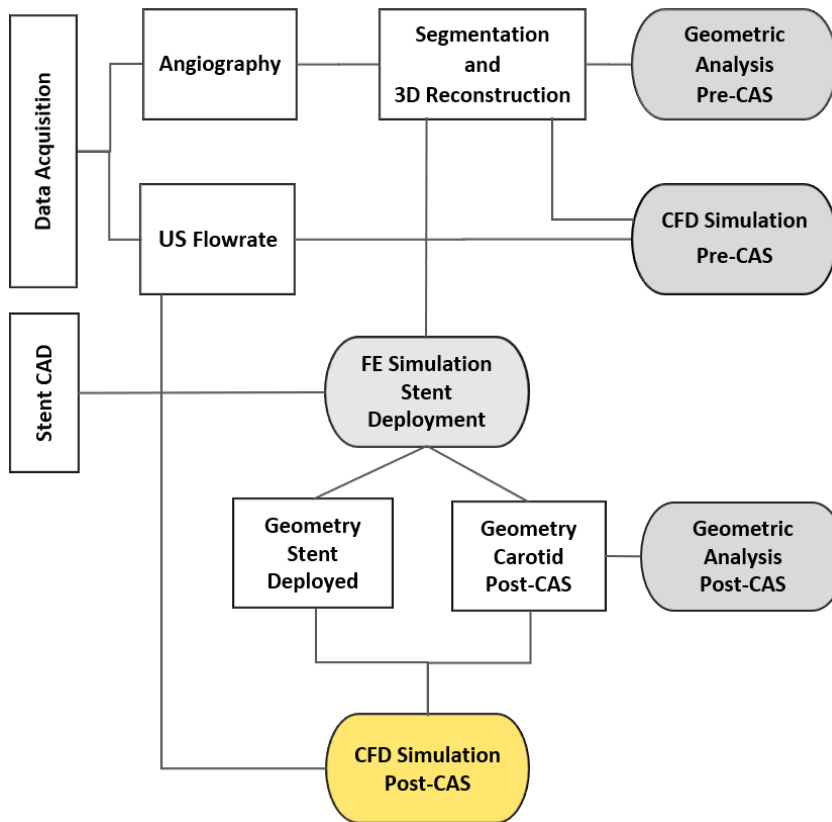


Figure 5.5: Workflow to perform the geometric, structural, and hemodynamic analysis of pre- and post-stenting carotid artery from pre-operative imaging data. The inputs of the workflow are the vertical boxes on the left side of the figure. Patient’s data include angiographic data to reconstruct the pre-CAS vascular geometry, and flow data to apply patient-specific BCs in the mechanical simulations. The CAD model of the stent can be available from the manufacturer or can be generated from imaging techniques. The reconstructed carotid model is used to perform the geometric and hemodynamic analysis of the pre-CAS configuration, and the FE simulation of virtual stent deployment. Then, the post-CAS geometries of the stent and carotid are extracted and used to perform the geometric and hemodynamic analysis of the post-CAS configuration. The yellow box, i.e. CFD simulation of post-stenting carotid, is the focus of this work. CAD = Computer-aided designed, CAS = Carotid Artery Stenting, CFD = Computational Fluid Dynamics, FE = Finite Element, MR = Magnetic Resonance, US = Ultrasound.

smoothing algorithm because of the risk of losing the cross-sectional strut shape or even filtering out the strut. To overcome such an issue, De Santis and colleagues developed an *ad hoc* computational method based on surface triggering to eliminate small gaps and “repair” the stent surfaces before generating the body-fitted fluid domain mesh [30]. Then, they applied the methodology in a comparative study in which they evaluated the impact on carotid hemodynamics of open- and closed- cell stent designs [53].

On the other hand, Conti et al. [31] used an alternative approach for the generation of the computational fluid domain of the post-stenting carotid artery starting from the carotid and stent surfaces which overcame the “repairing operation” proposed by de Santis [30]. Indeed, they adopted a “penalty method” (i.e., an “immersed method”) to account for the presence of the stent in the fluid domain. Differently from the body-fitted case, an immersed grid does not conform to the surfaces of the endovascular device and *lives* also inside its volume (an example of immersed grid is given in the middle and right panes of figure 5.6). The effect of the immersed object on the flow field can be achieved by adding a “penalty term” in the NSE at the elements inside and near the body rather than building up a conforming mesh around its surfaces, eliminating the above mentioned difficulties associated with the generation of body-fitted grids, and considerably simplifying the meshing phase. In their preliminary study, Conti and colleagues proposed an in-house CFD code with penalty approach to simulate the blood flow in a pre- and post-stenting carotid artery. In that study, the authors virtually deployed the stent in its free configuration by rigid rototranslations according to the post-stenting carotid geometry. The method showed its potentialities but also its limits: the computed velocity field had unacceptable accuracy near and inside the immersed object even in the toy problems proposed by the authors.

Since in this kind of techniques the surfaces of the immersed object are not explicitly defined, a very fine mesh in the neighbourhood of the endovascular device is needed to attain an acceptable accu-

5.3. Methods for the hemodynamic simulation of the stented carotid and related issues

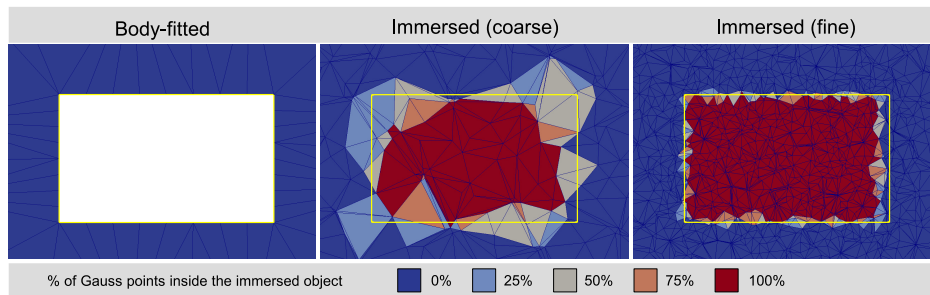


Figure 5.6: Comparison between “body-fitted” and “immersed” grids. In the left pane, an example of “body-fitted” grid around an immersed object with rectangular section. In the middle and right panes, an example of “immersed” grids around the same object (whose boundaries are superimposed in yellow for simplicity) with two different levels of refinement. Each element of the grid is coloured depending on the percentage of its Gauss points - as a surrogate of its volume - falling inside the immersed object. This figure shows how important is the refinement of the mesh to approximate the shape of the immersed object when using an immersed method.

racy of the solution and approximation of the endovascular shape. Again, the stenting application is critical because if the element size was constant over the computational domain, the significant thinness of the stent struts would lead to extremely large and computationally expensive meshes. Therefore, the local mesh refinement is a key strategy for this application, allowing to build up computational grids with very small elements only near the surfaces of the endovascular device while keeping the mesh sufficiently coarse elsewhere, achieving a good accuracy on the solution over the whole domain with a high computational efficiency. Such an issue has been highlighted by numerous studies involving the simulation of blood flow around endovascular bodies with immersed/embedded approaches, exploring *ad hoc* meshing techniques to achieve locally refined grids [110, 111].

5.4 Goal of the study

The workflow to set-up a CFD simulation of a patient-specific post-CAS model is shown in figures 5.4 and 5.5 and consists of a sequence of steps in which specific programs exchange data through standard file formats. On the other hand, several meshing libraries are available to perform complex operations on the mesh including local mesh refinement. In this context, the first goal of this study is to create a framework for the simulation of post-CAS hemodynamics with the immersed approach in which the fluid mesh is locally refined in proximity of the endovascular device. To achieve this task, we first implement a meshing tool for the semi-automatic local mesh refinement in section 5.6, and we set-up the CFD analysis with immersed approach using a commercially available software, tuning the meshing and simulation parameters for our target problem in sections 5.7 and 5.8. The second goal of this study is to show an illustrative application of the developed framework in a comparative analysis of different stent implants in the carotid artery to evaluate their effect on the post-CAS hemodynamics. This second part of the study will be accomplished in the next chapter.

5.5 The “immersed solid method”

We adopt the “immersed solid method” implemented in Ansys CFX to perform the transient CFD simulation of the stented carotid artery. In the following, we briefly describe how the method is implemented in Ansys CFX together with some related modelling issues. The reader interested in the details is reminded to the Ansys CFX documentation [112, 69].

To set-up the simulation, the meshes of the endovascular device (solid domain) and carotid lumen (fluid domain) must be ready. On one side, the spatial configuration of the “deployed” stent and, thereafter, its mesh, can be obtained by rigidly positioning the undeformed (free configuration) stent in the vessel, or by mapping its geometry onto

5.5. The “immersed solid method”

the vascular surface, or after a FE simulation of virtual stent deployment. On the other side, the surface mesh of the carotid lumen is generated according to the meshing framework proposed later on in this chapter. Successively, the endovascular device is “immersed” in the carotid artery by superimposing the two meshes. The CFD simulation proceeds by solving a modified version of the NSE: forcing terms are added in the momentum equation 5.2 to take into account the presence of the endovascular device in the blood flow field. More specifically (in the following, the reader may refer to figure 5.7 for the nomenclature of the points and nodes), three forcing terms (one for each direction), having the dimension of force per unit volume, are added in the momentum equation only at the nodes that lie inside the immersed solid (nodes IW) to drive and force the fluid velocity towards the immersed solid velocity (Dirichlet velocity condition). The forcing terms read:

$$S_x = -KC(U_x - U_{x,solid}) \quad (5.3)$$

$$S_y = -KC(U_y - U_{y,solid}) \quad (5.4)$$

$$S_z = -KC(U_z - U_{z,solid}) \quad (5.5)$$

where U is the fluid velocity, U_{solid} is the immersed solid velocity - which is zero as the stent is considered a fixed rigid body -, C is the momentum source coefficient, automatically computed by the solver considering the advection and diffusion contributions from the fluid mesh elements in the immersed solid, K is a user-defined scaling factor controlling how strongly the fluid velocity is enforced to match the immersed solid velocity. Importantly, increasing the momentum source scaling factor K improves the accuracy of the solution inside the immersed body at the expense of stiffening the equation to solve. A scaling factor of 10 is often optimal, although it can be decreased if robustness problems are encountered, but at the expense of accuracy. For what concerns the description of the flow around the immersed stent, we adopt a laminar flow model with a modified forcing term acting on the nodes near the immersed boundaries (nodes NW). This

allows to take into account the presence of the boundary layer and to prevent the blood to penetrate inside the immersed body. The fluid velocity at the near wall nodes (identified through the “search through element” algorithm) is therefore:

$$U_{NW}^F = (U_{IB}^{IMS})_{norm} + (U_{NW}^F)_{tang} \quad (5.6)$$

Here, $(U_{IB}^{IMS})_{norm}$ is the normal component of the velocity at the immersed boundary point (point IB) on the immersed boundary. The tangential fluid velocity at the near-wall fluid nodes is instead:

$$(U_{NW}^F)_{tang} = (U_{IB}^{IMS})_{tang} + \frac{\mu_{FL}\Delta y}{\mu_{NW}(\Delta y)_{NIBF} + \Delta y} [(U_{FL})_{tang} - (U_{IB}^{IMS})_{tang}] \quad (5.7)$$

where $(U_{NW}^F)_{tang}$ is the tangential component of the forcing velocity at the NW node, μ_{NW} is the dynamic viscosity at the NW node, μ_{FL} is the dynamic viscosity at the FL node, U_{FL} is the fluid velocity at the FL node, $(\Delta y)_{NIBF}$ is the distance between the corresponding FL' point and NW node, Δy is the distance between the NW node and the IB point along the wall normal direction.

5.6 Semi-automatic local mesh refinement: the proposed approach

The meshing tool for the local mesh refinement around an immersed endovascular device has to be:

- Semi-automatic, so that the user can still visually control which regions need to be refined (and which not) and control some mesh characteristics, while the repetitive tasks are carried out automatically;
- Flexible, to easily generate locally refined meshes for any complex geometry of the endovascular device and hosting vessel, a feature particularly useful to test multiple stent implants in a quick way;

5.6. Semi-automatic local mesh refinement: the proposed approach

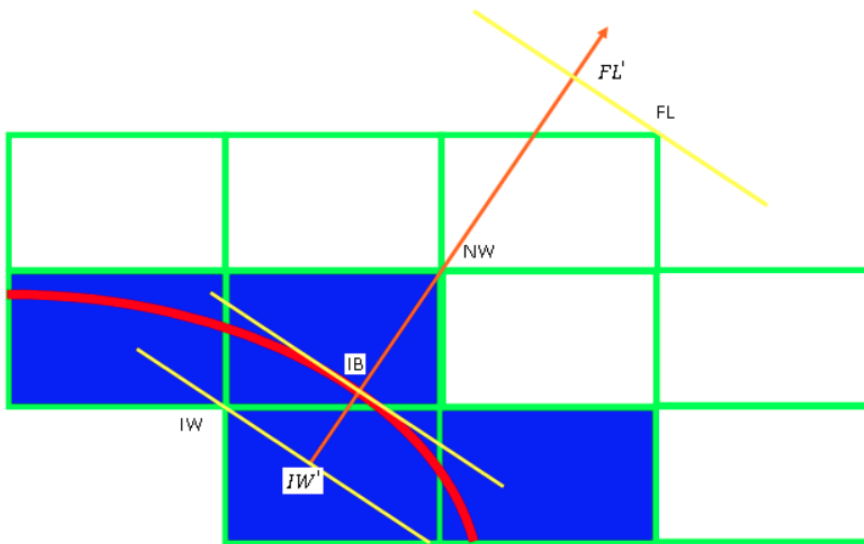


Figure 5.7: Schematic representation of immersed solid boundary in Ansys CFX. The immersed solid boundary is depicted as a red line. The nodes and points near the boundary are labelled as following: FL = fluid node, FL' = fluid point, IB = point on the immersed solid boundary, IW = in-wall node, IW' = in-wall point, NW = near-wall node. Reproduced from [69].

- Versatile, to work with any type of vessel and/or endovascular device, so that it may be used in different applications.

Furthermore, the tool has to naturally fit into the workflow described in figures 5.4 and 5.5.

We provide an overview of the proposed design in the following (figure 5.8). Then, in the next sections, we will detail each component. In particular, in section 5.6.1 we provide some theoretical notions of the meshing algorithm and libraries used, in section 5.6.2 we describe how the mesh generation is performed to achieve the particular task of refining the mesh around the endovascular device; in section 5.6.3 we show how the domain boundaries are labelled to facilitate the application of the BCs during the simulation set-up, finally in section 5.6.4 we describe some operations that the user has to perform for the correct functioning of the proposed meshing tool.

The tool mainly integrates two open-source libraries: Visualization Toolkit (VTK) [113], for the manipulation, repair and 3-D rendering of surface meshes; GMSH [114] for the 3-D grid generation. Such libraries are accessed differently depending on the task to be performed: VTK libraries are used through the GUI of third party programs (e.g., Vascular Modelling Toolkit (VMTK) [59], ParaView [115, 116]) in an interactive manner, while the GMSH libraries are used in API mode, orchestrated by an in-house Python program. The framework requires in input the STL surfaces of both the vascular lumen and the deployed stent. These surfaces are used in two different ways: on one hand, they are the boundaries from which the 3-D meshes of the vessel and of the stent are generated; on the other hand, they constitute the regions where the local mesh refinement has to be performed (eventually, they can be arbitrarily cut so that only sub-regions are employed). The mechanism is the following: the coordinates of the triangle vertices in the STL files are extracted and stored in separated DAT files; then, during the mesh generation, these points are used to centre multiple spheres where the mesh is refined. Although very simple, this approach allows to move from surface meshes (in the STL format) to cloud of points

(in DAT format), considerably simplifying the description of the regions governing the mesh refinement. The core of the framework relies on GMSH libraries and, taking in input the STL and DAT files produced in the previous steps, performs two tasks: (i) automatically identifies the boundaries of the computational domain for an easy application of the BCs during the simulation set up and (ii) generates the tetrahedral mesh with local refinement. Concerning the task (i), different options are available so that the boundary surfaces can be automatically identified in any vessel whatever oriented in space. As for the task (ii), the meshing generation is performed automatically, although the user can control its characteristics through different input parameters. Finally, the tool generates in output two different tetrahedral meshes, one relating to the computational domain where the NSE have to be solved, and the other relating to the stent for the identification of the elements of the fluid mesh inside the immersed body. A schematic diagram of the proposed meshing tool is shown in figure 5.8.

5.6.1 Basics of GMSH

A few theoretical notions concerning the mesh generation component are given in this section, reminding the reader to [114] for further details.

The main reason why we chose GMSH libraries to perform the grid generation is the concept of “mesh size field”. Basically, a “mesh size field” is an analytical function $\delta(x, y, z)$ prescribing the target size of the elements at each point of the computational domain, describing elementary regions such as points as well as more complex spatial distributions. Importantly, multiple size fields can be defined and, if they overlap at the same point, GMSH uses the one with the smaller target size element at that point. During the mesh generation, the mesh size fields constrain the meshing algorithm to create a grid in which each tetrahedral element K :

- Has edges e of adimensional length $l_e = \int_e \frac{1}{\delta(x,y,z)} dl$ close to 1;

5. Carotid stenting, hemodynamics and restenosis

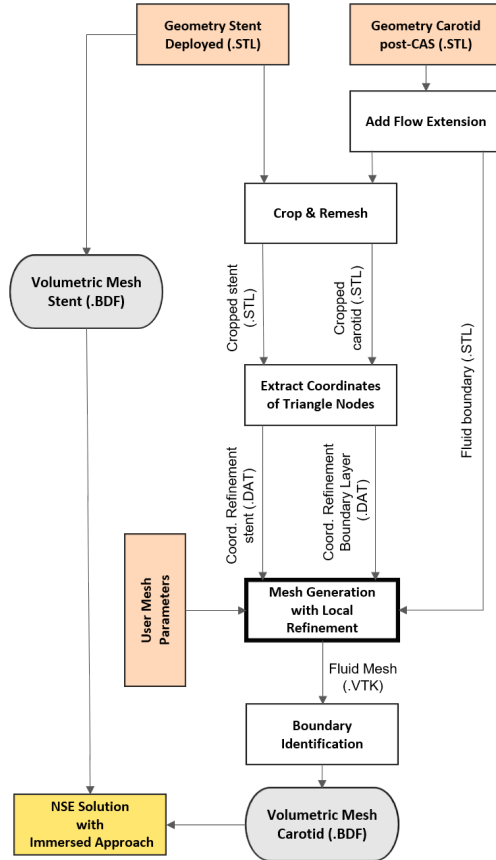


Figure 5.8: Schematic diagram of the proposed tool for the local mesh refinement around the endovascular device. The input data (pink boxes) are the STL geometries of the deployed stent and post-CAS carotid. Such triangulated geometries (or part of them) are used to extract and store in separated DAT files the coordinates of the 3-D points where performing the mesh refinement. The mesh generation component reads the DAT files and some user-defined mesh parameters and performs the tetrahedral mesh generation together with boundary identification. The output data (grey boxes) are the volumetric meshes of the stent and post-CAS carotid that are imported in Ansys CFX for the CFD simulation with “immersed solid method” of CAS hemodynamics (yellow box).

5.6. Semi-automatic local mesh refinement: the proposed approach

- Is *well shaped*, i.e., the measure $\gamma_K = \frac{6\sqrt{6}V_K}{\sum_{i=1}^4 a(f_i) \max_{i=1,\dots,6} l(e_i)}$ is close to 1. In the formula, V_K is the volume of K , $a(f_i)$ the area of the i^{th} face of K , $l(e_i)$ the dimensional length of the i^{th} edge of K .

The generation of the tetrahedral mesh proceeds according to a bottom-up approach in order to ensure the conformity of the mesh to the domain boundaries.

In the general framework, the boundary edges would be initially partitioned to guide the triangulation of the boundary surface which in turn would be exploited for the tetralization of the domain volume. In our case, the first steps are skipped as the boundary surfaces are already triangulated and available in the STL format. The volume tetralization is performed exploiting the open-source mesh generation kernel of Netgen [117], although other algorithms can be used [118, 114]. Finally, the mesh is optimized combining Netgen and in-house optimization algorithms to improve the aspect ratio of each element K in the grid.

5.6.2 Mesh generation

Let us now consider a 3-D domain Ω (e.g., a blood vessel), with boundary surface Γ_Ω , that we want to mesh with an unstructured grid with elements of size¹ l . Consider also a 3-D region Ψ (e.g., a stent), with boundary surface Γ_Ψ , in which we want elements of size l_r , with $l_r < l$.

We now illustrate the proposed meshing approach for a simple case of grid generation refined at a single point P , i.e., $\Psi \equiv P \in \Omega$.

Exploiting the concept of “mesh size field” introduced in section 5.6.1, the strategy consists of building the tetrahedral mesh according to three different regions in Ω , each characterized by three different mesh sizes:

¹Per *element size* we intend the average edge length of the tetrahedron.

- A region Σ , created with a spherical size field centred in P , with arbitrary radius ρ , where the element size is l_r ;
- A region Λ , created with a spherical shell size field centred in P , with internal radius ρ and external radius τ chosen such that the element size grows gradually from Σ to Υ at a prescribed growth rate g_r ;
- A region $\Upsilon = \Omega - \Sigma - \Lambda$, where the element size is l .

A schematic representation of the local mesh refinement at two points P_i is given in figure 5.9.

We now discuss the case with a more geometrically complex Ψ , for which the adoption of the presented approach is straightforward. In fact, it is sufficient to consider a point cloud $P_i \in \Omega$ in place of a single point P , where each point is associated to regions Σ_i , Λ_i and Υ_i . The *distribution* of such a point cloud with respect to the region Ψ determines whether a superficial or volumetric refinement is achieved. In the former case, the point cloud P_i lies on the boundary surface Γ_Ψ (for example, it may be constructed from the triangle vertices of the STL of the same surface). In the volumetric refinement, instead, the point cloud is distributed inside the volume of Ψ (for example, it may be constructed from the nodes of a mesh of the same volume). In a similar way, the cloud point can be constructed from a sub-part of Ψ or Γ_Ψ , allowing to refine the mesh only in specific regions of interest as will be discussed in section 5.6.4.

Finally, a note should be done concerning the symbol of “belonging to” (\in) used for the points P_i in Ω . Such condition *is not* stringent, and this is one of the main strengths of the proposed approach, being particularly useful whenever the endovascular device protrudes outside the lumen vessel due to numerical or modelling reasons. In fact, any point P_i is associated to a spherical size field regardless if it is or it is not in the domain Ω and during the mesh generation only those contributing inside the domain will be used to constrain the size of the elements.

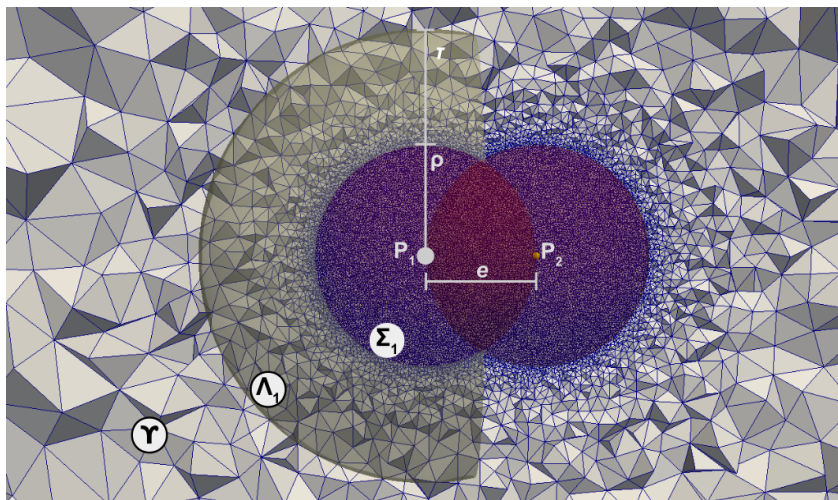


Figure 5.9: Schematic representation of the local mesh refinement and relative parameters. In this example, the mesh refinement was performed at two points P_1 and P_2 at distance e . Two spherical size fields of radius ρ , Σ_1 and Σ_2 (not shown), are centred at these points, where the element size is l_r . Υ is the region where the mesh is not refined, i.e., where the element size is l . Between each spherical size field Σ_i and the unrefined region Υ , two shell-like transition zones of thickness τ , Λ_1 and Λ_2 (not shown), allow a smooth transition of the mesh size with a fixed growth rate. In the figure, the transition region Λ_1 has been narrowed for the purpose of visualization. In this example, $\rho = e$ to allow overlapping of the spherical size fields.

5.6.3 Boundary identification

One of the features implemented within the framework is the automatic selection and labelling of the boundary surfaces of the fluid domain for the application of the BCs. The code starts by breaking down the boundary of the meshed domain into the surfaces of wall, inlet and outlets by grouping the element faces basing on an angle threshold. Then, the labelling of the surfaces proceeds with different criteria: the wall is identified as the one with the largest area, while the inlet and outlets are identified basing on the position of the respective barycentres, whose mechanism of identification depends on whether the domain is a simple vessel (one inlet, one outlet), a bifurcating vessel (an inlet, two outlets) or a more complex vascular structure. In the first case, the selection criterion bases on a user-defined direction (choices: x, y or z) and orientation (choices: increasing coordinate, decreasing coordinate). For example, the input pair (z, increasing coordinate) will separate the surfaces based on their position along the z axis, assigning the label of inlet to the surface with the lowest z-coordinate. In the case of bifurcating vessels, a second direction is assigned for the selection between the two outlets. Finally, in the case of more complex vascular structures, the user can directly enter the approximate coordinates of the inlet and outlets barycentres.

5.6.4 Crop and remesh

As explained in section 5.6.2, the mesh refinement is achieved by locating spherical size fields centred at the points passed to the mesh generation component.

Where and how well the mesh is refined depends on the characteristics of the cloud point: while its distribution determines the position of the refinement, its density defines its quality. This justifies the two operations described in this section.

Let us consider the example in which the mesh is refined at the surface of a stent deployed in the ICA. As already mentioned in section 5.6, a

5.7. Mesh sensitivity analysis in an idealized model of immersed stent strut

convenient choice could be to build the point cloud using the vertices of the triangles in the STL surface of the device. Let us now suppose that we are interested in visualizing the hemodynamic effect of the stent uniquely at the bifurcation; a refinement over the entire surface of the device would unnecessarily increase the computational cost of the simulation. A cropping operation exploiting the VTK libraries through open-source programs such as VMTK or Paraview allows to isolate the region of interest and generate a less numerous point cloud.

As for the quality of the mesh refinement, it depends on the density of the cloud point. To obtain a uniform refinement, the average distance e between two near points P_i has to be small enough in order to ensure adequate overlapping of the spherical size fields Σ_i . Such distance depends on the radius of the sphere ρ , which in turn depends on the number of elements of size l_r desired in the spherical region Σ_i before they start growing in the transition zone Λ_i . In this work, Γ_{Ψ_i} (for the superficial refinement) and Ψ_i (for the volumetric refinement) will be remeshed such that e will be equal to ρ , guaranteeing a good overlapping between adjacent spheres. This concept is illustrated in figure 5.9.

5.7 Mesh sensitivity analysis in an idealized model of immersed stent strut

5.7.1 Motivations

As we have previously pointed out, the “immersed solid method” requires a sufficiently fine mesh around the immersed body in order to allow for effective interpolation of near-immersed-boundary fluid nodes onto the immersed solid [69]. This becomes particularly challenging when the immersed body is thin comparing to the dimensions of the fluid domain, as occurs with stents. A uniform mesh would be impractical due to high computational cost, as its size would be

driven by the smallest element at the thin strut. As discussed before, a local mesh refinement can overcome this issue. Since the intended goal of this study is to simulate the hemodynamic effects of stenting in the carotid artery, it is reasonable to identify a range of physical dimensions that circumscribe the target problem in order to set up an idealized model to assess the suitable mesh for the simulations. Previous published data report a mean diameter of (units in mm) 9.21 ± 1.79 (range: 6.45-12.00) for diseased carotid bulb and of 4.27 ± 0.91 (range: 2.89-6.35) for the diseased ICA [102]. On the other hand, commercial stents commonly used in carotid angioplasty have struts dimensions of the order of tens to hundreds of micrometers [45].

The assessment of a suitable mesh requires a mesh sensitivity analysis. It is worth to point out that a mesh sensitivity analysis involving local refinement is a problem with two degrees of freedom: one relates to the element size in the unrefined region - i.e., far away from the immersed body -, the other relates to the element size in the refined region - i.e., around the immersed body -. Therefore, the mesh sensitivity analysis consisted of two steps. First, we performed simulations with uniform meshes in order to assess and fix the element size in the unrefined region. Then, we introduced local refinement and performed simulations varying the element size in the refined region. The use of an idealized model allowed to easily build a body-fitted mesh to compare and highlight differences between immersed and body-fitted approaches.

5.7.2 The computational model

We performed transient simulations of the problem shown in figure 5.10, describing a parallelepiped (modelling a stent strut) immersed in a cylindrical pipe (modelling a carotid artery). The parallelepiped is $240 \mu\text{m}$ along the transversal direction, $150 \mu\text{m}$ along the longitudinal direction (direction of flow, i.e., *worst case scenario*) and has a length of 1 cm, protruding outside the fluid domain in the

5.7. Mesh sensitivity analysis in an idealized model of immersed stent strut

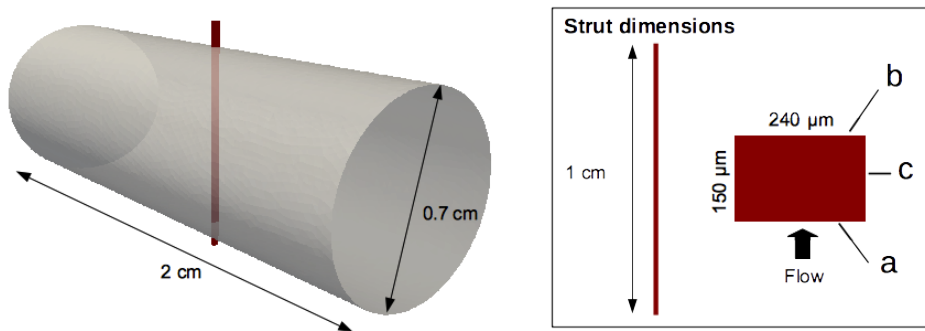


Figure 5.10: Computational model used for the mesh sensitivity analysis. On the left, idealized model of the stent strut immersed in a cylindrical pipe used in the mesh sensitivity analysis with body-fitted and immersed approaches. On the right, dimensions of the parallelepiped used to model the stent strut and axes a, b and c where WSS are plotted.

immersed case. The cylindrical pipe has a diameter of 0.7 cm and a length of 2 cm. The body-fitted model was created performing a boolean operation between the cylinder and the parallelepiped. On the other hand, the immersed model consisted of two separated and overlapping domains. As BCs, we prescribed at the inlet a constant parabolic velocity profile corresponding to the systolic peak from the flow waveform considered in [121], a zero pressure at the outlet and no-slip condition at the wall. In the body-fitted case, no-slip conditions were also applied at the surfaces of the parallelepiped. The fluid was considered newtonian with a density of 1.040 g cm^{-3} and a dynamic viscosity of 0.04 P. Transitory simulations were carried out over a period of 150 ms with a time-step of 1 ms. The duration of the time period was sufficient to damp any transitory effect and reach a steady-state solution. Fluid was considered at rest in its initial condition. Solver residual tolerances on mass and momentum were set to 10^{-5} . Ten Newton iterations per each time-step were allowed.

Table 5.1: Element edge lengths and number of degrees of freedom (#DOF) of the body-fitted and immersed models with uniform mesh.

Edge length [μm]	Body-fitted [#DOF]	Immersed [#DOF]
400	19798	19448
300	44865	44756
200	146302	146258
100	1131822	1145806

Table 5.2: Element edge lengths inside the refined region and number of degrees of freedom (#DOF) of the body-fitted and immersed models with local refinement.

Edge length [μm]	Body-fitted [#DOF]	Immersed [#DOF]
50	201663	191392
25	472629	418570
18.75	687250	576709
12.5	1164805	892674

5.7.3 Mesh sensitivity analysis

As previously pointed out, the goal of the first step is to identify the best element size in the unrefined region, i.e., in all the regions of the fluid domain where the flow field is scarcely influenced by the presence of the immersed body. With this aim, we performed simulations of body-fitted and immersed models using uniform linear tetrahedral meshes with different element edge lengths (table 5.1). The velocity magnitude along the longitudinal and transversal directions of these models are depicted in figures 5.11 a-d. For the sake of comparison, the reader should not consider in this step the errors among the solutions presenting from zero-coordinate onwards in the figures 5.11-a and 5.11-c because, at that region, the flow field is perturbed by the immersed body and would, therefore, require a refined grid. The analysis of the figures 5.11 a-d revealed a good approximation of the solutions in the body-fitted and immersed models with edge lengths of 300 μm , which was therefore used in the second step of the analysis introducing the local refinement (table 5.2). The velocity

5.7. Mesh sensitivity analysis in an idealized model of immersed stent strut

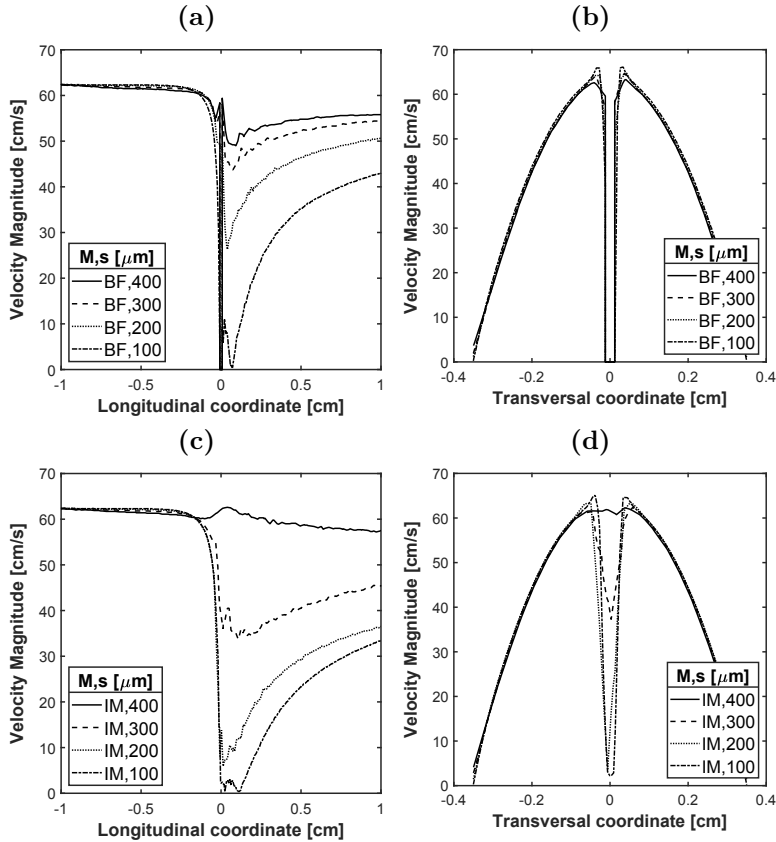


Figure 5.11: Comparison of the velocity magnitude along the longitudinal and transversal directions in the models with body-fitted and immersed uniform meshes at different element sizes. (a) Velocity magnitude along the longitudinal direction in the models with body-fitted uniform meshes; (b) Velocity magnitude along the transversal direction in the models with body-fitted uniform meshes; (c) Velocity magnitude along the longitudinal direction in the models with immersed uniform meshes ; and, (d) Velocity magnitude along the transversal direction in the models with immersed uniform meshes. M= Model, s = element size (characteristic edge length), BF = Body-fitted, IM = Immersed.

magnitude along the longitudinal and transversal directions of models with local refinement are depicted in the figures 5.12 a-d. Results showed that elements of $50\ \mu\text{m}$ in the refined region led to overall good approximation of the velocity field in body-fitted models, while element lengths of $25\ \mu\text{m}$ were required to obtain comparable accuracy in the immersed case. In fact, while in the body-fitted models the zero-velocity condition at the boundaries is automatically satisfied, in the immersed approach the velocity magnitude is in general non-null at these regions. As discussed in section 5.5, whether the method is able to “force” the velocity to (a value close to) zero at the boundaries and inside the immersed body depends on multiple factors including the value of the forcing term, the tolerances of the solver and the mesh size [112, 69]. As a measure of the accuracy of the velocity field obtained using the immersed approach, in table 5.3 are listed the minimum values of the velocity magnitude inside the stent strut of the immersed models expressed as percentage of the maximum velocity magnitude along each direction. Analogously, to evaluate the accuracy of the velocity field around the immersed object, in figure 5.4 are listed the maximum relative errors of the velocity magnitude around the stent strut of the immersed models with respect to the body-fitted solution. Results show that the proposed methodology allows to force the velocity magnitude *inside* the strut to values less than 1% of the maximum velocity along each direction in all the investigated cases, although the accuracy increases with finer meshes. On the other hand, less accuracy is encountered in the approximation of the solution *around* the immersed strut, especially in the longitudinal direction (range of errors in the transversal direction: 0.29% - 4.19%; range of errors in the longitudinal direction: 9.97% - 11.21%).

The inability of the immersed method to adequately describe the flow pattern around the immersed strut leads also to an inaccurate description of the WSS field at the interface between the stent strut and the blood flow. Figures 5.13 a-c depict the plot of the WSS magnitude along the axes a, b and c (figure 5.10) at the stent strut-blood inter-

5.7. Mesh sensitivity analysis in an idealized model of immersed stent strut

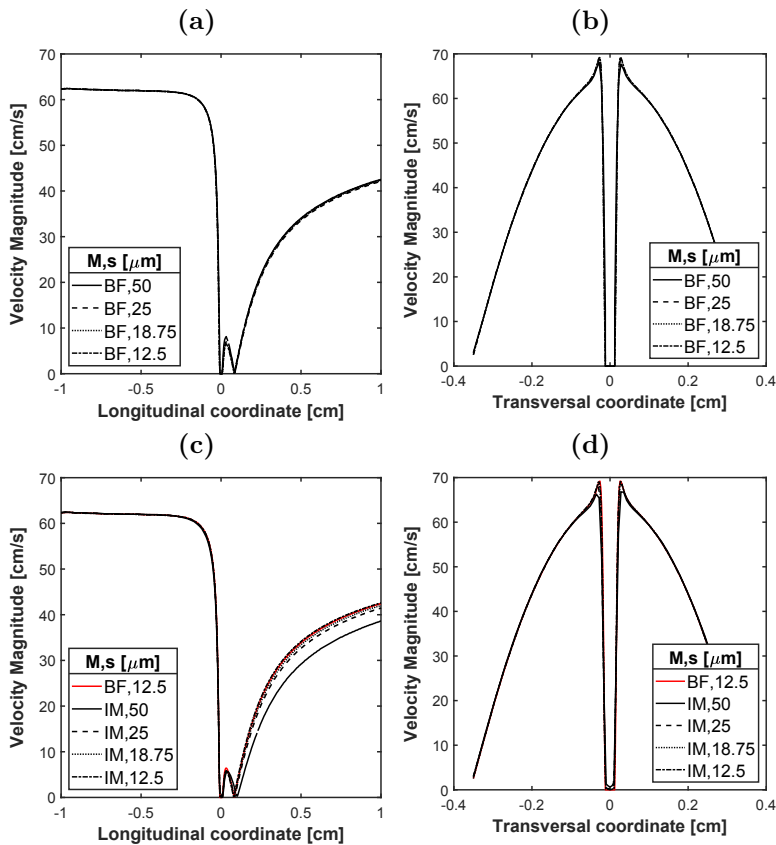


Figure 5.12: Comparison of the velocity magnitude along the longitudinal and transversal directions in the models with body-fitted and immersed meshes at different element sizes in the refined region. (a) Velocity magnitude along the longitudinal direction in the models with body-fitted locally refined meshes; (b) Velocity magnitude along the transversal direction in the models with body-fitted locally refined meshes; (c) Velocity magnitude along the longitudinal direction in the models with immersed locally refined meshes, compared to the velocity magnitude along the longitudinal direction in the model with the finest body-fitted locally refined mesh; and, (d) Velocity magnitude along the transversal direction in the models with immersed locally refined meshes, compared to the velocity magnitude along the longitudinal direction in the model with the finest body-fitted locally refined mesh. M= Model, s = element size (characteristic edge length), BF = Body-fitted, IM = Immersed.

Table 5.3: Minimum values of the velocity magnitude inside the stent strut of the immersed models expressed as percentage of maximum velocity magnitude along each direction.

Edge length [μm]	Longitudinal [%]	Transversal [%]
50	0.36	0.88
25	0.11	0.27
18.75	0.098	0.15
12.5	0.024	0.068

Table 5.4: Maximum relative errors of the velocity magnitude around the stent strut of the immersed models with respect to the body-fitted solution.

Edge length [μm]	Longitudinal [%]	Transversal [%]
50	-11.21	-4.19
25	-12.3	-1.3
18.75	-9.03	-0.72
12.5	-9.97	-0.29

face. Also, in figure 5.13-d the contour plots of the WSS magnitude in the body-fitted and immersed models are shown. These results show that the accuracy of the computed WSS is particularly affected by the immersed method, with no significant improvement associated with a decrease of the size of the mesh around the immersed strut. WSS are inaccurate at the corners of the strut, particularly those belonging to the transversal surface impacted by the flow (right and left sides of axis a, left side of axis c). On the other hand, a better accuracy is achieved in the opposite transversal surface (axis b).

5.7.4 Discussion

In this section we have performed a grid sensitivity analysis on a model of a stent strut immersed in a pipe to understand how to build a proper mesh to simulate carotid stenting using the “immersed solid method”. Previous studies have shown that the ability of the method to drive the velocity to zero at the nodes of the fluid mesh in-

5.7. Mesh sensitivity analysis in an idealized model of immersed stent strut

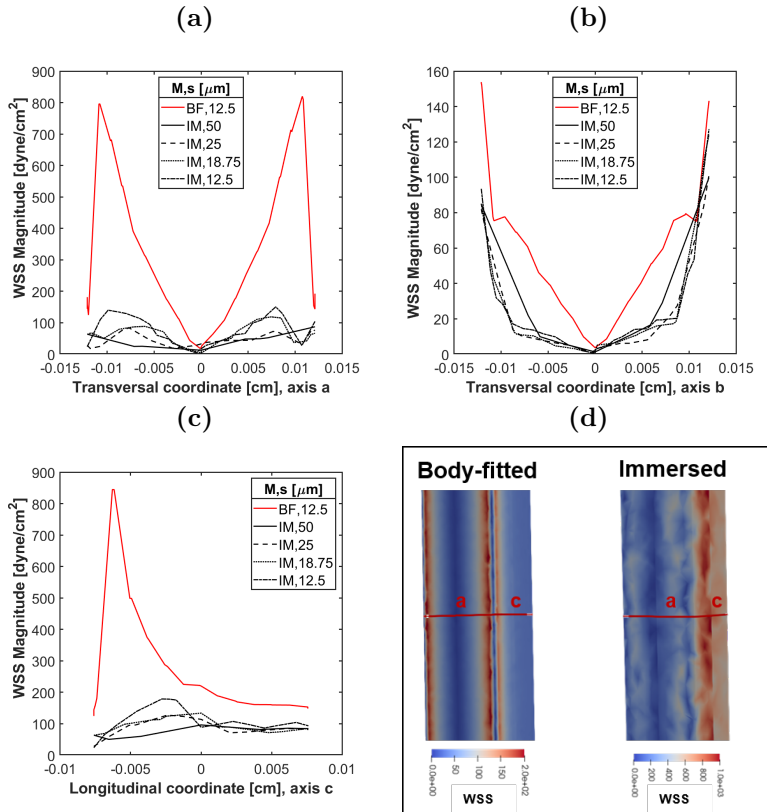


Figure 5.13: Comparison of the wall shear stress (WSS) magnitude at the stent strut-blood interface in the models with the body-fitted and immersed meshes at different element sizes in the refined region. (a) WSS magnitude along the transversal axis a (on the transversal strut surface impacted by the flow) in the models with body-fitted and immersed locally refined meshes; (b) WSS magnitude along the transversal axis b (on the transversal strut surface not impacted by the flow) in the models with body-fitted and immersed locally refined meshes; (c) WSS magnitude along the longitudinal axis c (on the lateral strut surface in the direction of the flow) in the models with body-fitted and immersed locally refined meshes; and, (d) Contour plots of the WSS magnitude at the strut surfaces in a body-fitted and immersed model.

cluded in the immersed object improves as the size of the elements in that region decreases to a fraction of the size of the immersed boundaries. In the case of very thin objects such as stents, the satisfaction of this requirement using uniform meshes easily leads to extremely large meshes, therefore a local mesh refinement strategy was adopted hereby. Our results showed that an edge length of $300\ \mu\text{m}$ for the elements outside, and of $25\ \mu\text{m}$ for the elements inside the refined region allowed to build a mesh showing grid independence of the solution and an error on the velocity magnitude less than 0.5% inside the strut, less than 2% around the strut along the transversal direction, but around 12% in the longitudinal direction. Unfortunately, a comparable accuracy was not achieved concerning the description of the WSS at the stent strut-blood interface, particularly at the corners of the strut surface impacted by the flow. Furthermore, the WSS description improved only by a small amount with refined meshes, indicating that other factors such as solution interpolation method and boundary layer model should be improved in order to tackle this aspect. Also, a sensitivity analysis of the scaling factor K of equations 5.3, 5.4 and 5.5 could suggest its optimal value to improve the accuracy of the solution near the solid body. As the description of the WSS at the stent strut-blood interface can be particularly relevant to study the impact of the endovascular device on the blood cells and the associated thrombogenic risk [72], this aspect is a current limitation of the proposed approach which has to be improved before translating the tool towards more clinical applications. On the other hand, the description of the WSS at the vascular wall, which is relevant for the evaluation of the impact of the endovascular device on the endothelial cells and the associated risk of in-stent restenosis, can be much more accurate because the computational grid conforms to the vascular wall and the no-slip boundary conditions are thereby strongly enforced.

Recalling that the strut has dimensions of $150\ \mu\text{m}$ in the longitudinal direction, and of $240\ \mu\text{m}$ in the transversal direction, the elements here adopted had length accounting for 15% of the boundary dimen-

5.7. Mesh sensitivity analysis in an idealized model of immersed stent strut

sion in the longitudinal direction, and 10% of the boundary dimension in the transversal direction. Although the Ansys CFX documentation suggests that the edge length of the fluid elements around the immersed object should be smaller than 10% of the dimension of its immersed boundaries, suggesting a possible cause of the higher error measured along the longitudinal direction, we still found an error of 10% in the longitudinal direction even with an element size of 12.5 μm . Therefore, we selected an element length of 25 μm for the subsequent simulations of carotid stenting.

Remarkably, even in a simple model like the one used in this study, the adoption of the proposed local mesh refinement has brought to large meshes. In fact, the strategy produces essentially three zones: the unrefined zone - where the mesh is coarse -, the refined zone - where the mesh is highly refined - and a transition zone in which the element size grows gradually in order to avoid abrupt element size change and excessive distortions. In our models, we kept the growth rate of the element size in the transition zone to an empirical value of 1.2 [122], which is recommended by the scientific community to avoid interpolation errors and inaccuracy of the solution due to bad quality mesh. However, as the difference between the sizes of the elements of the refined and unrefined regions increases, the transition region and, consequently, the number of elements inside grows. In our case, a single stent strut has led to appropriate mesh size of nearly 0.5 million degrees of freedom. A full stent model placed inside a realistic vessel would certainly lead to extremely large meshes.

In conclusion, we selected a mesh with the following characteristics:

- in the refined zone near the immersed device, the element edge length should be 10-15% of the smallest dimension of the strut;
- in the uniform zone far from the stent strut, the element edge length should be around 0.03 cm;
- in the transition zone between the refined and the uniform regions, the element edge length should grow with a growth rate of 1.2.

5.8 Time-step sensitivity analysis

5.8.1 Motivations

Using an idealized model of a stent strut immersed in a cylindrical pipe, in the previous section we have investigated how to build a suitable mesh for the simulation of the hemodynamics inside the stented carotid by “immersed solid method”. In other words, we have addressed the problem of the spatial discretization for our specific application. However, the flow dynamics in the carotid arteries is unsteady in time and, therefore, requires also a time discretization. Indeed, even with the strongest modelling assumptions, the flow at the CCA has to be modelled as a periodic waveform like the one depicted in figure 5.1. As the model becomes more complex, further time dependencies can be introduced. For example, the peripheral vascular system may be modelled using multiscale approaches [123] or, in case of fluid-structure interaction, the velocity field at the wall nodes may vary in time as the wall moves under the pressure exerted by the flow [124, 125, 126]. In a CFD simulation, the time step discretizes the temporal domain just like the elements of a mesh discretize the spatial domain. The analogy goes further and holds also for what concerns the size: the smaller the time step, the higher the temporal accuracy but also the computational cost. In general, the time step size depends on several factors dealing with the physics of the specific problem, the outcome of interest and the specific numerical method. More specifically, the time step should adequately capture the dynamics of the flow, i.e., the temporal changes of the velocity and pressure fields, particularly preponderant in turbulent flows (also known as fluctuations). On the other hand, the time step can be certainly relaxed if the variable of interest of the simulation is the result of an integration over space (e.g., the flow rate at the ICA), or time (e.g., the TAWSS at the bifurcation). Finally, the time step depends on few numerical characteristics of the problem, including the nature of the solver (i.e., implicit/explicit), the parameters of

5.8. Time-step sensitivity analysis

the integration scheme (i.e., the number of iteration of the iterative solver, the tolerances) and the size of the elements of the mesh. For explicit solvers, the previous concepts have been combined together into the Courant-Friedrichs-Lewy (CFL) convergence condition [127] that, in one dimension, takes the following form:

$$C = \frac{u\Delta t}{\Delta x} \leq 1 \quad (5.8)$$

where the dimensionless parameter C is called the Courant number, u is the magnitude of the flow velocity, Δt is the time step size and Δx is the element mesh size. The heuristic interpretation of the CFL condition is that the duration Δt of the time step in which computing the amplitude of a certain waveform travelling at velocity u across a computational grid of elements Δx should be less than the time for the wave to travel between two adjacent points of the grid. On the other hand, implicit solvers (like the one used in this study) are “unconditionally stable” and do not have to strictly withstand with the CFL condition. However, the Courant number is still used by the software to manage the time step initialization procedure and will therefore considered in this study [112].

Besides time step size, another temporal aspect to consider when setting a CFD simulation of carotid stenting is the number of cycles to simulate. In fact, unless more complex initial conditions are employed, the fluid at the first instant of the simulation is assumed to be still, i.e., the velocity field is null everywhere and no pressure gradients are present. As the simulation starts, the BCs force the flow to move, provoking an initial transitory and unrealistic phase during which the flow is accelerated that must not be included in the analysis. It is common practice to simulate more than one cardiac cycle in order to get rid of the first from the solution [128]. Also, in the regions of the vascular system characterized by transitional to turbulent flow, it is advisable to simulate a larger number of cardiac cycles to extract time-averaged hemodynamics indices [129].

For what has been said, the assessment of such temporal aspects (i.e.,

time step size and number of cycles) should be performed directly on a realistic problem of carotid stenting to incorporate the characteristics of the mesh used and the flow dynamics originating from both the complex geometry and the presence of the stent.

Therefore, we set up a patient-specific model of carotid bifurcation in which a XACT stent (Abbott Vascular, Abbott Park, IL, USA) was virtually deployed in the ICA and performed simulations of four cardiac cycles with four decreasing time step sizes. We compared the flow rate at the ECA, the instantaneous velocity magnitude at one probed point near the protruded stent in the bifurcation (point A), and the WSS at a different probed point at the bifurcation wall (point B) in order to assess the correct values of such simulation parameters.

5.8.2 Computational model

Carotid model generation

In the present study, we performed simulations on the patient specific model of the carotid bifurcation shown in figure 5.14. The patient-specific reconstructed vessel has been previously used to perform CFD simulations of the carotid hemodynamics before and after stenting using a penalty approach embedded in an in-house code [31]. Briefly, the luminal surface was derived from image analysis of the post-operative computed tomography (CT) scan of a 55-years-old asymptomatic female with stenosis (80% NASCET method) in the ICA. The segmentation was performed via the open-source software ITK snap [130] through active contour method and then exported as STL format. Before generating the mesh, cylindrical extensions were added to the inlets and outlets of the extracted surface through VMTK [59] to ensure that the solution in the vascular domain was not forced by the presence of the BCs.

Mesh generation with local refinement

The fluid domain was discretized with linear tetrahedral elements exploiting the proposed meshing tool presented in section 5.6. To perform the mesh refinement around the endovascular device, a computer-aided designed (CAD) model of a XACT stent was virtually placed by rigid rototranslations in the ICA according to the straightening of the vessel detected in the post-operative configuration. Two different levels of mesh refinement were defined:

- inside and around the immersed stent, where the elements had edge length of $25\ \mu\text{m}$ as found in section 5.7;
- a boundary layer at the bifurcation, where the elements had edge length of $100\ \mu\text{m}$. This region was defined as the part of the model comprised between three planes (α , β and γ) whose position was chosen to include the whole stent in the ICA and part of the CCA and ECA where the flow might be affected by the presence of the endovascular device.

In both cases, the refined regions had a thickness equal to three times the size of the elements inside. Finally, according to the results of section 5.7, we selected an edge length of $300\ \mu\text{m}$ for the elements outside these refined regions and growth rate inside the transition zones of 1.2 [122]. A longitudinal viewcut of the bifurcation showing the details of the local mesh refinement and the position of the planes used to determine the boundary layer are depicted in figure 5.14-a and 5.14-b.

CFD simulation set-up

The following BCs were prescribed according to [66] (figure 5.14):

- At the CCA, a time-dependent fully-developed parabolic velocity profile obtained from the flow rate waveform from Marshall et al. [121];

- at the ICA, an outflow corresponding to 60% of the flow at the CCA;
- at the ECA, a null static pressure;
- at the luminal walls, a no-slip condition;

As initial condition, the fluid was considered at rest. Concerning the solver set-up, convergence criteria consisted of mass and momentum root mean square residuals less than 10^{-4} [131, 122] and up to ten iterations per each time-step were allowed. Also, the flow was considered laminar and no turbulence model was adopted. The immersed solid was treated by setting a momentum source scaling factor equal to 10, a “modified forcing” method as boundary model and a “search through elements” as boundary tracking (chapter 1.2.10 of [112]). The blood was modelled as an incompressible newtonian fluid with a density of 1 g cm^{-3} and a dynamic viscosity of 0.04 P [31]. Four simulations with decreasing time step sizes were performed ($ts=0.01 \text{ s}$, $ts=0.005 \text{ s}$, $ts=0.002 \text{ s}$ and $ts=0.001 \text{ s}$) over a total simulation time of 4 s consisting of four cardiac cycles (namely, C0, C1, C2 and C3), and data were stored every 2, 4, 10 and 20 time-steps, respectively.

5.8.3 Time-step sensitivity analysis

The second column of table 5.5 lists the maximum Courant number among the mesh elements of the domain at the systolic peak of the performed simulations. Results show that the maximum Courant number ranged approximately from 20 to 192. Also, they show that the reduction factor between two consecutive Courant numbers does no match that found for the time steps above 0.002 s . Recalling the equation 5.8, this result evidences that in this case, the product between the maximum velocity u at the systolic peak and the element in which it occurs (giving the term Δx in the equation) is not constant, i.e. the computed velocity field has not converged. The third column of table 5.5 shows also that the solution of the non-linear system at

5.8. Time-step sensitivity analysis

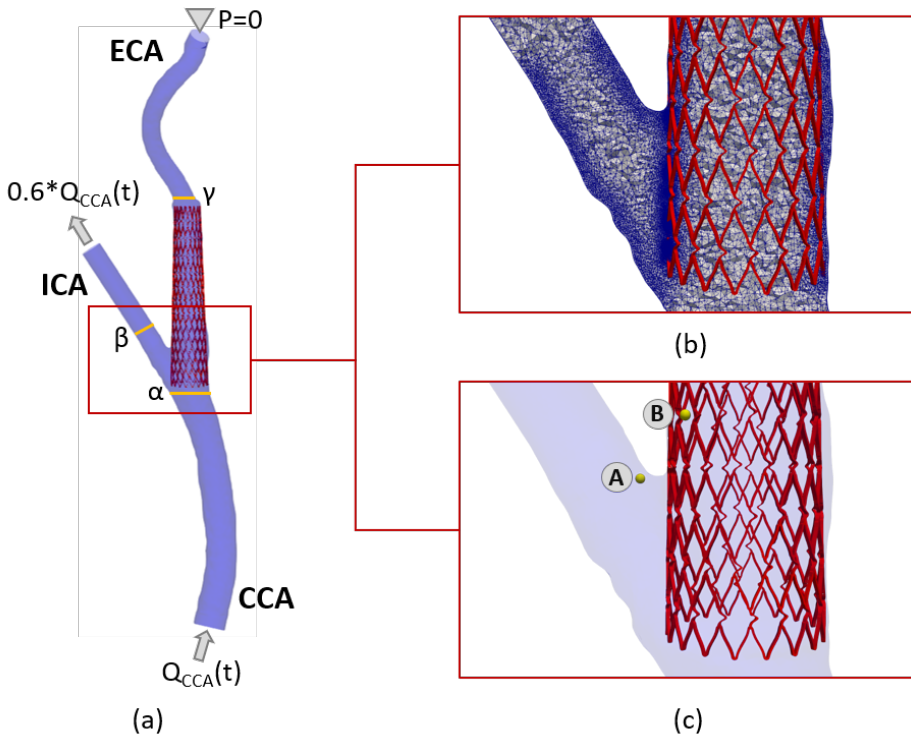


Figure 5.14: Patient-specific model used for the time-step sensitivity analysis. a) BCs and planes α , β , and γ for the boundary layer region; b) particular of the bifurcation evidencing the mesh refinement at the boundary layer and near the stent struts; (c) particular of the bifurcation showing the probe points A and B for the plot of the velocity and WSS vectors.

Table 5.5: Courant numbers and solver iterations at the systolic peak in the models with different time step sizes.

Time step [s]	Courant number	Iterations Number
0.01	192.51	3
0.005	99.42	2
0.002	40.59	1
0.001	20.34	1

the systolic peak was always reached within one to three loop iterations. Figure 5.15-b depicts the velocity streamlines at the systolic peak in the simulated model of the stented carotid artery. Also, a zoom on the local mesh refinement around the struts immersed in the blood domain at the level of the bifurcation is given in figure 5.15-a. It is possible to appreciate the effectiveness of the proposed approach to capture the blood flow disturbances induced by the stent struts protruding into the carotid bifurcation. Figure 5.16 shows the plots of the flow rates at the ECA and of the velocity magnitudes at the probed point A during the last simulated cardiac cycle at different time steps. While the computed flow rates at the ECA are overall similar with different time step sizes (figure 5.16-a), the local velocity magnitudes at the probed point A show temporal convergence below a time step of 0.002 s (figure 5.16-b). Moreover, no local fluctuations were detected in the plot of the velocity magnitudes during the cardiac cycle at all the investigated time step sizes (figure 5.16-b). Figures 5.17-a and 5.17-b show the components and magnitude of the WSS vector at the probed point B during the last cardiac cycle. As for the velocity, the WSS vectors is not adequately resolved in time in the simulations with time steps of 0.01 s and 0.005 s, showing a temporal convergence with time step sizes below 0.002 s. To assess the number of cardiac cycles to simulate needed to exclude the initial transitory effects and reach a periodic solution, we plot in figure 5.18 the velocity magnitudes at the probed point A over the four cardiac cycles at different time steps. Results show that the initial transitory effects vanish by the end of the first systolic peak (i.e., within the first

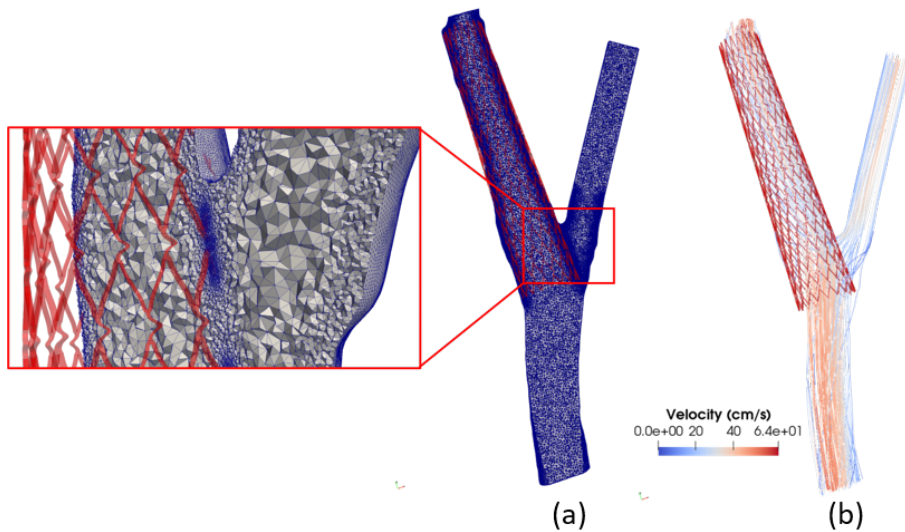


Figure 5.15: Local mesh refinement and blood flow pattern around the stent struts protruding inside the carotid bifurcation. a) The proposed meshing algorithm allows to easily obtain refined meshes near the immersed stent and vascular walls to achieve a good local accuracy of the solution; b) the immersed solid approach is used to compute the velocity field in the computational domain, showing effectiveness to capture the flow disturbances induced by the thin stent struts.

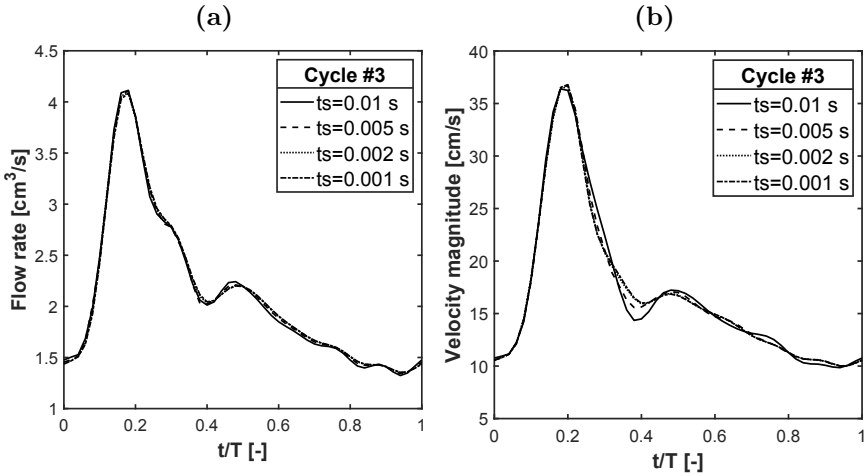


Figure 5.16: (a) Flowrate at the ECA and (b) velocity magnitude at the probed point A recorded at the last cycle of the simulations with different time steps. T_s = time step.

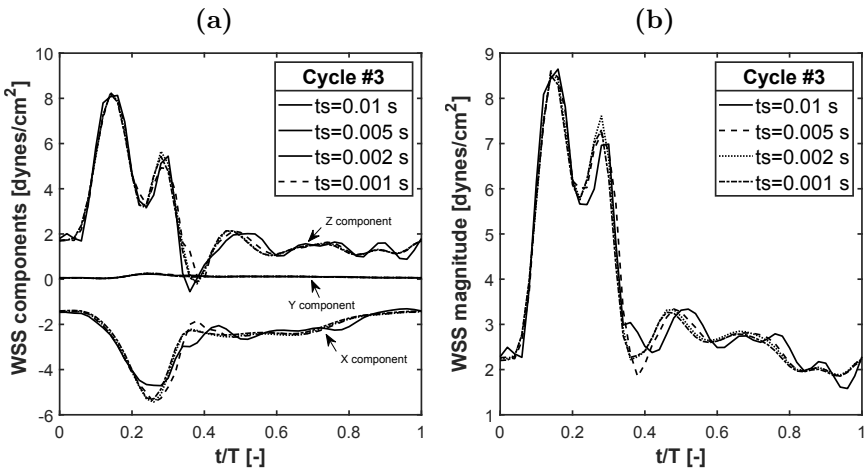


Figure 5.17: (a) Vectorial components and (b) magnitude of the WSS vectors at the probed point B recorded at the last cycle of the simulations with different time steps. T_s = time step.

5.8. Time-step sensitivity analysis

0.4 s of simulation time) in all the investigated cases, meaning that the second cycle is already sufficient to describe the flow occurring in the stented carotid over a whole cardiac pace.

Finally, we evaluate if the imposed flow division is verified. Figure 5.19-a depicts the computed flows at the CCA, ICA and ECA in the second cycle of the model with time step size of 0.002 s. Figure 5.19-b depicts the division of the flows with respect to the one imposed at the CCA. The figures show that the imposed boundary conditions are verified, although small numerical errors can be detected with respect to the difference between the imposed flow at the CCA and the sum of the flows at the outlets (ECA and ICA) at systolic peak.

5.8.4 Discussion

In this study, we have performed a sensitivity analysis to assess the time step size and the number of cycles to use in the simulations of carotid artery stenting with “immersed solid method” in Ansys CFX. Our results have shown that the choice of the time step size depends on the outcome of interest. In fact, if to adequately time resolve the flow rate at the ECA (figure 5.16a) a time step size of 0.01 s would be sufficient, the temporal resolution of local values of the velocity and the WSS vectors requires time steps below 0.002 s (figures 5.16b and 5.17). This is explained by the different mathematical operation behind such values. Indeed, starting from the velocity field directly coming from the numerical solution of the NSE, while the flow rate is computed by integrating it over the element face areas of the cross-section, the WSS field is computed by differentiating it among the surrounding nodes. As a result, any local differences in the velocity field, especially found in the simulations with time steps greater than 0.002 s, are smoothed by the integration and amplified by the differentiation. Our results showed that the local velocity at the probed point A converged within an error less than 1% starting from a time step of 0.002 s, that was therefore selected as the optimal time step size. The resulting maximum Courant number at the systolic peak

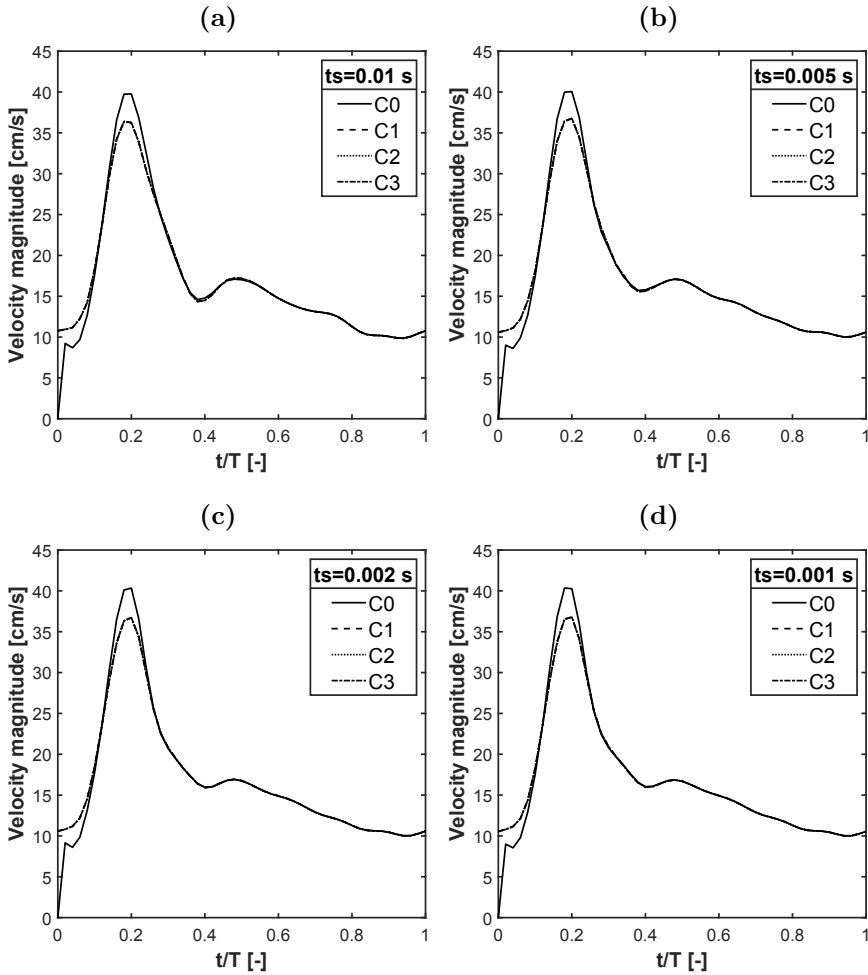


Figure 5.18: Velocity magnitudes at the probed point A over the four simulated cardiac cycles with different time steps. C = cycle, ts = time step.

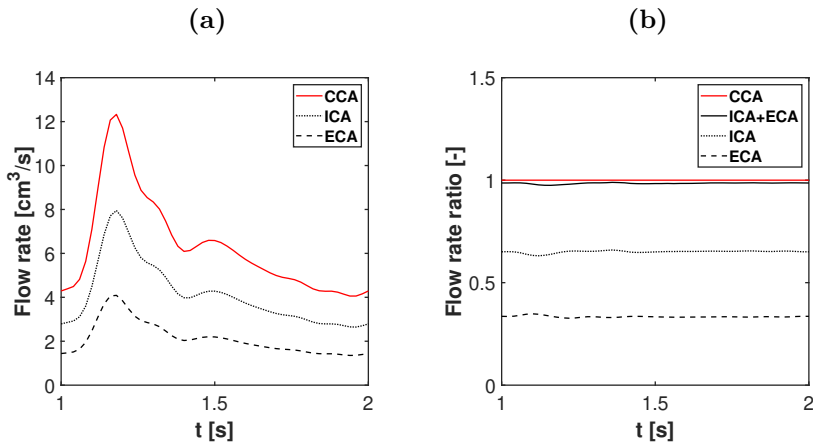


Figure 5.19: (a) Computed flowrate at the CCA, ICA and ECA, and (b) verification of flow division and mass conservation. In the right figure, the flow rates in the CCA, ICA and ECA normalized with respect to the flow rate in the CCA are depicted. Data were recorded in the second cycle of the model with time step equal to 0.002 s.

was around 40 and the non-linear system at this time-step was resolved at the given tolerance in the first iteration. This result confirms that the chosen time-step is small enough to guarantee the convergence of the solution, but also encourages to choose smaller residual tolerances if needed, as long as number of loop iterations stays below five as suggested in the chapter 15.4.2.7 of Ansys CFX-solver theory documentation [69]. On the other hand, the gained accuracy that would originate from the improvement the converge criteria might be negligible with respect to other numerical (e.g., excluded high-order terms, poor grid quality) and modelling (e.g., BCs, and blood constitutive model) sources of errors. Future studies should perform an uncertainty analysis to assess the most important sources of errors in the model and thus improve its usability. Another important aspect investigated in this section is the number of cardiac cycles to simulate in order to exclude from the solution the transitory effects due to the applied initial conditions. Concerning this point, there is a large vari-

ability among different studies with similar applications because the convergence to a periodic solution is strongly affected by the characteristics of the model like the presence of compliant elements or the flow complexity. While many authors perform simulations over more than three cardiac cycles (see, as an example, [54, 132, 53]), we found that the periodic solution was already available in the second simulated cycle, probably due to instantaneous BCs and the non-turbulent nature of the flow. In this regard, we found that the struts of the stent protruding in the CCA lumen induced slight local changes of the flow direction but no flow instabilities, as evidenced by the absence of velocity fluctuation in the probed point A downstream one of these struts. Indeed, the maximum Reynolds number describing the blood flow around the strut at the systolic peak is around 40; at this regime, it has been shown via optical coherence tomography and CFD that the flow past the immersed strut keeps its laminarity and eventual flow instabilities disappear so fast that a true turbulent flow does not develop [133]. In conclusion, to simulate the carotid stenting by immersed approach the following temporal parameters should be used:

- A time step smaller than 0.002s (larger time steps are allowed if the outcome of interest is derived from the integration of the velocity field);
- At least two simulated cardiac cycles, so that the first one is discarded to eliminate initial transitory effects.

5.9 Final comments and future developments

In this chapter, we have developed a framework for the CFD analysis of the post-stenting carotid artery using an immersed approach for the inclusion of the endovascular device in the blood domain. Usually, the immersed technique is naturally applied in the field

of fluid-structure interaction simulations, where the fluid exchanges forces with a solid body, causing a displacement of its boundaries. As the solid body boundaries move, a conforming body-fitted grid should in fact deform accordingly, leading to excessive mesh distortions with subsequent degradation of the mesh quality. The immersed technique allows to by-pass these difficulties, because the immersed body boundaries can “move” within the fluid mesh that remains fixed during the simulation (unless run-time remesh is performed). This approach has been extensively used in the field of cardiac simulations [134], where the deformations of the involved tissues (the heart muscle and valves) are significant.

Our target problem, i.e., the hemodynamic simulation of the post-CAS carotid artery with an immersed stent, does not contain such complexities: both the vessel wall and the stent are considered rigid and fixed bodies during the CFD simulation (indeed, the use of a body-fitted mesh around the stent is still potentially possible in this application [105, 54, 53]). However, the problem is characterized by a geometric complexity concerning the immersed body and this explains our choice to adopt a hybrid body-fitted/immersed approach: the fluid mesh is “body-fitted” with respect to the carotid walls (where we apply the strong no-slip BCs) while is “immersed” with respect to the endovascular device (where we apply the weak no-slip BCs). As mentioned in section 5.3, the reduced thickness of the stent struts implies that the generation of a body-fitted grid is error-prone and time-consuming due to the necessity of manually repairing small defects/gaps [30]. Combined with the high computational times necessary for this type of simulations, these difficulties compromise the use of CFD simulation of CAS in the clinical settings.

Our approach significantly facilitates the set-up of the CFD simulation including the endovascular device in the fluid domain, although the generation of the fluid mesh still presents some complexities related to the mesh refinement around the stent. However, the semi-automatic meshing tool proposed in section 5.6 considerably simplifies the procedure. Furthermore, building a refined mesh near the

stent is a crucial condition to accurately solve the velocity field, but it can be by-passed if the goal is to perform a quick simulation of the fluid dynamics in the stented carotid artery. This means that this framework can be extremely advantageous to study different post-CAS configurations (e.g. different stent lengths, placements, designs), by simulating different stents while keeping fixed the fluid mesh, then extract rough considerations of the resulting hemodynamics, and finally repeat the simulations with a sufficiently refined mesh to draw the accurate solution only on a selected subset of configurations.

The proposed meshing tool can be further improved, in particular concerning the characterization of the boundary layer. Indeed, the boundary layer is composed of tetrahedral elements, which is a less efficient choice comparing to structured or hybrid approaches such as prismatic/tetrahedral meshes [119, 59, 120]. The use of prismatic elements in the regions close to the vessel walls may be included in future developments of the tool, considering however the compatibility of a hybrid grid with the adopted solver for the CFD simulation. Another aspect that should be considered concerns the thickness of the boundary layer, which should be dependent on the local vessel size, consistently with the fact that the size of the physical shear layer is expected to scale with the vessel calibre. A possible solution could be the implementation of spherical size fields at the wall points where each radius depends on the local vessel calibre.

The framework can be further improved also with respect to the solver used to perform the CFD analysis. In this thesis, we have presented the results obtained by adopting the “immersed solid method” implemented within the software Ansys CFX. Commercial softwares provide stable, reliable and fast CFD codes, but their usage require the ownership of a valid licence. Furthermore, they do not possess the versatility that can be instead offered by open-source or in-house codes, dramatically limiting the possible applications that can be studied. During the three years of the PhD, we also tested and improved an in-house code for the CFD simulations with penalty approach, which was developed in a past collaboration between our

5.9. Final comments and future developments

group and Los Alamos National Laboratories, New Mexico, U.S. [31]. Because this line of research was not completed by the end of the PhD course, we decided to not include the relative results in this dissertation, but we encourage future research focusing on this aspect.

Chapter 6

Evaluation of post-stenting carotid hemodynamics with different stent designs: proof-of-concept study

6.1 Introduction

In this section, the methods proposed in chapter 5 are applied in a realistic problem. In particular, we aim to evaluate the differences of the hemodynamics in a post-stented patient-specific carotid artery resulting from the implant of four different commercial stents. Of note, the focus of this chapter is a methodological proof-of-concept: its ultimate goal is to show the reader a possible working pipeline exploiting the developed methods for the simulation and analysis of the post-carotid artery stenting (CAS) hemodynamics, rather than provide new clinical insights. Therefore, we here present a study that is, on one side, complete in terms of steps of the pipeline (i.e., the computational fluid dynamic (CFD) analysis through the immersed solid method, the extraction of the results and an example of post-

processing to find a potential clinical link) but, on the other side, uses simplified model assumptions that are clearly insufficient to draw any clinical conclusion. As a matter of fact, the applied boundary conditions (BCs) (imposed flow split and null static pressure at the outlet of the external carotid artery (ECA), as done in the carotid model of the time-step sensitivity analysis of section 5.8) are very simple to implement but, at the same time, rather strong and inevitably influence the results of the analysis. Another example concerns the description of the computed flow in the post-processing phase: to not burden the discussion, only the time-averaged wall shear stress (TAWSS) are considered, but it is clear that many other hemodynamic indices could be taken into account to better describe the blood flow and capture specific flow characteristics, especially if a relation to the pathology is sought.

Given such premises, the starting point to create the geometry of the post-stenting carotid artery for the CFD analysis consists of the STL surfaces of the virtually deployed stent and lumen of the treated carotid. In section 5.6 we have discussed the possible ways to bring such input data, alongside with their pros and cons. Briefly, if the stenting operation has already been performed, it is possible to acquire the geometry of the post-stenting carotid from medical images and then virtually implant the stent with different techniques such as by mapping its geometry on the vessel wall [105], overlapping its free configuration in the vessel of interest [31], or performing a structural simulation of stent deployment modelling the vascular walls as rigid material. If, on the other hand, the stenting operation has not yet been performed and the intention is to *predict* the post-CAS configuration, it is necessary to carry out a structural simulation of stent deployment within the pre-CAS geometry of the carotid and modelling its deformation under the forces of the expanded stent. Whatever is the pursued road, the proposed methodology can always be applied as long as the geometries of the post-CAS stent and carotid lumen are available. For instance, in the time-step sensitivity analysis of section 5.8, the post-stenting carotid geometry was constructed from

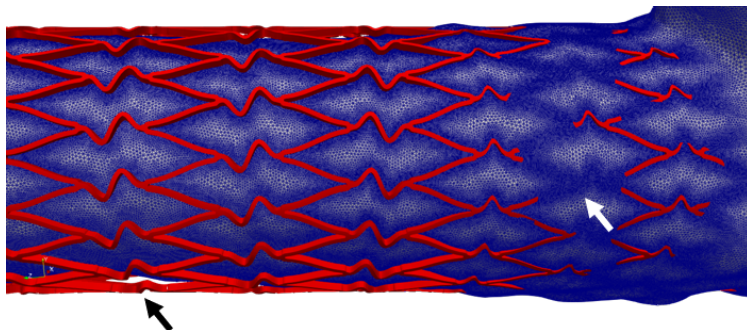


Figure 6.1: Generation of non-conforming grid when the endovascular device is not perfectly positioned inside the vessel lumen. A XACT stent in its free configuration was virtually deployed inside the post-stenting carotid lumen by rigid rototranslation. As a consequence, the endovascular device did not perfectly adhere to the luminal surface, resulting in regions where the struts were completely outside the fluid volume (black arrow) and regions where the struts were completely immersed (white arrow). The proposed framework allowed to easily set up the computational grid and perform the CFD simulation.

post-operative computed tomography (CT) images, then a computer-aided designed (CAD) model of a XACT stent was virtually placed by rigid rototranslations in the ICA according to the straightening of the vessel detected in the post-operative configuration. In that case, the adoption of the immersed approach allowed a fast generation of a proper computational grid bypassing the need of performing boolean operations to build a body-conforming mesh, a potential source of error since the endovascular device was not perfectly positioned inside the vessel lumen (figure 6.1). In this chapter, instead, we show how to perform the CFD analysis with the proposed immersed approach after a structural simulation of virtual stent deployment. In particular, we derive the STL surfaces of the four implanted stents and of the lumen of the patient-specific carotid artery from a previous finite element (FE) study by our group, which aimed to compare different stent designs with respect to the resulting stent cell areas [135]. In turn, that study exploited a previously developed procedure for the stent deployment simulation [136]. Of note, in that stud-

ies, the FE analysis simulated the stent deployment inside a silicon model of a patient-specific carotid artery, in order to experimentally validate the FE stent deployment procedure towards experimental results. The resulting post-CAS geometric models used in this chapter do not, therefore, represent the realistic geometry of a stented carotid artery, as the vascular wall material was silicon and not vascular tissue. Given the aim of this chapter, we will focus only on the methods dealing with the flow analysis; the reader interested in the details of the methods relating to the FE simulations of CAS is referred to the relevant papers instead [135, 136].

6.2 Carotid geometry

The patient-specific carotid model considered in this study reflects the geometry of a silicon mock artery, derived from a CT angiogram of the carotid bifurcation of a 83-year-old man presenting with a mild 24% stenosis (NASCET method) in the most proximal internal carotid artery (ICA) segment. Details of image acquisition are: Somatom Sensation Dual Energy scanner (Siemens Medical Solutions, Forchheim, Germany, 1 mm slice thickness, 512 by 512 matrix, 0.3 mm scan interval. Image segmentation was performed in Mimics (version 13; Materialise, Leuven, Belgium) and the reconstructed STL surface of the artery lumen was cropped to a 42 mm long segment. From now on, the STL representation of this surface will be labelled as CONTROL because it represents the unstented stenosed carotid geometry.

6.3 Stent geometries

The CONTROL surface was exported to a FE solver for the simulations of virtual deployment of four different stents (see [136, 135] for the details of the simulations). Four commercially available stents used in the clinical practice were considered: ACCULINK (Abbott,

6.4. Mesh generation with local refinement

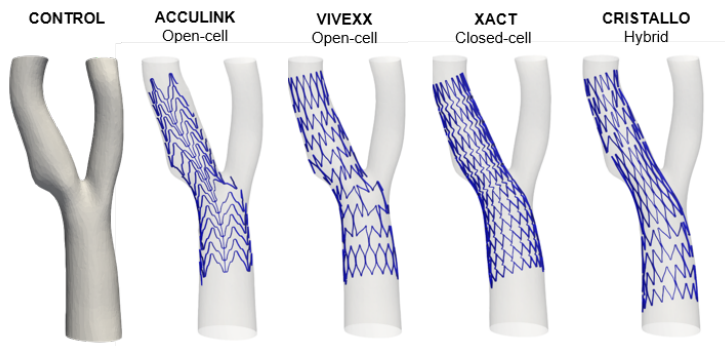


Figure 6.2: Stents deployed in the carotid artery. From left to right, CONTROL model (unstented), then stents ACCULINK, VIVEXX, XACT and CRISTALLO. All stents have 9 mm reference diameter and 30 mm length.

Illinois, USA), VIVEXX (C. R. Bard Angiomed GmbH and Co., Germany), XACT (Abbott, Illinois, USA) and CRISTALLO (Invatec/Medtronic, Roncadelle (BS), Italy). As starting point, the straight configuration with 9 mm reference diameter and 30 mm length was considered for all models. Figure 6.2 shows the CONTROL as well as the four stented models investigated in this study.

6.4 Mesh generation with local refinement

The STL representations of each stent and of the luminal surface of the carotid were extracted from the deformed configuration resulting from the FE stent deployment simulations performed in [135, 136]. These triangulated surfaces were used to generate the computational models for the CFD simulation with immersed approach as described in section 5.6. First, cylindrical extensions of length equal to eight times the diameters of the parent vessels were added to the common carotid artery (CCA), ECA and ICA of each extracted surface through the Vascular Modelling Toolkit (VMTK) [59] to ensure that

the solution in the vascular domain was not forced by the presence of the BCs. The resulting fluid domain was then discretized with linear tetrahedral elements exploiting the proposed meshing tool presented in section 5.6. Two different levels of mesh refinement were defined:

- element edge length of $100\ \mu\text{m}$ in a boundary layer in a region comprised between two horizontal planes whose position was chosen to include the whole stent in the ICA.
- around the surface of a portion of the immersed stents protruding inside the carotid bifurcation, where the elements had edge length of $25\ \mu\text{m}$ according to the results of section 5.7. This portion was defined as the part of the stent comprised between two horizontal planes (one at $z=1.5$, the other at $z=2.5$) whose position was chosen to include the stent protruding in the bifurcation and the carotid sinus.

For the control model, only the mesh refinement for the boundary layer was performed. Opposite to what done for the time step sensitivity analysis, the thickness of the refined region was set such that only one element of 25 micrometers was allowed to stay in order to prevent the meshes to be too large. The reason why such issue did not present for the stented model in the time-step sensitivity analysis is because in that case the stent was partially outside the computational fluid domain due to the rigid rotation for its inclusion. Therefore, all the portions outside the fluid domain did not contribute to the mesh refinement, diminishing the number of elements generated. In this case, the stent is constrained inside the vessel surfaces because of the contact algorithm acting during the stent deployment FE simulation. Then, a transition zone to allow the elements to grow with a rate of 1.2 until an edge length of $300\ \mu\text{m}$ was prescribed. The mesh sizes of the computational models are listed in table 6.1.

6.5. CFD simulation set-up

Table 6.1: Mesh characteristics of the computational models used for the CFD analysis.

Model	N. of Elements	N. of Nodes
CONTROL	2,013,519	390,131
ACCULINK	9,993,093	1,723,207
VIVEXX	8,568,131	1,497,866
XACT	11,088,061	1,917,063
CRISTALLO	9,789,831	1,698,353

6.5 CFD simulation set-up

The following BCs were prescribed according to [66]:

- At the CCA, a time-dependent fully-developed parabolic velocity profile obtained from the flow rate waveform of figure 5.1;
- at the ICA, an outflow corresponding to 60% of the flow at the CCA;
- at the ECA, a null static pressure;
- at the luminal walls, a no-slip condition;

As initial condition, the fluid was considered at rest. Concerning the solver set-up, convergence criteria consisted of mass and momentum root mean square residuals less than 10^{-4} [131, 122] and up to ten iterations per each time-step were allowed. Also, the flow was considered laminar and no turbulence model was adopted. The immersed solid was treated by setting a momentum source scaling factor equal to 10, a “modified forcing” method as boundary model and a “search through elements” as boundary tracking (chapter 1.2.10 of [112]). The blood was modelled as an incompressible newtonian fluid with a density of 1 g cm^{-3} and a dynamic viscosity of 0.04 P [31]. Time step sizes of 0.002 s over a total simulation time of 2 s consisting of two cardiac cycles were simulated according to section 5.8 and data were stored every twenty time-steps during the second cardiac cycle.

6.6 Post-processing of the simulation results

Velocity, pressure and wall shear stress (WSS) fields were saved to text files using the Ensign format and then imported into the software Paraview for further post-processing. Bulk flow visualization, vascular resistances and TAWSS distribution were computed to compare the impact of different stent designs on the carotid hemodynamics.

Flow was visualized around the stent struts of the portion of the stent protruding inside the carotid bifurcation as described in 6.4. To do so, the output models containing the velocity vectorial fields were clipped by two horizontal planes (one at $z=1.5$, the other at $z=2.5$) and the streamlines were computed in Paraview using the streamtracer component, setting the resolution to 1000 to ease the visualization.

The impact of the stent design on the ICA (ECA) flow resistances was evaluated. First, we took the area-averaged pressures (namely, P_{CCA} , P_{ICA} , and P_{ECA}) on the cross-sections of the CCA and ICA (ECA) defining the boundaries of the original model without the flow extension; second, we computed the pressure delta $\Delta_{CCA-ICA} = P_{CCA} - P_{ICA}$ ($\Delta_{CCA-ECA} = P_{CCA} - P_{ECA}$); third, we divided the pressure delta by the flow inside the respective vessel to obtain its vascular resistance $R_{CCA-ICA} = \Delta_{CCA-ICA}/Q_{ICA}$ ($R_{CCA-ECA} = \Delta_{CCA-ECA}/Q_{ECA}$).

Finally, we assessed the impact of stent design on TAWSS pattern. TAWSS in the carotid bifurcation were considered low and atherogenic if $< 4 \text{ dyne/cm}^2$, high if $> 70 \text{ dyne/cm}^2$ according to [72]. To compare the TAWSS distribution among the investigated cases, we first removed the areas of the carotid “in contact” with the apposed stent. In this sense, we report the *intra-strut* TAWSS area, disregarding the *under-strut* TAWSS area in the calculation. To do so, we exploited the built-in VMTK function `vmtksurfacedistance` to map on the carotid wall the distance field between the luminal surface and the immersed stent. Then, by using the threshold component in Par-

aview, we filtered out the areas of the vessel wall where the distance was less than a fifth of the stent strut thickness to exclude the regions where the stent was correctly apposed [53]. The vascular walls of each model deprived with the regions in contact with the stent were used to extract the percentage areas exposed to low, medium and high TAWSS. Because the percentage area exposed to a certain range of TAWSS depends on the total area used for the computation, we clipped each stented model to isolate only the stented portion of the vessel. Accordingly, the percentage areas exposed to low, medium and high TAWSS in the control model were computed differently for each stented model by taking the portion of the control vessel correspondent to the stented counterpart.

6.7 Impact of stenting on the blood flow field

Figure 6.3 shows the streamlines in the carotid bifurcation of the considered models at systolic peak. In the unstented carotid, blood flow appears mainly laminar, with two recirculation zones at the outer walls of the ICA (inside the carotid sinus) and ECA. In the stented models, the laminarity is preserved in the distal CCA, ECA and ICA, but flow disturbances are detected around the stent struts protruding into the bifurcations. The stent nets constitute a physical barrier at the ECA ostia altering the blood flow around the struts, an effect that is more evident in open-cell designs (i.e., ACCULINK and VIVEXX). Blood flow inside the carotid sinus is also differently affected by the presence of stent. While VIVEXX and CRISTALLO allow blood to flow inside the carotid sinus reproducing the hemodynamic pattern of the unstented case, XACT and ACCULINK produce a larger area with steady blood flow. Peak blood flow velocity also differs among the investigated cases. The maximum velocity is 56.79 cm s^{-1} in the control model, is reduced to 49.88 cm s^{-1} in VIVEXX, 51.84 cm s^{-1}

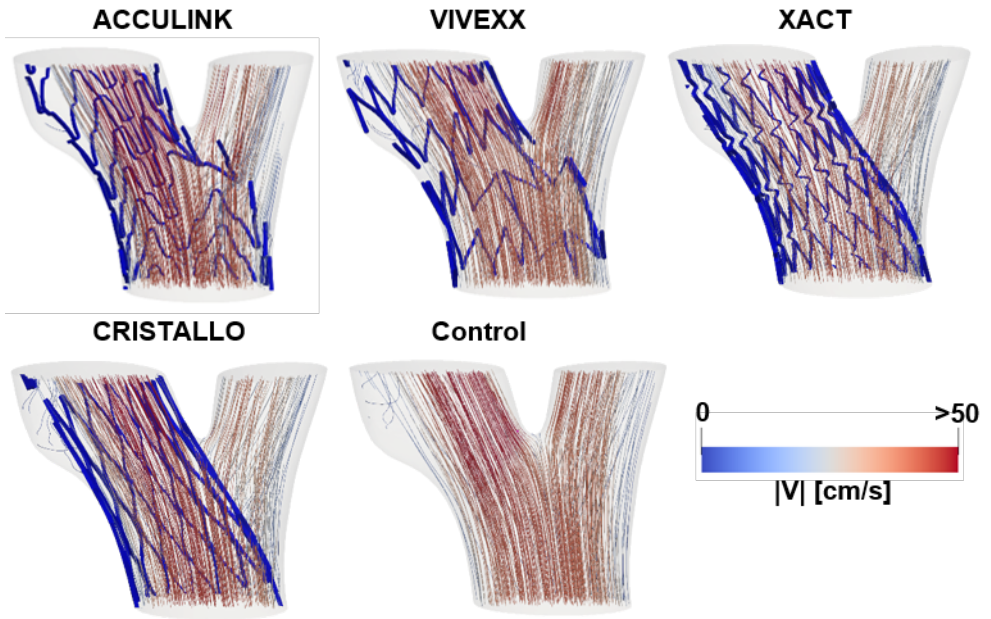


Figure 6.3: Impact of stenting on the blood flow field at the carotid bifurcation. The figures show the streamlines at systolic peak for all the investigated models. Flow is overall laminar in the CONTROL model, with recirculation at the carotid sinus. After CAS, the stents do not alter the laminarity, but small flow disturbances can be detected downstream the struts in the carotid bifurcation.

in XACT, 54.66 cm s^{-1} in CRISTALLO models, and incremented to 58.5 cm s^{-1} in ACCULINK model.

6.8 Impact of stenting on arterial resistance

Figure 6.4 summarizes the resistances of the ICA and ECA computed as defined in section 6.6. ICA resistance is greater than ECA resistance in the CONTROL model (278 vs $219 \text{ dynes/cm}^2/\text{cm}^3$).

6.9. Impact of stenting on TAWSS distribution

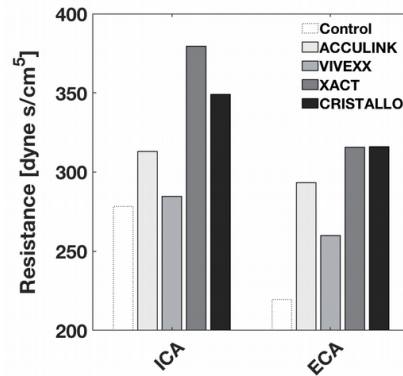


Figure 6.4: Impact of stenting on ICA and ECA flow resistances. ICA resistance is greater than ECA resistance in both pre- and post-CAS models. The stent implant causes an increase of the flow resistances in both vessels, to a greater extent in stents with closed cells at the bifurcation.

The stent implant increases the resistance values of both vessels, but at different extent depending on the cell configuration. Stents with closed cells at the ECA ostium (i.e., XACT and CRISTALLO) are characterized by higher resistances both at ICA and ECA comparing with open-cell stents (i.e., ACCULINK and VIVEXX). Comparing to the unstented control, the percentage increase of vascular resistance is greater in the ECA for each investigated model (+33% vs +12%, +18% vs +2%, +44% vs +36%, +44% vs +25% respectively for stents ACCULINK, VIVEXX, XACT and CRISTALLO), although the ICA resistances continue to be higher than ECA resistances.

6.9 Impact of stenting on TAWSS distribution

Finally, figures 6.5 and 6.6 describe the TAWSS distribution in the investigated cases. Considering the thresholds for TAWSS proposed by Malek and colleagues [72] to differentiate between athero-

genic, atheroprotective and thrombogenic blood flow, the CONTROL carotid is exposed for $96.3 \pm 0.21\%$ ($7.77 \pm 0.15 \text{ cm}^2$) of the total area ($8.08 \pm 0.18 \text{ cm}^2$) to an atheroprotective flow, for $3.44 \pm 0.2\%$ ($0.28 \pm 0.022 \text{ cm}^2$) to an atherogenic flow, and for $0.1 \pm 0.00\%$ ($0.0083 \pm 0.00 \text{ cm}^2$) to a thrombogenic flow. Low TAWSS are localized at the carotid sinus, while high TAWSS are found at the carotid bifurcation where the blood flow impacts the carotid wall. The effect of CAS is two-fold: on one side, the apposed stent accentuates the TAWSS distribution observed in the CONTROL configuration by increasing the low TAWSS area at the carotid sinus and decreasing the high TAWSS area at the bifurcation. On the other side, the stent struts in contact with the vascular wall of the CCA and ICA produce intra-strut atherogenic regions, whose particular distribution along the stented segment is determined by the specific stent geometry. In all models, low intra-strut TAWSS are mostly found in the most proximal portion of the stented segment, i.e., in the transition zone between unstented and stented CCA, but at different extent: low TAWSS area accounts for 16.30% (1.34 cm^2) in VIVEXX, 18.99% (1.73 cm^2) in CRISTALLO, 21.14% (1.74 cm^2) in XACT and 28.72% (2.32 cm^2) in ACCULINK. Interestingly, low TAWSS are localized in the whole areas of the closed-cells of the XACT stent, while distribute around the struts in the open-cell and hybrid-cell designs. As anticipated earlier, together with the increase of the areas exposed to atherogenic TAWSS, the implant of the stent decreases the areas exposed to high TAWSS, yet very small in the control condition, becoming less than 1% of the total stented area in the post-CAS configuration. As a consequence of the stent implant, areas exposed to atheroprotective blood flow are also reduced: 49.36% (4.05 cm^2) in XACT, 56.68% (4.58 cm^2) in ACCULINK, 56.99% (5.2 cm^2) in CRISTALLO and 58.80% (4.84 cm^2) in VIVEXX. It is worth to notice that the sum of the percentage areas exposed to low, mid and high TAWSS in each stented model does not bring to the unit: the area describing the contact between the vessel arterial wall and the stented has been in fact filtered out as described in section 6.6. It is therefore possi-

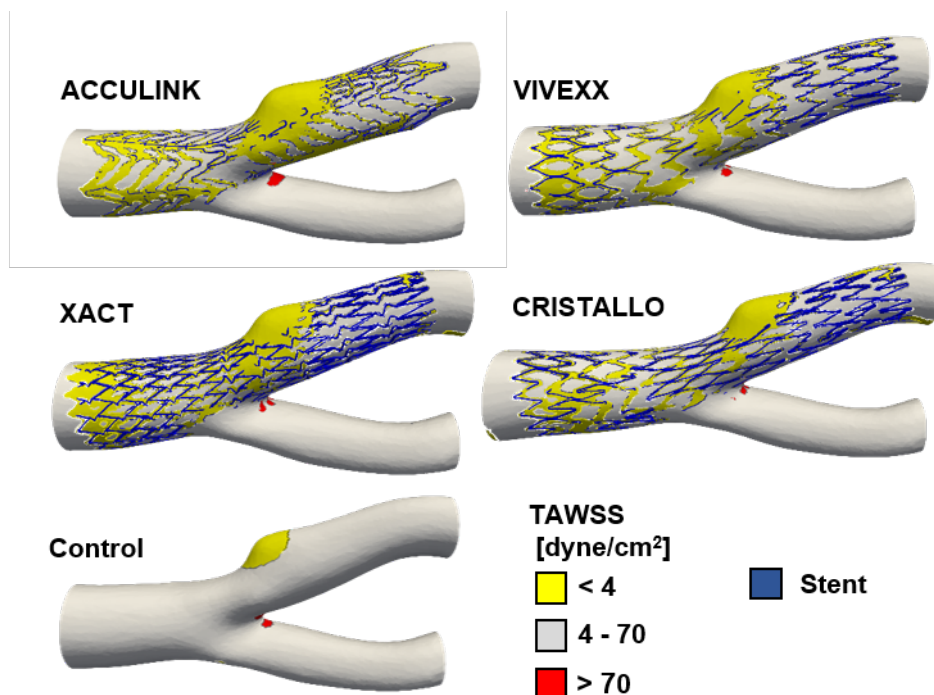


Figure 6.5: Impact of stenting on TAWSS distribution. After CAS, low (atherogenic) TAWSS areas are mostly distributed at the carotid bulb and inside the stent struts, particularly in the most proximal portion of the stented segment, i.e., in the transition zone between unstented and stented CCA. In the control model, low TAWSS are found only at the carotid sinus.

able to extrapolate also a measure of such an area, which accounts for 14.55% in ACCULINK, 24.01% in CRISTALLO, 24.89% in VIVEXX and 29.48% in XACT.

6.10 Analysis of the results

In this study, we aimed to evaluate the differences of the hemodynamics in a post-stenting patient-specific carotid artery resulting

6. Carotid stenting, hemodynamics and restenosis

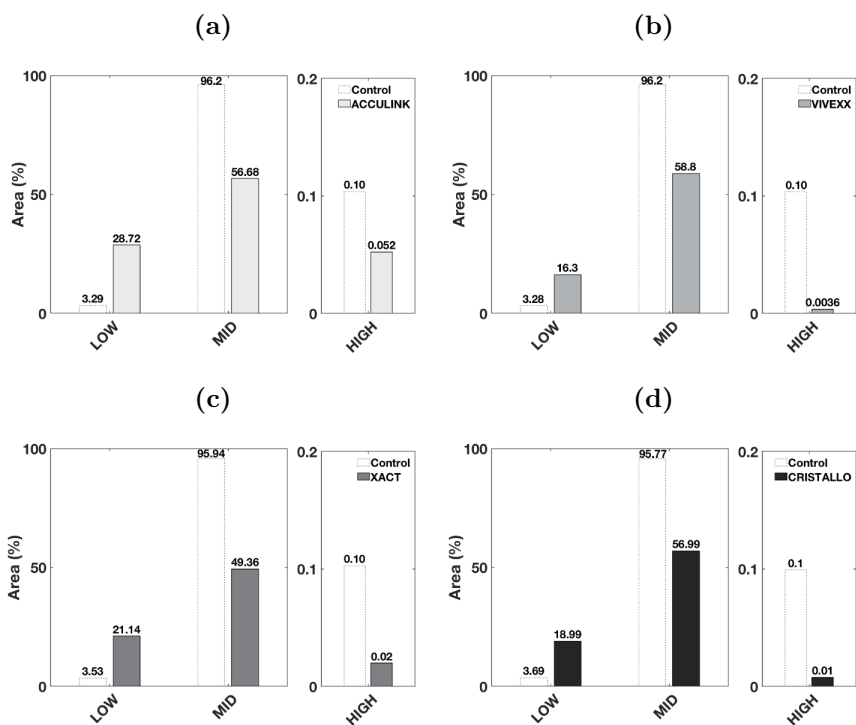


Figure 6.6: Impact of stenting on TAWSS areas. Comparing with control model, the implant of the stent a) increases the low (atherogenic) TAWSS area, b) decreases the high (thrombogenic) TAWSS area and c) decreases the mid (athero-prone) TAWSS area. The percentage areas differ among the investigated cases: (a) comparison between ACCULINK and CONTROL; (b) comparison between VIVEXX and CONTROL; (c) comparison between XACT and CONTROL; and, (d) comparison between CRISTALLO and CONTROL.

from the implant of four different commercial stents (ACCULINK, VIVEXX, XACT and CRISTALLO). We extracted the STL surfaces of the post-CAS carotid lumen and implanted stents from the FE simulations of virtual stent deployment performed previously by our group [136, 135], and set-up CFD analyses according to the framework developed in chapter 5.

The results show that, comparing to the control case, the implantation of the endovascular device does not significantly alter the flow regime within the post-CAS carotid, which continues to be laminar in all cases. A similar observation was done by Johari and colleagues [105], and reflects the fact that the thin shape of the stent struts induce a very small perturbation on the flow field. Furthermore, such a perturbation is localized only downstream the struts protruding inside the carotid bifurcation, where the blood velocity is higher.

In the present study, the stents bridge the CCA and the ICA, forming a net of struts whose density is somehow proportional to the areas of the cells at the bifurcation. In the post-CAS configuration of all the investigated models, the presence of a physical barrier at ECA ostium impeding the blood to flow freely causes the observed increase of its vascular resistance. In particular, the higher percentage increase of ECA resistance observed for XACT and CRISTALLO compared to ACCULINK and VIVEXX stents is compatible with the fact that the former have significantly smaller cell areas at the bifurcation [135]. The change of vascular resistance in the post-CAS carotid artery was measured by other authors. Kabinejadian and co-workers measured a post-CAS ECA resistance 2.8 times higher than that found in the CONTROL configuration, while the ICA resistance did not change following treatment. In that study, the authors simulated the implant of a covered stent, whose membrane across the bifurcation is likely responsible for the higher increase of ECA resistance comparing to our results [54]. De Santis et al. also measured an increase of ECA resistance after CAS with XACT and ACCULINK stents, and a decrease of ICA resistance, but the method used to assess such resistances was different from the one used in this study [30]. If the

impact of CAS on ECA resistance found in this study is in accordance with that found in the literature, the same does not hold for the ICA resistance. In [54, 30] the ICA was characterized by a lower resistance both in the pre- both in the post-CAS configuration. In our case, the ICA resistance is always higher. We believe that this can be explained by the particular set of BCs chosen in the CFD simulations. Specifically, we impose a flow split ICA/ECA of 65/35, and a zero-pressure at the ECA outlet. After the stent implantation, the ECA resistance increases due to the post-CAS geometric changes and the presence of the struts at the ECA ostium. Since the pressure at the ECA outlet must remain null, the CCA pressure increases to guarantee the imposed flow in the ECA. In turn, the ICA pressure is shifted accordingly to guarantee the imposed flow in the ICA. In essence, the ECA and ICA resistances increase because the increase of ECA and ICA pressures do not correspond to a variation of the respective flows, since the last are set a priori as BCs.

Finally, we compared the area exposed to low, mid and high TAWSS among the investigated cases. Low TAWSS have been associated to atherogenesis, mid TAWSS to atheroprotection, and high TAWSS to thrombogenesis [72]. Results show that, in the control case, low TAWSS areas are mainly located in the carotid sinus, and that the stent implant determines a) an increase of the low TAWSS area in the carotid sinus and b) the formation of low TAWSS intra-strut areas, specifically at the transition between unstented and stented CCA. A few spots of high TAWSS are instead located at the carotid bifurcation both in the control and the stented models. The TAWSS patterns in the control and stented cases have also been confirmed by previous studies, which report atherogenic areas in the carotid bulb [105, 136, 137] and thrombogenic areas around the flow divider [105]. We did not find a clear association between the areas of the stent cells in contact with the vascular wall and intra-strut low TAWSS area. In increasing order of low TAWSS area we find: VIVEXX (average cell area: 6.1 mm^2 [135]), CRISTALLO (average cell area: 9.4 mm^2 [135]), XACT (average cell area: 2.6 mm^2 [135]) and ACCULINK (average

cell area: 7.2 mm^2 [135]). These results disagree with that found by Johari and colleagues, who found that both closed-cell stent models (stents WALLSTENT and XACT) had larger atherogenic areas than open-cell stent ACCULINK. However, as specified in section 6.6, we report the *intra-strut* low TAWSS area (i.e., we don't include the low TAWSS regions *under* the stent struts). Obviously, since each stent design is characterized by a different strut density and consequent appposable area [30], the results are altered. Whether to include the area in contact with the stent in the calculation of the atherogenic region arising in the post-CAS carotid is unclear. In the regions where the struts contact with the vascular wall, the velocity is zero (in body-fitted meshes) or close to zero (in our case); consequently, the TAWSS are trivially low. We believe that the inclusion of these regions introduces a confounding factor for the evaluation of the performance of a particular stent design in relation to the in-stent restenosis (ISR) risk, because the quantification of such areas relates to the density of a stent and its ability to contact the vessel wall rather than its tendency to produce intra-strut atherogenic patterns.

6.11 Final comments and future developments

With the aim of showing a potential application of the computational framework previously developed, in this chapter we have simulated the post-CAS hemodynamics resulting from the implant of four different commercial stents in a realistic model of carotid bifurcation. Specifically, the impact of CAS on carotid hemodynamics was assessed with respect to alterations of blood flow pattern, ICA and ECA resistances, and TAWSS distribution. The study showed that stenting did not significantly alter carotid bulk flow dynamics, but increased the ECA resistance (particularly closed-cell stent designs) and induced atherogenic areas at the carotid sinus and near the

stent struts. In this regard, results did not show a clear association between stent cell area and ISR risk, suggesting that other factors should be taken into account for a more comprehensive evaluation of the optimal stent cell design. In particular, the specific shape of the elementary cell might be an important aspect to investigate in future studies as the orientation in space of the struts may determine a different impact with the blood flowing near the vascular walls with consequent different formation of recirculation areas on the walls.

The presented application of the developed computational framework was clearly preliminary as it contains a number of aspects that should be investigated in future studies. First of all, the reliability of the flow prediction should be validated towards experimental/clinical data. At this purpose, an experimental set-up reproducing the stent implant inside the silicon mock artery used in this study could be exploited to validate, through experimental techniques such as particle image velocimetry, the flow characteristics resulting from the CFD simulation with immersed method. Furthermore, with availability of clinical images (such as 4-dimensional magnetic resonance (MR) imaging) of post-CAS blood flow, the hemodynamics predicted by the proposed framework could be validated towards clinical data. However, it is important to note that the current technology is affected by rather small spatial resolution (around 2.5 mm per voxel side) which is insufficient to visualize the flow pattern around the immersed stent strut, whose typical dimension is around 0.2 mm. Therefore, the clinical validation can be assessed only for macroscopic quantities (such as flow split or vascular resistance), as the detailed description of the flow pattern around the stent strut can be assessed only through numerical simulations. Another aspect that should be addressed is the choice of the correct BCs. In this study, we applied a flow split ICA/ECA of 65/35, and a zero-pressure at the ECA outlet. Evidently, the application of more realistic flow features at the outflows would likely allow a more reliable evaluation of the post-CAS vascular resistances. Therefore, other outflow boundary conditions, e.g., 1-D lumped parameter outflow models, should be explored in future stud-

6.11. Final comments and future developments

ies. Finally, a multi-patient study involving the simulation of post-CAS hemodynamics in different realistic models of carotid arteries should be carried out. Indeed, the performance of a stent cannot be evaluated without considering the anatomic variability of the hosting vessel: a specific stent might perfectly adapt to the anatomy of one carotid bifurcation, or be highly malapposed in another.

Chapter 7

Conclusions

The research activity described in this dissertation can be collocated in the area of computational biomechanics, as it exploits and improves methods of medical imaging processing, computational fluid dynamics (CFD) and data analysis to investigate different aspects concerning the biomechanics of the carotid artery, particularly focusing on the role that carotid morphometry and flow may play during onset, development and post-treatment follow-up of vascular disorders. In this dissertation, the analysis of the vascular pathology has been approached from different viewpoints. In the first part of the thesis we focused on how the morphometry of the carotid and vertebral arteries might be responsible for the reduction of the blood flow observed in hypertensive patients. Moving to a different clinical scenario, in the second part of the thesis we focused on how stenting might affect the blood flow in the treated carotid artery. The specific clinical application has driven the technological innovation proposed in this dissertation. In particular, in the first part of the thesis we implemented a framework for the objective splitting and morphometric analysis of carotid and vertebral arteries into different vascular tracts basing on the curvature analysis of the reconstructed centerlines. In the second part, instead, we set up a framework for

the CFD analysis of the hemodynamics in the stented carotid artery exploiting the immersed method for the inclusion of the endovascular device inside the blood domain.

This thesis highlights the importance of using computational tools for the assessment of the biomechanical mechanisms involved in vascular diseases, potentially applicable in every aspect of the pathology including pathophysiology investigation, pre-operative surgical planning, endovascular device performance and evaluation of post-treatment follow-up. In this chapter we briefly resume the main scientific results obtained in this dissertation.

The clinical aim of the first part of the thesis was to analyze the local and global morphometry of the major intracranial arteries in normotensive and hypertensive subjects and assess their relationship with arterial flow and blood pressure. We hypothesised that decreasing vascular mean cross-sectional area, increasing tortuosity and increasing vessel length are associated with decreased arterial flow, or in other words that hypertensive subjects exhibit narrower, more tortuous and longer vessels compared to normotensives.

Therefore, we decided to build a semi-automatic platform for the systematic subdivision and morphometric analysis of the right and left intracranial internal carotid arteries (ICAs), and right and left intracranial vertebral arteries (VAs). As the subdivision of these vessels into different anatomical tracts had to be based on the characteristics of the centerline curvature, we first focused on the implementation of *ad hoc* algorithms to improve accuracy and efficiency of curvature estimation over classical curvature computation methods (e.g., by finite differences). Preliminary tests showed that centerline curvatures computed by finite differences were in fact extremely noisy unless high resampling length and smoothing algorithms were used at the expense of an unacceptable loss of accuracy. Therefore, the solution consisted of first re-converting the reconstructed centerline to an approximating analytical function, and then performing the exact derivatives. Following Sangalli et al. [86], we chose spatially adaptive

free-knot regression splines (SARS) as approximating analytical functions, i.e., regression splines where the number and position of knots are not fixed in advance, but chosen in a way to minimize a penalized sum of squared errors criterion [84]. We coded the algorithm for the search of optimal knots and the generation of SARS in Matlab and presented some implementation details in the thesis. We acknowledge that this part of the manuscript does not add any new concept or idea to the existing literature; however, while the use of SARS has been recognized as an optimal method for the vascular centerline reconstruction, implementation details are difficult to find and the relative papers are not immediate to replicate. Therefore, by including it in the thesis, we hope to support researchers in the field who may want to implement such methods in the future. We then integrated the implemented centerline reconstruction methods into a computational platform for the semi-automatic objective anatomic subdivision and morphometric analysis of the intracranial carotid and vertebral arteries. The tool was used to perform the morphometric analysis of the cerebral vessels in 112 normotensive/hypertensive subjects to assess the relationship between arterial morphometry, blood flow and systemic blood pressure. The study was conducted during the visit at the Bristol Heart Institute (UK). The clinicians showed an enthusiastic response, appreciating the capability of the tool to perform vascular splitting and morphometric analysis in a semi-automated way, reducing the measuring errors associated to manual measures. Results showed that carotid flow was reduced in hypertensives, but the morphology of the intracranial ICA did not appear to be the cause, suggesting that the link between hypertension and morphometry of intracranial ICA is incidental. On the other hand, results suggested a possible link between hypertension and VA geometry, where in particular an increased length and tortuosity might be associated to vertebral flow decrease. The study adds evidence to the hypothesis that the morphometry of VAs may be involved in the onset of essential hypertension paving the way for supplemental diagnostic evaluation and risk assessment of this pathology.

Moving to a different clinical perspective, in the second part of the thesis we aimed to assess the impact on the blood flow resulting from the implant of four different commercial stents (ACCULINK, VIVEXX, XACT and CRISTALLO) in a realistic model of carotid artery bifurcation.

Few works deal with the analysis of hemodynamics in patient-specific post-carotid artery stenting (CAS) models, due to difficulties in the creation of analysis-suitable meshes able to catch the protrusion of the slender stent struts into the carotid blood volume. Therefore, we decided to build a framework for the simulation of post-CAS hemodynamics adopting a hybrid body-fitted/immersed approach: the fluid mesh is “body-fitted” with respect to the carotid walls while is “immersed” with respect to the stent. To achieve this task, we first created a meshing tool for the semi-automatic local mesh refinement in proximity of the endovascular device, then we set up the CFD analysis with hybrid approach tuning the meshing and simulation parameters for our target problem. The implemented meshing tool requires in input the STL surfaces of the vascular lumen and the deployed stent, and returns in output the tetrahedral mesh of the blood domain locally refined where the stent is immersed, ready for the CFD simulation. Also, it automatically identifies and labels the boundaries of the computational domain to facilitate the application of the boundary conditions during the simulation set-up. Once the user sets specific parameters, the mesh refinement is performed automatically by defining three regions, each characterized by three different mesh sizes: a spherical region, centred at points *on* or *inside* the surface of the endovascular device, where the mesh is refined; a surrounding shell-like region, where the element size grows gradually at a prescribed growth rate; a region where the mesh is not refined. By working with STL surfaces, the proposed meshing tool allows the user to easily control which regions need to be refined (and which not) with geometries of any complexity. The mesh characteristics strongly determine the accuracy of the CFD simulation, especially

when an immersed approach is used, therefore we performed mesh sensitivity tests to assess the optimal grid characteristics. We found that the element size should be around 10-15% of the smallest dimension of the strut in the refined zone near the immersed device, around 0.03 cm in the unrefined region, and grow with rate of 1.2 between the two regions. Also, time sensitivity tests were performed to assess the optimal temporal parameters of the CFD simulation. We found the temporal resolution of the velocity and its derivatives (e.g., wall shear stress (WSS)) requires time steps below 0.002 s, a condition that can be relaxed to 0.01 s with integral quantities (e.g., flowrate). Also, we found that at least two cardiac cycles should be simulated to discard the first one where initial transitory effects exist. A preliminary application of the implemented framework was presented in the last chapter of this dissertation, where we simulated the post-CAS hemodynamics in a comparative study with four commercial stents implanted in a realistic model of carotid bifurcation. Specifically, the impact of CAS on carotid hemodynamics was assessed with respect to alterations of blood flow pattern, ICA and external carotid artery (ECA) resistances, and time-averaged wall shear stress (TAWSS) distribution. Results showed that, comparing to the control case, the implantation of the endovascular device does not significantly alter the bulk flow within the post-CAS carotid, as the thin shape of the stent struts induce a very small perturbation on the flow field, however mainly localized downstream the struts protruding inside the carotid bifurcation where the blood velocity is higher. We found that stenting induces a significant increase of the ECA resistance due to the presence of the strut net at its ostium impeding the blood to flow freely, consistently with the observation that the highest resistance increase was associated to stents with smaller cell areas. Finally, we compared the carotid wall areas exposed to low (atherogenic), mid (atheroprotective) and high (thrombogenic) TAWSS among the investigated cases. Results showed that, in the control case, low TAWSS areas are mainly located in the carotid sinus, and that the stent implant determines a) an increase of the low

TAWSS area in the carotid sinus and b) the formation of low TAWSS intra-strut areas, specifically at the transition between unstented and stented common carotid artery (CCA). A few spots of high TAWSS are instead located at the carotid bifurcation both in the control and the stented models. We did not find a clear association between the areas of the stent cells in contact with the vascular wall and intra-strut low TAWSS area. The study shows the potentialities of the proposed computational framework for the hemodynamic analysis of the post-stenting carotid artery, but is preliminary: future studies involving more complex modelling assumptions as well as the validation of the performance of the method on a more numerous cohort of datasets are demanded.

Bibliography

- [1] Dinko Susic. Hypertension, aging, and atherosclerosis: the endothelial interface. *Medical clinics of north America*, 81(5):1231–1240, 1997.
- [2] DG1 Harrison, J Widder, I Grumbach, W Chen, M Weber, and C Searles. Endothelial mechanotransduction, nitric oxide and vascular inflammation. *Journal of internal medicine*, 259(4):351–363, 2006.
- [3] Victoria Cachofeiro, María Miana, Beatriz Martín-Fernandez, Sandra Ballesteros, Gloria Balfagon, Vicente Lahera, et al. Inflammation: a link between hypertension and atherosclerosis. *Current Hypertension Reviews*, 5(1):40–48, 2009.
- [4] Michael A Gimbrone. Endothelial dysfunction and the pathogenesis of atherosclerosis. In *Atherosclerosis V*, pages 415–425. Springer, 1980.
- [5] Peter L Weissberg. Atherogenesis: current understanding of the causes of atheroma. *Heart*, 83(2):247–252, 2000.
- [6] Michael J Davies and Anthony C Thomas. Plaque fissuring—the cause of acute myocardial infarction, sudden ischaemic death, and crescendo angina. *British heart journal*, 53(4):363, 1985.

- [7] Mark Fisher, Annlia Paganini-Hill, Aldana Martin, Michele Cosgrove, James F Toole, Henry JM Barnett, and John Norris. Carotid plaque pathology: thrombosis, ulceration, and stroke pathogenesis. *Stroke*, 36(2):253–257, 2005.
- [8] Walter Johnson, Oyere Onuma, Mayowa Owolabi, and Sonal Sachdev. Stroke: a global response is needed. *Bulletin of the World Health Organization*, 94(9):634, 2016.
- [9] R Wayne Alexander. Hypertension and the pathogenesis of atherosclerosis: oxidative stress and the mediation of arterial inflammatory response: a new perspective. *Hypertension*, 25(2):155–161, 1995.
- [10] Hai-Chao Han. Twisted blood vessels: symptoms, etiology and biomechanical mechanisms. *Journal of vascular research*, 49(3):185–197, 2012.
- [11] Simina Ciurică, Marilucy Lopez-Sublet, Bart L Loeys, Ibtissem Radhouani, Nalin Natarajan, Miikka Vikkula, Angela HEM Maas, David Adlam, and Alexandre Persu. Arterial tortuosity: Novel implications for an old phenotype. *Hypertension*, 73(5):951–960, 2019.
- [12] Colin G Caro, Denis J Doorly, Maria Tarnawski, Katherine T Scott, Quan Long, and Charles L Dumoulin. Non-planar curvature and branching of arteries and non-planar-type flow. *Proceedings of the Royal Society of London. Series A: Mathematical, Physical and Engineering Sciences*, 452(1944):185–197, 1996.
- [13] KB Chandran. Flow dynamics in the human aorta. *Journal of biomechanical engineering*, 115(4B):611–616, 1993.
- [14] Umberto Morbiducci, Annette M Kok, Brenda R Kwak, Peter H Stone, David A Steinman, Jolanda J Wentzel, et al.

BIBLIOGRAPHY

- Atherosclerosis at arterial bifurcations: evidence for the role of haemodynamics and geometry. *Thromb Haemost*, 115(3):484–492, 2016.
- [15] Konstantinos C Koskinas, Yiannis S Chatzizisis, Antonios P Antoniadis, and George D Giannoglou. Role of endothelial shear stress in stent restenosis and thrombosis: pathophysiologic mechanisms and implications for clinical translation. *Journal of the American College of Cardiology*, 59(15):1337–1349, 2012.
- [16] Mark Fisher and Sherry Fieman. Geometric factors of the bifurcation in carotid atherogenesis. *Stroke*, 21(2):267–271, 1990.
- [17] Jonathan B Thomas, Luca Antiga, Susan L Che, Jaques S Milner, Dolores A Hangan Steinman, J David Spence, Brian K Rutt, and David A Steinman. Variation in the carotid bifurcation geometry of young versus older adults: implications for geometric risk of atherosclerosis. *Stroke*, 36(11):2450–2456, 2005.
- [18] Thanh G Phan, Richard J Beare, Damien Jolley, Gita Das, Mandy Ren, Kitty Wong, Winston Chong, Matthew D Sinnott, James E Hilton, and Velandai Srikanth. Carotid artery anatomy and geometry as risk factors for carotid atherosclerotic disease. *Stroke*, 43(6):1596–1601, 2012.
- [19] Sang-Wook Lee, Luca Antiga, J David Spence, and David A Steinman. Geometry of the carotid bifurcation predicts its exposure to disturbed flow. *Stroke*, 39(8):2341–2347, 2008.
- [20] Daniel Birchall, Azfar Zaman, Jacob Hacker, Gavin Davies, and David Mendelow. Analysis of haemodynamic disturbance in the atherosclerotic carotid artery using computational fluid dynamics. *European radiology*, 16(5):1074–1083, 2006.
- [21] Samuel A Kock, Jens V Nygaard, Nikolaj Eldrup, Ernst-Torben Fründ, Anette Klærke, William P Paaske, Erling Falk, and

- W Yong Kim. Mechanical stresses in carotid plaques using mri-based fluid–structure interaction models. *Journal of biomechanics*, 41(8):1651–1658, 2008.
- [22] Dalin Tang, Zhongzhao Teng, Gador Canton, Chun Yang, Marina Ferguson, Xueying Huang, Jie Zheng, Pamela K Woodard, and Chun Yuan. Sites of rupture in human atherosclerotic carotid plaques are associated with high structural stresses: an in vivo mri-based 3d fluid-structure interaction study. *Stroke*, 40(10):3258–3263, 2009.
- [23] Hao Gao, Quan Long, Martin Graves, Jonathan H Gillard, and Zhi-Yong Li. Carotid arterial plaque stress analysis using fluid–structure interactive simulation based on in-vivo magnetic resonance images of four patients. *Journal of biomechanics*, 42(10):1416–1423, 2009.
- [24] JFR Paton, CJ Dickinson, and G Mitchell. Harvey cushing and the regulation of blood pressure in giraffe, rat and man: introducing ”cushing’s mechanism”. *Experimental physiology*, 94(1):11–17, 2009.
- [25] Esther AH Warnert, Jonathan CL Rodrigues, Amy E Burchell, Sandra Neumann, Laura EK Ratcliffe, Nathan E Manghat, Ashley D Harris, Zoe Adams, Angus K Nightingale, Richard G Wise, et al. Is high blood pressure self-protection for the brain? *Circulation research*, 119(12):e140–e151, 2016.
- [26] CJ Dickinson and AD Thomson. Vertebral and internal carotid arteries in relation to hypertension and cerebrovascular disease. *The Lancet*, 274(7090):46–48, 1959.
- [27] P Pancera, M Ribul, B Presciuttini, and A Lechi. Prevalence of carotid artery kinking in 590 consecutive subjects evaluated by echocolor Doppler. is there a correlation with arterial hypertension? *Journal of internal medicine*, 248(1):7–12, 2000.

BIBLIOGRAPHY

- [28] Ugo Oliviero, Giovanna Scherillo, Cosma Casaburi, Marilena Di Martino, Angela Di Gianni, Raffaella Serpico, Serafino Fazio, and Luigi Saccà. Prospective evaluation of hypertensive patients with carotid kinking and coiling: an ultrasonographic 7-year study. *Angiology*, 54(2):169–175, 2003.
- [29] Josephus LM van Rooij, Richard AP Takx, Birgitta K Velthuis, Jan Willem Dankbaar, and Pim A de Jong. Coiling of the internal carotid artery is associated with hypertension in patients suspected of stroke. *Clinical Neuroradiology*, pages 1–6, 2020.
- [30] Gianluca De Santis, Michele Conti, Bram Trachet, Thomas De Schryver, Matthieu De Beule, Joris Degroote, Jan Vierendeels, Ferdinando Auricchio, Patrick Segers, Pascal Verdonck, et al. Haemodynamic impact of stent-vessel (mal) apposition following carotid artery stenting: mind the gaps! *Computer methods in biomechanics and biomedical engineering*, 16(6):648–659, 2013.
- [31] Michele Conti, Chris Long, Michele Marconi, Raffaella Berchiolli, Yuri Bazilevs, and Alessandro Reali. Carotid artery hemodynamics before and after stenting: A patient specific cfd study. *Computers & Fluids*, 141:62–74, 2016.
- [32] Alain Bouthillier, Harry R Van Loveren, and Jeffrey T Keller. Segments of the internal carotid artery: a new classification. *Neurosurgery*, 38(3):425–433, 1996.
- [33] Thomas S Lee, Yadranko Ducic, Eli Gordin, and David Stroman. Management of carotid artery trauma. *Craniomaxillofacial trauma & reconstruction*, 7(3):175–189, 2014.
- [34] G Garcia-Cardena and MA Gimbrone. Biomechanical modulation of endothelial phenotype: implications for health and disease. In *The Vascular Endothelium II*, pages 79–95. Springer, 2006.

- [35] Jordan S Pober, Wang Min, and John R Bradley. Mechanisms of endothelial dysfunction, injury, and death. *Annual Review of Pathology: Mechanisms of Disease*, 4:71–95, 2009.
- [36] Sarah Jane George and Jason Johnson. *Atherosclerosis: molecular and cellular mechanisms*. John Wiley & Sons, 2010.
- [37] Russell Ross. Atherosclerosis - an inflammatory disease. *New England journal of medicine*, 340(2):115–126, 1999.
- [38] THOMAS A ISCHINGER. Carotid stenting: which stent for which lesion? *Journal of Interventional Cardiology*, 14(6):617–623, 2001.
- [39] Pascal Meier, Guido Knapp, Umesh Tamhane, Seemant Chaturvedi, and Hitinder S Gurm. Short term and intermediate term comparison of endarterectomy versus stenting for carotid artery stenosis: systematic review and meta-analysis of randomised controlled clinical trials. *Bmj*, 340, 2010.
- [40] Daniel Yavin, Derek J Roberts, Michael Tso, Garnette R Sutherland, Misha Eliasziw, and John H Wong. Carotid endarterectomy versus stenting: a meta-analysis of randomized trials. *Canadian journal of neurological sciences*, 38(2):230–235, 2011.
- [41] KI Paraskevas, EL Kalmykov, and AR Naylor. Stroke/death rates following carotid artery stenting and carotid endarterectomy in contemporary administrative dataset registries: a systematic review. *European Journal of Vascular and Endovascular Surgery*, 51(1):3–12, 2016.
- [42] M Hassan Murad, David N Flynn, Mohamed B Elamin, Gordon H Guyatt, Robert W Hobson II, Patricia J Erwin, and Victor M Montori. Endarterectomy vs stenting for carotid artery stenosis: a systematic review and meta-analysis. *Journal of vascular surgery*, 48(2):487–493, 2008.

BIBLIOGRAPHY

- [43] A Kastrup and K Gröschel. Carotid endarterectomy versus carotid stenting: an updated review of randomized trials and subgroup analyses. *Acta Chirurgica Belgica*, 107(2):119–128, 2007.
- [44] Simon Morr, Ning Lin, and Adnan H Siddiqui. Carotid artery stenting: current and emerging options. *Medical Devices (Auckland, NZ)*, 7:343, 2014.
- [45] Dougal R McClean and Neal L Eigler. Stent design: implications for restenosis. *Reviews in cardiovascular medicine*, 3(S5):16–22, 2002.
- [46] Martin Schillinger, Manfred Gschwendtner, Bernhard Reimers, Johannes Trenkler, Luc Stockx, Johann Mair, Sumaira Macdonald, Franz Karnel, Kurt Huber, and Erich Minar. Does carotid stent cell design matter? *Stroke*, 39(3):905–909, 2008.
- [47] Damon S Pierce, Eric B Rosero, J Gregory Modrall, Beverley Adams-Huet, R James Valentine, G Patrick Clagett, and Carlos H Timaran. Open-cell versus closed-cell stent design differences in blood flow velocities after carotid stenting. *Journal of vascular surgery*, 49(3):602–606, 2009.
- [48] Rami O Tadros, Constantinos T Spyris, Ageliki G Vouyouka, Christine Chung, Prakash Krishnan, Margaret W Arnold, Michael L Marin, and Peter L Faries. Comparing the embolic potential of open and closed cell stents during carotid angioplasty and stenting. *Journal of vascular surgery*, 56(1):89–95, 2012.
- [49] Christopher L Skelly, Katherine Gallagher, Ronald M Fairman, Jeffrey P Carpenter, Omaidia C Velazquez, Shane S Parmer, and Edward Y Woo. Risk factors for restenosis after carotid artery angioplasty and stenting. *Journal of vascular surgery*, 44(5):1010–1015, 2006.

- [50] J Gunn and D Cumberland. Does stent design influence restenosis? *European heart journal*, 20(14):1009–1013, 1999.
- [51] Xinke Yao, Zhengze Dai, Xu Zhang, Jie Gao, Gelin Xu, Yan Cai, and Zhiyong Li. Carotid geometry as a predictor of in-stent neointimal hyperplasia - a computational fluid dynamics study -. *Circulation Journal*, pages CJ–18, 2019.
- [52] Alexey V Kamenskiy, Iraklis I Pipinos, Yuris A Dzenis, Jai Bikhchandani, Prateek K Gupta, Nick Phillips, Syed A Jaffar Kazmi, and Jason N MacTaggart. Effects of carotid artery stenting on arterial geometry. *Journal of the American College of Surgeons*, 217(2):251–262, 2013.
- [53] Gianluca De Santis, Bram Trachet, Michele Conti, Matthieu De Beule, Umberto Morbiducci, Peter Mortier, Patrick Segers, Pascal Verdonck, and Benedict Verheghe. A computational study of the hemodynamic impact of open-versus closed-cell stent design in carotid artery stenting. *Artificial organs*, 37(7):E96–E106, 2013.
- [54] Foad Kabinejadian, Fangsen Cui, Boyang Su, Asawinee Dandinid, Pei Ho, and Hwa Liang Leo. Effects of a carotid covered stent with a novel membrane design on the blood flow regime and hemodynamic parameters distribution at the carotid artery bifurcation. *Medical & biological engineering & computing*, 53(2):165–177, 2014.
- [55] Gail M Siewiorek, Ender A Finol, and Mark H Wholey. Clinical significance and technical assessment of stent cell geometry in carotid artery stenting. *Journal of Endovascular Therapy*, 16(2):178–188, 2009.
- [56] William E Lorensen and Harvey E Cline. Marching cubes: A high resolution 3d surface construction algorithm. *ACM SIGGRAPH computer graphics*, 21(4):163–169, 1987.

BIBLIOGRAPHY

- [57] N Byrne, M Velasco Forte, A Tandon, I Valverde, and T Husain. A systematic review of image segmentation methodology, used in the additive manufacture of patient-specific 3d printed models of the cardiovascular system. *JRSM cardiovascular disease*, 5:2048004016645467, 2016.
- [58] Will Schroeder, Lydia Ng, and Josh Cates. The itk software guide. 2003.
- [59] Luca Antiga, Marina Piccinelli, Lorenzo Botti, Bogdan Ene-Iordache, Andrea Remuzzi, and David A Steinman. An image-based modeling framework for patient-specific computational hemodynamics. *Medical & biological engineering & computing*, 46(11):1097, 2008.
- [60] James Albert Sethian. *Level set methods and fast marching methods: evolving interfaces in computational geometry, fluid mechanics, computer vision, and materials science*, volume 3. Cambridge university press, 1999.
- [61] Andrea Giachetti and Gianluigi Zanetti. Vascular modeling from volumetric diagnostic data: a review. *Current Medical Imaging*, 2(4):415–423, 2006.
- [62] Tamal K Dey and Wulue Zhao. Approximate medial axis as a voronoi subcomplex. In *Proceedings of the seventh ACM symposium on Solid modeling and applications*, pages 356–366, 2002.
- [63] Luca Antiga, Bogdan Ene-Iordache, and Andrea Remuzzi. Computational geometry for patient-specific reconstruction and meshing of blood vessels from mr and ct angiography. *IEEE transactions on medical imaging*, 22(5):674–684, 2003.
- [64] Umberto Morbiducci, Diego Gallo, Diana Massai, Raffaele Ponzini, Marco A Deriu, Luca Antiga, Alberto Redaelli, and Franco M Montecvecchi. On the importance of blood rheology

- for bulk flow in hemodynamic models of the carotid bifurcation. *Journal of biomechanics*, 44(13):2427–2438, 2011.
- [65] Sang-Wook Lee and David A Steinman. On the relative importance of rheology for image-based cfd models of the carotid bifurcation. 2007.
- [66] Umberto Morbiducci, Diego Gallo, Raffaele Ponzini, Diana Massai, Luca Antiga, Franco M Montevecchi, and Alberto Redaelli. Quantitative analysis of bulk flow in image-based hemodynamic models of the carotid bifurcation: the influence of outflow conditions as test case. *Annals of biomedical engineering*, 38(12):3688–3705, 2010.
- [67] Keri R Moyle, Luca Antiga, and David A Steinman. Inlet conditions for image-based cfd models of the carotid bifurcation: is it reasonable to assume fully developed flow? *Journal of biomechanical engineering*, 128(3):371–379, 2006.
- [68] Cristóbal Bertoglio, Alfonso Caiazzo, Yuri Bazilevs, Malte Braack, Mahdi Esmaily, Volker Gravemeier, Alison L Marsden, Olivier Pironneau, Irene E. Vignon-Clementel, and Wolfgang A. Wall. Benchmark problems for numerical treatment of backflow at open boundaries. *International journal for numerical methods in biomedical engineering*, 34(2):e2918, 2018.
- [69] Inc Ansys. *ANSYS CFX-Solver Theory Guide*. Southpointe, 275 Technology Drive, Canonsburg, PA 15317, 14.0 edition, 11 2011.
- [70] Juan M Jiménez and Peter F Davies. Hemodynamically driven stent strut design. *Annals of biomedical engineering*, 37(8):1483–1494, 2009.
- [71] Xin Liu, Heye Zhang, Lijie Ren, Huahua Xiong, Zhifan Gao, Pengcheng Xu, Wenhua Huang, and Wanqing Wu. Functional

BIBLIOGRAPHY

- assessment of the stenotic carotid artery by cfd-based pressure gradient evaluation. *American Journal of Physiology-Heart and Circulatory Physiology*, 311(3):H645–H653, 2016.
- [72] Adel M Malek, Seth L Alper, and Seigo Izumo. Hemodynamic shear stress and its role in atherosclerosis. *Jama*, 282(21):2035–2042, 1999.
- [73] Jennifer M Dolan, John Kolega, and Hui Meng. High wall shear stress and spatial gradients in vascular pathology: a review. *Annals of biomedical engineering*, 41(7):1411–1427, 2013.
- [74] Kwong Ming Tse, Peixuan Chiu, Heow Pueh Lee, and Pei Ho. Investigation of hemodynamics in the development of dissecting aneurysm within patient-specific dissecting aneurismal aortas using computational fluid dynamics (cfd) simulations. *Journal of biomechanics*, 44(5):827–836, 2011.
- [75] Oscar A Carretero and Suzanne Oparil. Essential hypertension: part i: definition and etiology. *Circulation*, 101(3):329–335, 2000.
- [76] Sandosh Padmanabhan, Mark Caulfield, and Anna F Dominiczak. Genetic and molecular aspects of hypertension. *Circulation research*, 116(6):937–959, 2015.
- [77] Matthew J Cates, C John Dickinson, Emma CJ Hart, and Julian FR Paton. Neurogenic hypertension and elevated vertebrobasilar arterial resistance: is there a causative link? *Current hypertension reports*, 14(3):261–269, 2012.
- [78] Matthew J Cates, Peter W Steed, Ana PL Abdala, Philip D Langton, and Julian FR Paton. Elevated vertebrobasilar artery resistance in neonatal spontaneously hypertensive rats. *Journal of applied physiology*, 111(1):149–156, 2011.

- [79] Nephtali Marina, Richard Ang, Asif Machhada, Vitaliy Kasyrov, Anastassios Karagiannis, Patrick S Hosford, Valentina Mosienko, Anja G Teschemacher, Pirkko Vihko, Julian FR Paton, et al. Brainstem hypoxia contributes to the development of hypertension in the spontaneously hypertensive rat. *Hypertension*, 65(4):775–783, 2015.
- [80] Alexander M Nixon, Murat Gunel, and Bauer E Sumpio. The critical role of hemodynamics in the development of cerebral vascular disease: a review. *Journal of neurosurgery*, 112(6):1240–1253, 2010.
- [81] Nataliya Romanko-Hrushchak. Mdcta diagnosis of cerebral vessel disease among patients with arterial hypertension. *Polish journal of radiology*, 78(3):28, 2013.
- [82] Yen-Yu Chen, A-Ching Chao, Hung-Yi Hsu, Chih-Ping Chung, and Han-Hwa Hu. Vertebral artery hypoplasia is associated with a decrease in net vertebral flow volume. *Ultrasound in medicine & biology*, 36(1):38–43, 2010.
- [83] Marina Piccinelli, Susanna Bacigaluppi, Edoardo Boccardi, Bogdan Ene-Iordache, Andrea Remuzzi, Alessandro Veneziani, and Luca Antiga. Geometry of the internal carotid artery and recurrent patterns in location, orientation, and rupture status of lateral aneurysms: an image-based computational study. *Neurosurgery*, 68(5):1270–1285, 2011.
- [84] Shanggang Zhou and Xiaotong Shen. Spatially adaptive regression splines and accurate knot selection schemes. *Journal of the American Statistical Association*, 96(453):247–259, 2001.
- [85] Laura M Sangalli, Piercesare Secchi, Simone Vantini, and Alessandro Veneziani. A case study in exploratory functional data analysis: geometrical features of the internal carotid artery. *Journal of the American Statistical Association*, 104(485):37–48, 2009.

BIBLIOGRAPHY

- [86] Laura M Sangalli, Piercesare Secchi, Simone Vantini, and Alessandro Veneziani. Efficient estimation of three-dimensional curves and their derivatives by free-knot regression splines, applied to the analysis of inner carotid artery centrelines. *Journal of the Royal Statistical Society: Series C (Applied Statistics)*, 58(3):285–306, 2009.
- [87] Carl De Boor, Carl De Boor, Etats-Unis Mathématicien, Carl De Boor, and Carl De Boor. *A practical guide to splines*, volume 27. springer-verlag New York, 1978.
- [88] Charles M Stein. Estimation of the mean of a multivariate normal distribution. *The annals of Statistics*, pages 1135–1151, 1981.
- [89] Carl De Boor. *Spline toolbox for use with MATLAB: user's guide, version 3*. MathWorks, 2005.
- [90] Giuseppe Mancina, Robert Fagard, Krzysztof Narkiewicz, Josep Redon, Alberto Zanchetti, Michael Böhm, Thierry Christiaens, Renata Cifkova, Guy De Backer, Anna Dominiczak, et al. 2013 esh/esc guidelines for the management of arterial hypertension: the task force for the management of arterial hypertension of the european society of hypertension (esh) and of the european society of cardiology (esc). *Blood pressure*, 22(4):193–278, 2013.
- [91] Yongyue Zhang, Michael Brady, and Stephen Smith. Segmentation of brain mr images through a hidden markov random field model and the expectation-maximization algorithm. *IEEE transactions on medical imaging*, 20(1):45–57, 2001.
- [92] Luca Antiga and David A Steinman. Robust and objective decomposition and mapping of bifurcating vessels. *IEEE transactions on medical imaging*, 23(6):704–713, 2004.

- [93] Marina Piccinelli, Alessandro Veneziani, David A Steinman, Andrea Remuzzi, and Luca Antiga. A framework for geometric analysis of vascular structures: application to cerebral aneurysms. *IEEE transactions on medical imaging*, 28(8):1141–1155, 2009.
- [94] Matthew Ethan MacDonald and Richard Frayne. Phase contrast mr imaging measurements of blood flow in healthy human cerebral vessel segments. *Physiological measurement*, 36(7):1517, 2015.
- [95] Kolja M Thierfelder, Alena B Baumann, Wieland H Sommer, Marco Armbruster, Christian Opherk, Hendrik Janssen, Maximilian F Reiser, Andreas Straube, and Louisa von Baumgarten. Vertebral artery hypoplasia: frequency and effect on cerebellar blood flow characteristics. *Stroke*, 45(5):1363–1368, 2014.
- [96] Aristeidis H Katsanos, Maria Kosmidou, Athanassios P Kyritsis, and Sotirios Giannopoulos. Is vertebral artery hypoplasia a predisposing factor for posterior circulation cerebral ischemic events? a comprehensive review. *European neurology*, 70(1-2):78–83, 2013.
- [97] Lijun Wang, Feng Zhao, Daming Wang, Shen Hu, Jiachun Liu, Zhilun Zhou, Jun Lu, Peng Qi, and Shiyong Song. Pressure drop in tortuosity/kinking of the internal carotid artery: simulation and clinical investigation. *BioMed research international*, 2016, 2016.
- [98] Simona Sacco, Rocco Totaro, Massimo Baldassarre, and Antonio Carolei. Morphological variations of the internal carotid artery: prevalence, characteristics and association with cerebrovascular disease. *International Journal of Angiology*, 16(02):59–59, 2007.

BIBLIOGRAPHY

- [99] HFG Martins, A Mayer, P Batista, F Soares, V Almeida, AJ Pedro, and V Oliveira. Morphological changes of the internal carotid artery: prevalence and characteristics. a clinical and ultrasonographic study in a series of 19 804 patients over 25 years old. *European journal of neurology*, 25(1):171–177, 2018.
- [100] P Pancera, M Ribul, S Marchi De, E Arosio, and A Lechi. Prevalence of morphological alterations in cervical vessels: a colour duplex ultrasonographic study in a series of 3300 subjects. *International angiology: a journal of the International Union of Angiology*, 17(1):22–27, 1998.
- [101] Thomas C Hinton, Zoe H Adams, Richard P Baker, Katrina A Hope, Julian FR Paton, Emma C Hart, and Angus K Nightingale. Investigation and treatment of high blood pressure in young people: Too much medicine or appropriate risk reduction? *Hypertension*, 75(1):16–22, 2020.
- [102] Alexey V Kamenskiy, Iraklis I Pipinos, Jeffrey S Carson, Jason N MacTaggart, and B Timothy Baxter. Age and disease-related geometric and structural remodeling of the carotid artery. *Journal of vascular surgery*, 62(6):1521–1528, 2015.
- [103] Adam Harvey, Augusto C Montezano, and Rhian M Touyz. Vascular biology of ageing - implications in hypertension. *Journal of molecular and cellular cardiology*, 83:112–121, 2015.
- [104] Ernesto L Schiffrin. Effects of antihypertensive drugs on vascular remodeling: do they predict outcome in response to antihypertensive therapy? *Current opinion in nephrology and hypertension*, 10(5):617–624, 2001.
- [105] Nasrul Hadi Johari, Mohamad Hamady, and Xiao Yun Xu. A computational study of the effect of stent design on local hemodynamic factors at the carotid artery bifurcation. *Artery Research*, 2020.

- [106] Milliam L Kataoka, Mary G Hochman, Edward K Rodriguez, Pei-Jan Paul Lin, Shigeto Kubo, and Vassilios D Raptopoulos. A review of factors that affect artifact from metallic hardware on multi-row detector computed tomography. *Current problems in diagnostic radiology*, 39(4):125–136, 2010.
- [107] Monika Colombo, Marco Bologna, Marc Garbey, Scott Berceli, Yong He, Josè Felix Rodriguez Matas, Francesco Migliavacca, and Claudio Chiastra. Computing patient-specific hemodynamics in stented femoral artery models obtained from computed tomography using a validated 3d reconstruction method. *Medical Engineering & Physics*, 75:23–35, 2020.
- [108] Stefano Morlacchi, Claudio Chiastra, Dario Gastaldi, Giancarlo Pennati, Gabriele Dubini, and Francesco Migliavacca. Sequential structural and fluid dynamic numerical simulations of a stented bifurcated coronary artery. *Journal of biomechanical engineering*, 133(12), 2011.
- [109] Ferdinando Auricchio, Michele Conti, Matthieu De Beule, Gianluca De Santis, and Benedict Verheghe. Carotid artery stenting simulation: from patient-specific images to finite element analysis. *Medical engineering & physics*, 33(3):281–289, 2011.
- [110] Juan R Cebal and R Lohner. Efficient simulation of blood flow past complex endovascular devices using an adaptive embedding technique. *IEEE transactions on medical imaging*, 24(4):468–476, 2005.
- [111] Boyce E Griffith. Immersed boundary model of aortic heart valve dynamics with physiological driving and loading conditions. *International Journal for Numerical Methods in Biomedical Engineering*, 28(3):317–345, 2012.

BIBLIOGRAPHY

- [112] Inc Ansys. *ANSYS CFX-Solver Modelling Guide*. Southpointe, 275 Technology Drive, Canonsburg, PA 15317, 14.0 edition, 11 2011.
- [113] Will J Schroeder, Bill Lorensen, and Ken Martin. *The visualization toolkit: an object-oriented approach to 3D graphics*. Kitware, 2004.
- [114] Christophe Geuzaine and Jean-François Remacle. Gmsh: A 3-d finite element mesh generator with built-in pre-and post-processing facilities. *International journal for numerical methods in engineering*, 79(11):1309–1331, 2009.
- [115] James Ahrens, Berk Geveci, and Charles Law. Paraview: An end-user tool for large data visualization. *The visualization handbook*, 717, 2005.
- [116] Utkarsh Ayachit. *The paraview guide: a parallel visualization application*. Kitware, Inc., 2015.
- [117] Joachim Schöberl. Netgen an advancing front 2d/3d-mesh generator based on abstract rules. *Computing and visualization in science*, 1(1):41–52, 1997.
- [118] Hang Si and A TetGen. A quality tetrahedral mesh generator and three-dimensional delaunay triangulator. *Weierstrass Institute for Applied Analysis and Stochastic, Berlin, Germany*, 81, 2006.
- [119] Volodymyr Dyedov, Daniel R Einstein, Xiangmin Jiao, Andrew P Kuprat, James P Carson, and Facundo Del Pin. Variational generation of prismatic boundary-layer meshes for biomedical computing. *International journal for numerical methods in engineering*, 79(8):907–945, 2009.

- [120] Gianluca De Santis, Peter Mortier, Matthieu De Beule, Patrick Segers, Pascal Verdonck, and Benedict Verheghe. Patient-specific computational fluid dynamics: structured mesh generation from coronary angiography. *Medical & biological engineering & computing*, 48(4):371–380, 2010.
- [121] Ian Marshall, Panorea Papathanasopoulou, and Karolina Wartolowska. Carotid flow rates and flow division at the bifurcation in healthy volunteers. *Physiological measurement*, 25(3):691, 2004.
- [122] Yuanyuan Dai, Peng Lv, Ashkan Javadzadegan, Xiao Tang, Yi Qian, and Jiang Lin. Hemodynamic analysis of carotid artery after endarterectomy: a preliminary and quantitative imaging study based on computational fluid dynamics and magnetic resonance angiography. *Quantitative imaging in medicine and surgery*, 8(4):399, 2018.
- [123] SA Urquiza, PJ Blanco, MJ Vénere, and RA Feijóo. Multidimensional modelling for the carotid artery blood flow. *Computer Methods in Applied Mechanics and Engineering*, 195(33-36):4002–4017, 2006.
- [124] Juan R Cebal, Peter J Yim, Rainald Löhner, Orlando Soto, and Peter L Choyke. Blood flow modeling in carotid arteries with computational fluid dynamics and mr imaging. *Academic radiology*, 9(11):1286–1299, 2002.
- [125] Sang Hyuk Lee, Seongwon Kang, Nahmkeon Hur, and Seul-Ki Jeong. A fluid-structure interaction analysis on hemodynamics in carotid artery based on patient-specific clinical data. *Journal of mechanical science and technology*, 26(12):3821–3831, 2012.
- [126] Zhongjie Wang, Nigel B Wood, and Xiao Yun Xu. A viscoelastic fluid–structure interaction model for carotid arteries under pulsatile flow. *International journal for numerical methods in biomedical engineering*, 31(5):e02709, 2015.

BIBLIOGRAPHY

- [127] Richard Courant, Kurt Friedrichs, and Hans Lewy. On the partial difference equations of mathematical physics. *IBM journal of Research and Development*, 11(2):215–234, 1967.
- [128] David A Steinman. *Assumptions in modelling of large artery hemodynamics*, pages 1–18. Springer, 2012.
- [129] Christian Poelma, Paul N Watton, and Yiannis Ventikos. Transitional flow in aneurysms and the computation of haemodynamic parameters. *Journal of The Royal Society Interface*, 12(105):20141394, 2015.
- [130] Paul A Yushkevich, Joseph Piven, Heather Cody Hazlett, Rachel Gimpel Smith, Sean Ho, James C Gee, and Guido Gerig. User-guided 3d active contour segmentation of anatomical structures: significantly improved efficiency and reliability. *Neuroimage*, 31(3):1116–1128, 2006.
- [131] Yukinao Kambayashi, Hiroyuki Takao, Kouichi Shinohara, Takashi Suzuki, Sho Takayama, Soichiro Fujimura, Shunsuke Masuda, Mituyoshi Watanabe, Tomoaki Suzuki, Chihebeddine Dahmani, et al. Computational fluid dynamics analysis of tandem carotid artery stenoses: Investigation of neurological complications after carotid artery stenting. *Technology and Health Care*, 24(5):673–679, 2016.
- [132] Jingliang Dong, Kiao Inthavong, and Jiyuan Tu. Image-based computational hemodynamics evaluation of atherosclerotic carotid bifurcation models. *Computers in Biology and Medicine*, 43(10):1353–1362, 2013.
- [133] D Liesch, A Balasso, C Zimmer, H Berger, R Burkhart, and H-H Eckstein. Diagnostic and therapeutic treatments of plaques in the carotid bifurcation - studies in models with stent and filters. *Journal of Mechanics in Medicine and Biology*, 14(03):1450030, 2014.

- [134] Boyce E Griffith and Neelesh A Patankar. Immersed methods for fluid–structure interaction. *Annual Review of Fluid Mechanics*, 52:421–448, 2020.
- [135] F Auricchio, M Conti, M Ferraro, and A Reali. Evaluation of carotid stent scaffolding through patient-specific finite element analysis. *International journal for numerical methods in biomedical engineering*, 28(10):1043–1055, 2012.
- [136] Michele Conti, Denis Van Loo, Ferdinando Auricchio, Matthieu De Beule, Gianluca De Santis, Benedict Verhegghe, Stefano Pirrelli, and Attilio Odero. Impact of carotid stent cell design on vessel scaffolding: a case study comparing experimental investigation and numerical simulations. *Journal of Endovascular Therapy*, 18(3):397–406, 2011.
- [137] Ian Marshall, Shunzhi Zhao, Panorea Papathanasopoulou, Peter Hoskins, and X Yun Xu. Mri and cfd studies of pulsatile flow in healthy and stenosed carotid bifurcation models. *Journal of biomechanics*, 37(5):679–687, 2004.

Acknowledgements

This dissertation was written from 2017 to 2021 during my time spent as PhD student at the Department of Civil Engineering and Architecture (DICAr) at the University of Pavia, Italy. First of all, I would like to thank sincerely Prof. Michele Conti. I really think I have been lucky to have him as my doctoral supervisor: during these years, he has been able to leave me enough space to explore my personal research ideas, but at the same time he was always ready to help me when I needed it. I would also like to thank sincerely Prof. Ferdinando Auricchio, for giving me the opportunity to work in his research group and for his valuable guidance. During the course of my research project, I spent four months at the Bristol Heart Institute in the United Kingdom. I want to thank Dr. Giovanni Biglino, Dr. Chiara Bucciarelli-Ducci and Dr. Silvia Schievano for their kind hospitality and the good cooperation that we continued also afterwards. A special gratitude goes also to my friends and colleagues: Alfredo, Karim, Lorenzo and Mauro. Thank you for your support, advices, lunches, dinners and laughs. You were able to cheer me up even in the foggiest days. Finally, I have to thank the people that belongs to my heart. My family, far away from here, but always in my thoughts. And Lorena, my soulmate, my angel. Thank you for your unconditional support: I wouldn't be writing this thesis without you.